Microstructural Engineering for Ultra High Strength Steel Wire

Daniel Jensen

Department of Materials Science and Engineering

A thesis submitted to The University of Sheffield for the degree

of Doctor of Engineering in the Faculty of Science and Engineering.

September 2023

Acknowledgements

I firstly want to thank my academic supervisor, Professor W. Mark Rainforth, for his invaluable support and advice throughout the EngD project at the University of Sheffield. Completing this work through a global pandemic and other setbacks would not have been possible without him.

Additionally, I would like to thank Engineering and Physical Sciences Research Council (ESRPC) and the Henry Royce Institute for Advanced Materials for their financial support with the project.

I would like to also thank British Steel and their research and development team based at the Advanced Manufacturing Research Centre (AMRC) near Rotherham. More specifically, I would like to thank my industrial supervisor, Shaun Hobson and his colleague, Sally Parker, for providing steel material, wire drawing facilities, contribution to technical work and their vast knowledge on steel metallurgy, the rod and wire industry and processing routes. I would also like to thank Shaun personally for his kind words and promise to support the project, even with the project potentially being dropped by British Steel due to financial issues.

I would like to thank the technical staff here within the University of Sheffield who have helped throughout the project. I am forever grateful for D. Haylock for his help with the Thermomechanical Compression Machine (TMC), humour and his kindness to always make time for my long isothermal holding heat treatments.

Additionally, John Nutter provided a lot of advice, friendship, and help, and being able to electropolish and obtain decent TEM images would have been a lot more difficult without him.

Finally, I would like to thank my friends, family and my wife, Sophie. Their constant encouragement and support have helped me through this project, and I am eternally grateful for them.

Abstract

The potential cost savings in weight result in an ever-growing demand for higher strength steel rod and wire. Steel rod and wire is utilised in a multitude of applications such as springs, tyre cords, suspension bridge cables and mooring ropes. Whilst high carbon pearlitic microstructures currently dominate the wire and rod market, research in the industry has shown there are only marginal gains to be made in tensile strength for this microstructure. Therefore, alternative steel microstructures are being investigated for potentially larger gains in mechanical properties. This research investigated the development of alternative steel rod microstructures for high strength steel rod/wire applications and compared them to the current leading high strength pearlitic grades available. The two main alternative steel microstructure that were investigated are quench and partitioned (Q&P) steels and carbide free bainitic steels.

British Steel have performed past work on these microstructures and found that the retained austenite in the microstructure is a key issue towards drawing the steel rods down to wire. The retained austenite transforms into fresh untempered martensite under deformation, a process known as the TRIP effect (transformation-induced-plasticity). Therefore, a key objective for the work is to stabilise the retained austenite found in both alternative microstructures as much as possible.

For the Q&P steels, steel rods provided by British Steel from previous research were heat treated using molten salt baths and investigated using optical and scanning electron microscopy (SEM). However, the lower temperature quench to a higher isothermal holding temperature proved difficult to facilitate, and so the project scope was narrowed to focus on carbide free bainites.

The alloys used to investigate the carbide free bainites were designed and cast using a vacuum induction melting furnace. The cast ingots were then machined and rolled to refine the

microstructures. The axisymmetric samples were then machined from the rolled steel and were isothermally heat treated to produce bainitic microstructures. The effect of a second isothermal holding step was also investigated, to further transform the retained austenite in the bainite microstructures.

This research produced carbide free bainite microstructures, with carbides not being present in either the EBSD maps or the TEM/STEM images taken. It was found that the second isothermal holding step was beneficial in reducing the final fraction of retained austenite in the microstructures. This could be useful in future carbide free bainitic investigations to improve the mechanical properties of the steels, by achieving higher volume fractions of nanostructured bainite. The alloy composition with the lower martensitic start temperatures, M_s, was found to have lower amount of retained austenite and the morphology of the retained austenite was more thin film like. This morphology is more stable than more blocky/polygonal retained austenite, and therefore can avoid the formation of untempered martensite through the TRIP effect, increasing the ductility and drawability of the steel. The work performed highlights the importance of the morphology of the retained austenite in carbide free bainites and presents a possible processing route for further development on the microstructure.

Contents

Nomenclature

α - Ferrite

γ - Austenite

ε - Engineering strain

σ - Engineering stress

b - Breadth

B_f - Bainite finish temperature

B_s - Bainite start temperature

h - Height

ΔG - Gibbs free energy

L - Length

M_f - Martensite finish temperature

M_s - Martensite start temperature

PT - Partitioning Temperature

QT - Quenching Temperature

T - Temperature

t - time

T_0 - Temperature at which α and γ have the same free energy

vol.% - Volume percentage

w - Width

wt.% - Weight percentage

1.0 Introduction

High strength steel wire can reach tensile strengths of up to 7 GPa and is utilised in a variety of applications, such as for suspension bridge cables, springs, tyre cord and mooring cables. The steel product's enhanced strength is attributed to the microstructure that is produced upon cold drawing the wire. This mechanical process dramatically increases the dislocation density and reduces the interlamellar spacing between the ferrite and cementite layers in the pearlite, resulting in a fine microstructure that provides good tensile strength and ductility.

The market is currently dominated by hypereutectoid pearlitic grades, ranging from 0.8 to 1.0 wt.% carbon. However, there is a need for higher strength-to-weight ratios to achieve both weight savings and yield cost efficiencies in fuel economy. Many at British Steel believe that the hypereutectoid pearlitic grade wires are approaching a tensile limit. High levels of cold drawing can result in a phenomenon known as cementite dissolution, where the cementite lamellae are lost by carbon diffusing into the ferrite lamellae. This results in large decreases in ductility in the product, limiting further improvements in the strength of the wire. In addition, the formation of proeutectoid cementite and its detrimental effect on cold drawing limits the carbon content to around 1.05 wt.%. Therefore, alternative microstructures are being investigated as many in the industry believe there are larger strength-to-weight ratios to be gained rather than focusing on high carbon pearlitic structures.

The hot rolled rod needs to exhibit a high tensile strength and high ductility. Additionally, a high work hardening rate is required during wire drawing, with 500 MPa per unit strain being the typically highest rate obtainable. Following wire drawing, the wire should still exhibit good ductility, usually measured through tensile, bend and torsion testing. This is where the severe challenge lies; producing a material that exhibits high work hardening rate, but which still exhibits adequate ductility after wire drawing.

Numerous strategies have been developed to produce high strength steels. These steels have been developed for a wide range of products, most commonly sheet. However, there has been little development of high strength wire. Of the high strength steel processing strategies, the following could potentially be used for wire (with due attention paid to whether they would likely be considered commercially):

- Low and high carbon bainitic steels
- Carbide free bainites or "Super bainites"
- Dual phase steels:
    - Ferrite / martensite
    - Martensite / bainite
    - Quench & partitioned austenite / martensite
- Amorphous/nanocrystalline steels

None of the microstructures listed above were developed for subsequent high strain wire drawing (true strains of up to 5). There is therefore a clear research question:

"Can an alternative to pearlite rod be developed that can be drawn to high strain and retain adequate ductility?"

British Steel has undertaken preliminary studies into this research by looking at rod processed to the various microstructures listed above. This has shown potential for a wide range of microstructures but has not developed mechanistic understanding that could lead the way towards a new commercial wire product.

Initially, this EngD project was focussed on studying quenched and partitioned (Q&P) steels, which have microstructures consisting of tempered martensite and retained austenite. However, the availability and control of external molten salt bath facilities saw the project scope change. The project then focussed on investigating carbide-free bainite, as the quench rate requirements are not as limiting and lower carbide-free bainitic wire has been shown to have promising mechanical results as an alternative to pearlite.

1.1 Aims and Objectives

Whilst lower bainite provides higher work hardening rates in drawn steel wire than a conventional pearlitic microstructure, there are two main drawbacks with this alternative. One is that retained austenite in the steel undergoes a transformation induced plasticity (TRIP) reaction whereby the retained austenite is transformed into martensite. This dramatically decreases the ductility and drawability of the wire, causing brittle failures. In addition, the untempered martensite formed by the TRIP reaction results in inferior torsional ductility in wire, when compared to pearlitic grades. The other issue is the relatively long transformation times to produce nano-bainite with little to no carbide precipitation. These transformation times can be more than two days. Therefore, the overall aim of the work is to investigate alternative microstructures for cold drawn steel wire. The two main objectives for the work are as follows:

- To investigate the stability of retained austenite under deformation/wire drawing.
- To create a fully nanostructured bainitic microstructure containing minimal retained austenite, preferably with a needle-like morphology

1.2 Structure of the Thesis

The thesis consists of the following chapters, Literature Review; Experimental Methods; Q&P Work; Carbide Free Bainite Work 1; Carbide Free Bainite Work 2; Conclusions; and Future Work.

The literature review analyses previous research on steel wire and the alternative microstructures. The following research is discussed, an introduction to steel rod and wire; cold wire drawing; bainite; and quench and partitioned steels. The analysis of this research helps to identify the suitability of the alternative microstructures for cold drawn steel wire.

The experimental methods chapter introduces the experimental techniques that were utilised in this study. Additionally, the chapter provides an overview of how the steel ingots were produced and processed to becoming axisymmetric samples.

The Chapter: Q&P Work, discusses the work done to investigate quench and partitioned (Q&P) steels as an alternative microstructure for cold drawn steel wire and rod, as was one of the aims of the study.

Carbide Free Bainite Work 1 covers the initial work performed on producing and investigating a carbide free bainitic steel alloy. This chapter focuses on the objective to create a fully nanostructured bainitic microstructure containing minimal retained austenite.

Carbide Free Bainite Work 2 is the supporting chapter on the investigation of carbide free bainitic microstructures. The chapter investigates whether altering the chemical composition of the steel alloy, or by utilising a second isothermal holding treatment, stabilises the retained austenite under deformation.

The Conclusions chapter provides a comprehensive summary of the key findings and main implications of this work.

Finally, Future Work highlights what parts of the study could be investigated further if the work was to be continued for future research.

2.0 Literature Review

This Chapter begins by providing an introduction into the steel wire and rod, highlighting some of the key issues faced in the industry. After which, the two alternative steel microstructures are discussed for the remainder of the section.

2.1 An Introduction to Steel Rod and Wire

Pearlitic steel rod is a highly versatile material, that can create a wide range of products due to the material's high formability. Pearlite is a microstructure made up of alternating parallel lamellae of cementite (Fe_3C) and ferrite (α-Fe), formed through a eutectoid transformation from austenite (γ). Focussing on just one of the many rod products available, drawn steel wire alone is utilised in mooring cables for deep sea applications, tyre cord to reinforce rubber tyres and in suspension bridge cables. These applications take advantage of the high strength that drawn pearlitic steels can achieve, with strengths up to 5-6 GPa being reached [1].

2.1.1 Production of Steel Rod

At the rod mill in British Steel's site in Scunthorpe, production begins with large 4 tonne steel blocks known as blooms. The steel was produced on site using the blast oxygen steelmaking (BOS) process, before being cast into blooms with dimensions of 283 mm by 230 mm. The blooms undergo up to 32 rolling passes, in order to achieve the desired rod diameter. After which the rod is water cooled, before passing through the lay head which has a geometry that causes the rod to coil. The coiled rod is then cooled on a Stelmor cooling conveyor, where fans provide controlled air cooling. Finally, the cooled coils are placed into coil reform tubs at the end of the conveyor for further inspection, trimming and sampling. An alternative option for cooling of the wire rod is to utilise lead patenting. This is a process that further enhances the pearlitic microstructure, whereby the steel, after receiving an austenisation treatment at 900-950°C, is quenched into a bath of molten lead.

2.2 Cold Wire Drawing

Wire drawing is an excellent way to increase the strength of a product through the work hardening achieved by the deformation. The process reduces the cross-section area of the rod/wire by pulling the product through a series of drawing dies with decreasing diameter dimensions. It is usually performed at room temperature, although the deformation introduced generates a large amount of heat and so commercial drawing normally incorporate some form of wire cooling. For fine wire sizes an intermediate lead patenting treatment may also be utilised to restore some ductility to the wire.

It is vital that the tensile strength used for drawing is not larger than the ultimate tensile strength of the rod/wire, as this would cause necking or a potential break. Thus the reduction of area per drawing pass is usually limited to around 35% or less [2]. To achieve larger reductions, the process is often repeated using multiple dies with decreasing diameters until a final desired wire diameter for the product is reached.

2.2.1 Wire Drawing Strengthening Mechanisms

Embury et al. [3] and Langford [4] were some of the first to report findings on the deformation of pearlitic wires and the related strengthening mechanisms. Both authors related the strength to the sub structure of cementite lamellae that formed after drawing, noting that the interlamellar spacing was typically less than the thickness of the prior cementite plates. Using transmission electron microscopy (TEM), it was shown that the mean barrier spacing (i.e. the interlamellar spacing) decreased proportionally with a reduction in area during wire drawing. This knowledge was utilised to create a modified Hall-Petch equation, relating the flow stress and strain together:

$$\sigma = \sigma_0 + \frac{k_1}{(2\lambda_0)^{0.5}} . e^{\left(\frac{\varepsilon}{4}\right)} \tag{2.1}$$

where σ and σ_0 are the final and initial strengths respectively, k is the Hall-Petch constant, λ_0 is the original lamellar spacing and ε is the drawing strain. Though the equation helps to relate the flow stress with drawing strain, mechanical data shows that at high strains the linear relationship breaks down, as k_1 is no longer constant. Zhang et al. [1] showed this schematically in a graph of results collected from previous studies, shown in Figure 2.1. The divergence from linearity at high strains has convinced many researchers that the strengthening mechanisms for pearlitic drawn wire must be due to the combination of multiple strengthening factors [1,7–9].

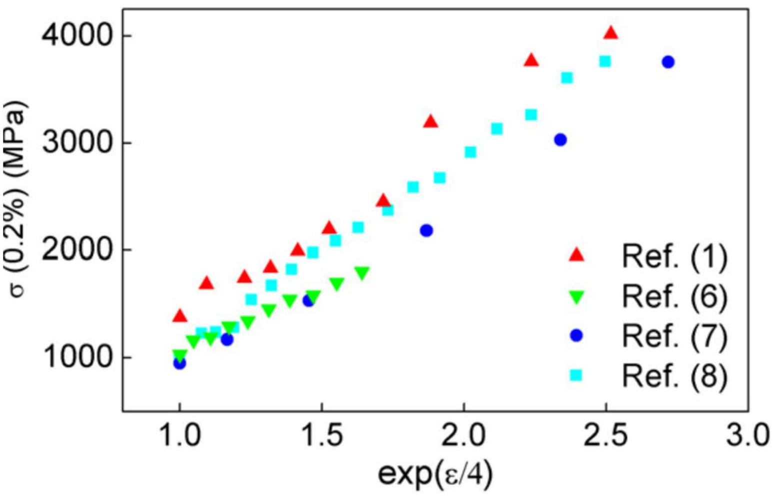

Figure 1.1: Summary of compiled mechanical data of pearlitic steel wires from multiple studies [1].

However, there is still some disagreement as to what strengthening mechanisms are involved for cold drawing pearlitic steel wire. Zhang et al. [1] theorises that there are three main strengthening mechanisms at play:

- The boundary strengthening which is in relation to the distance between the cementite lamellae and in turn the modified Hall-Petch equation
- The strain hardening strengthening which is due to the increase in the dislocation density through drawing
- The solid solution strengthening effect which is caused by cementite dissolution increasing the carbon concentration in the ferrite lamellae.

They then proposed that these mechanisms acted together in linear addition, and created the following equation to express the flow stress of the wire:

$$\sigma(\varepsilon) = \sigma_0 + \sigma(b) + \sigma(p) + \sigma(ss) \tag{2.2}$$

In the equation, $\sigma(\mathrm{b}), \sigma(\mathrm{p})$ and $\sigma(\mathrm{ss})$ are the boundary, strain hardening and solid solution strengthening respectively. The additional term σ_0 is the friction stress associated with pure ferrite. This expression however assumes that the ferrite and cementite lamellae are parallel and the wire has a fibrous structure.

As touched upon earlier, many studies noted the dominating mechanism as the boundary strengthening [1, 5, 7, 8, 10]. Typically, the Hall-Petch equation relates the strength of a material to the grain size of the material's microstructure. The size of the grains is taken as the mean free barrier path for dislocations. However as stated previously, the interlamellar spacing is typically less than the thickness of the original cementite plates. Therefore, the mean free path of dislocations is instead related to interlamellar spacing of the pearlite. Gensamer et al. [10] showed that the mean uninterrupted ferrite path is around 1.9 to 2 times the interlamellar spacing, which Zhang et al. [1] then utilised to create Equation 2.3:

$$\sigma(\varepsilon) = \sigma_0(\varepsilon) + k(\varepsilon)(2d)^{-0.5} \tag{2.3}$$

Borchers and Kircheim [5] suggest an additional strengthening mechanism occurs during plastic deformation, known as dispersion strengthening. Whilst this mechanism is typically not applied to pearlite due to the non-deformability of the cementite present, the study suggests this however changes when cementite becomes amorphous (amorphous cementite has been observed by several researchers in very heavily drawn wires) [11]. Due to the increased hardness of the amorphous cementite, it is implied that this will strengthen the surrounding soft ferrite matrix. Furthermore, the study states that additional geometrical dislocations will be formed by the plastic inhomogeneity associated with differing strain gradients in the heavily drawn pearlite. Zhou et al. [12] in agreement with these finding, state that the amorphous cementite acts as a large dislocation barrier between the ferrite lamellae. Their study also mentions that when annealed, the amorphous cementite can decompose into an ultra-fine nano-crystalline structure creating more barriers and further strengthening the wire.

The solid solution strengthening ($\sigma(ss)$) is due to the large amount of deformation during drawing causing the dissolution of cementite into the ferrite matrix, which in turn acts as additional barriers for dislocations and therefore increasing the strength of the wire. At strains less than 2.67, Zhang et al. [1] reports that this is not a major contributing strengthening mechanism. However, at strains above 3.67 the mechanism becomes significant as the ferrite is enriched with carbon, with reported estimated strengthening effects of around 400MPa. This is supported by Lamontagne et al. [13], who utilised the thermoelastic power technique (TEP) and electrical resistivity measurements to show that the amount of cementite dissolution that occurred in pearlitic wires during the drawing did not become significant until strains greater than 1.5.

The phenomenon of the dissolution of cementite in pearlitic wire during drawing was first observed using Mössbauer spectroscopy in 1972 [14]. There is an on-going debate on the dominant mechanism involved with decomposition of the cementite, resulting in three suggested theories. The first was that the carbon atoms were highly attracted to the dislocations generated through drawing. In this model, the interaction force between the dislocations and the carbon atoms is suggested to be larger than the binding energy between the iron and carbon atoms, therefore when heat is generated through drawing the carbon atoms diffuse to the dislocations [15]. The second theory relates the dissolution to the Gibbs-Thompson effect. The idea is that as the drawing continues and the cementite begins to fragment, there is an increase in the free energy of the interface between the matrix and the cementite thus increasing the local solubility of the carbon. Finally, the last hypothesized mechanism was referred to as the “carbon drag effect” in a large amount of research [1, 8, 16].

The effect is again related to the carbon atoms being attracted to dislocations. When the dislocations originally generated at the cementite-matrix interface move away from the interface, the carbon atoms are then deposited into the ferrite matrix when the dislocations annihilate, forming a supersaturated matrix in the process. There are a number of reasons why reaching a consensus on the main mechanism for the dissolution of the cementite is so difficult. One issue is that the microstructures produced during drawing are very fine and therefore it is difficult to characterise the carbon within the microstructures. Another issue is the lack of repeated ageing temperatures and drawing conditions in research, both of which heavily influenced the state of the carbon within the drawn pearlite. Finally the techniques frequently used to observe these mechanisms (atom probe tomography and transmission electron spectroscopy) focus on a very small region, resulting in a highly localised analysis [14, 16].

2.3 Bainite

Bainite is a steel microconstituent, with a microstructure consisting of ferrite plates or sheaves, cementite and retained austenite. The constituent is formed by controlled cooling from the austenite phase, with high enough rates to avoid the formation of pearlite but avoiding the formation of martensite. It can also be formed through an isothermal heat treatment, by holding at a temperature, after quenching, that is between the martensitic start temperature and the bainitic start temperature.

Davenport and Bain [16] were the first to discover the microstructure, during studies on isothermal transformations to observe phase changes as a function of time and temperature. The microstructure was named “bainite”, in honour of Edgar Collins Bain. However, the term was not originally popular, with Bain describing bainite as an "unnamed, dark etching, acicular aggregate somewhat similar to martensite" in a paper on steel nomenclature in 1936 [17]. Figure 2.2 shows a schematic TTT diagram for steel and where the bainitic region lies.

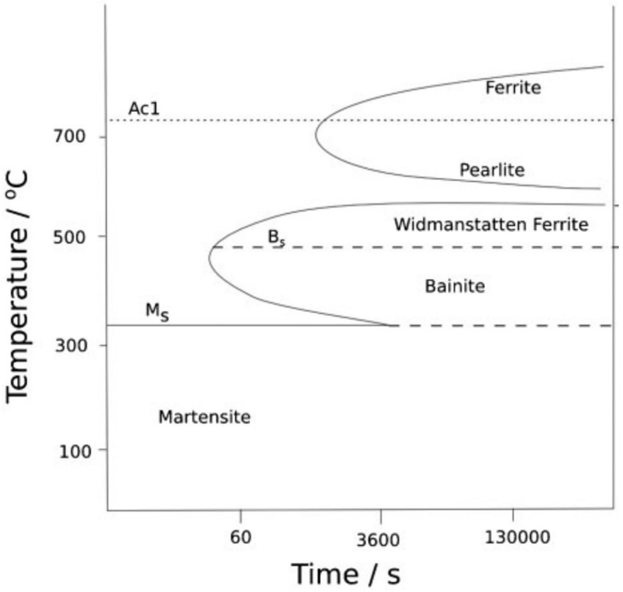

Figure 2.2: Schematic of the TTT diagram showing the bainitic region [16].

Bainite is classified by the temperature range at which the microstructure was formed, with upper bainite and lower bainite being formed at relatively high temperatures and low temperatures in the same steel respectively. The main variation between the two groups is the morphology of the subunits and carbide precipitates. Figure 2.3 helps to demonstrate the difference between the two structures schematically [18]. Upper bainite consists of ferrite lath subunits separated by coarse carbide precipitates. Lower bainite however, consists of more fine carbide precipitates within the ferrite subunits, in addition to the inter-lath carbides.

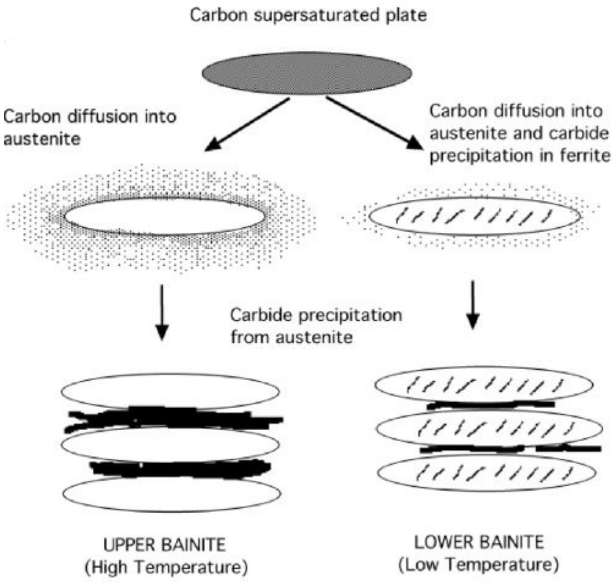

Figure 2.3: Schematic diagram showing the difference in formation and morphology of upper and lower bainite [18].

2.3.1 Incomplete Reaction Phenomenon

During the isothermal transformation of austenite to bainitic ferrite, a phenomenon is observed where the some of the austenite remains untransformed regardless of holding times. The reaction is said to be incomplete, thus the phenomenon is commonly coined the incomplete reaction phenomenon. Zener [19] described the transformation in terms of free energy, defining a temperature, T_0, where the austenite and ferrite phase of the same composition have the same free energy. Equation 2.4 was used to show the change in free energy of the system.

$$\Delta G = -\Delta G_{Fe^{x\gamma}} + C\Delta G_{C^{\gamma x}} - CT\Delta S_{C^{\gamma x}} \tag{2.4}$$

$\Delta G_{Fe}{}^{x\gamma}$ is the change in free energy of 1 mole of pure iron in the austenite phase when compared to the ferrite phase, $C\Delta G_{C}{}^{\gamma x}$ is the change in free energy of 1 mole of carbon in the ferrite phase compared to the austenite phase and $CT\Delta S_{C}{}^{\gamma x}$ is the excess of entropy of one mole of carbon when dissolved in austenite. This final term can be considered negligible if the transformation times are small enough to not consider the rate of carbon diffusion. By solving the equation for $\Delta G = 0$, it is possible to plot the carbon concentration in the austenite at the T_0 temperature. Figure 2.4 is a schematic diagram of the T_0 line on the Fe-C phase diagram, produced by Bhadeshia and Edmonds [17]. The line represents a maximum temperature for the bainitic transformation at a given carbon content, known as the bainitic start temperature, B_S.

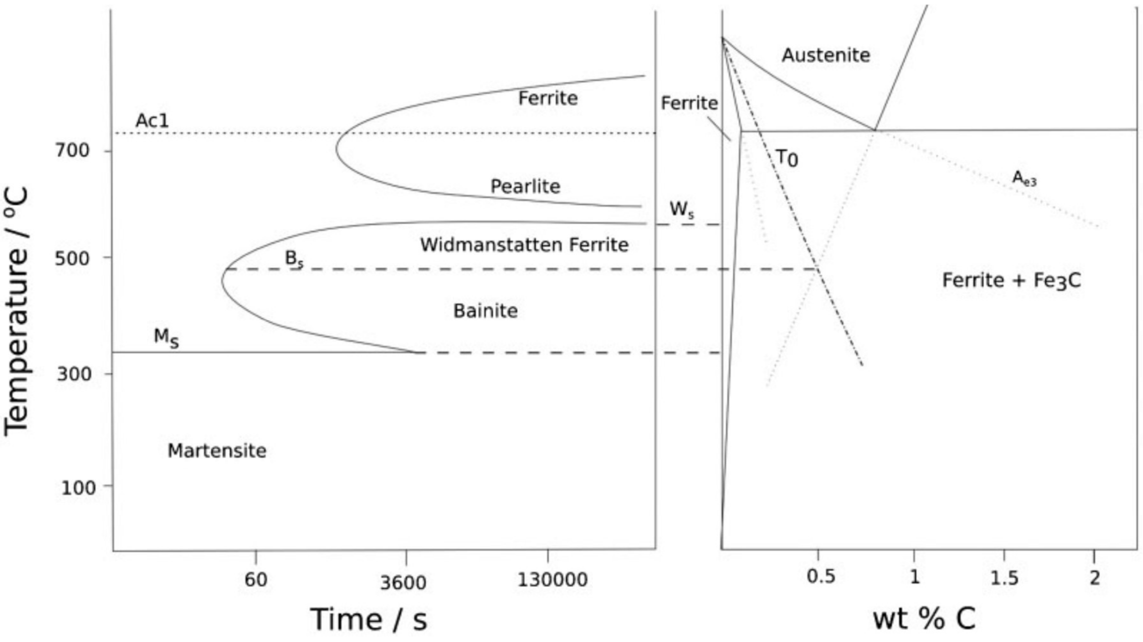

Figure 2.4: Schematic diagram of the TTT diagram for bainite and the relation to the phase diagram, showing the T_0 temperature [17].

Zener described this as a displacive transformation. The study summarised that a subunit of bainite nucleates supersaturated in carbon, which is then rejected into the surrounding austenite (when the formation of carbides is inhibited). Due to the increasing carbon content in the austenite, the driving force for the nucleation and growth of the bainitic ferrite decreases with each subsequent subunit. The T_0 lies between the extrapolated A_{e1} and the A_{e3} lines on the iron-carbon phase diagram. The free energy will then eventually reach 0 at the T_0 line, when the ferrite and austenite have equal free energy, leading to the incomplete reaction and the resulting untransformed austenite remaining. Le Houillier et al. [20] proposed a T_0' line, which accounts for the strain energy of the bainite transformation. Experimentally, the transformation reaction austenite content has been found to match well with the T'_0 line, as shown in results from Caballero and Bhadeshia [21] in Figure 2.5. However, the theory that the bainite transformation is a diffusion-less, displacive mechanism is still debated, as many researchers believe that the transformation is through a diffusive mechanism is instead.

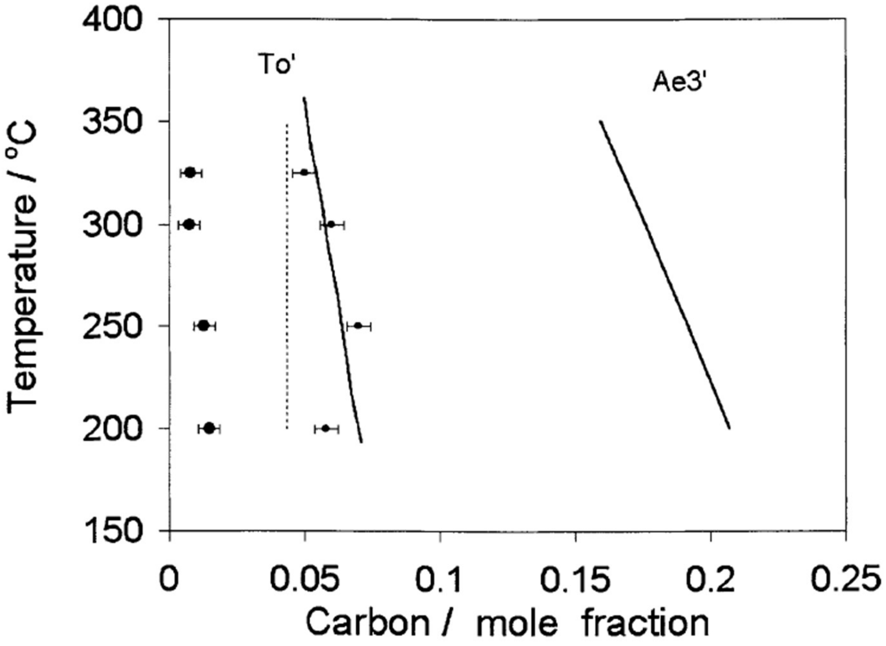

Figure 2.5: Experimental data showing the carbon mole fraction in the retained austenite matches closely with the T'_0 *line [21].*

2.3.2 The Transformation of Bainite: Displace or Diffusive

In the displacive transformation theory for bainite, the growth of sub units is halted by plastic relaxation in the surrounding austenite. The end of the sub units are then nucleation points for new sub units to form. Each sub unit is initially supersaturated with carbon upon nucleation. The carbon then partitions from the ferrite and precipitates into either the surrounding austenite, to form upper bainite, or into the subunit to form lower bainite. If carbide precipitation is inhibited, for example using a high silicon addition, the bainitic ferrite growth is halted due to the T_0' curve shown in Figure 6, and therefore the transformation is incomplete. Fielding et al. [22] summarised that the work that supports this theory to include:

- Evidence of the carbon partitioning during nucleation through synchrotron work [23]
- Plastic relaxation and surface relief results found in the surrounding austenite during growth [24], [25]
- X-ray data showing that the retained austenite content closely matches the T_o' curve [17], [21], [25]
- Atom probe and synchrotron studies showing carbon partitioning during nucleation and the supersaturation in bainitic ferrite during transformation [25], [26]

In addition, the theory helps to describe why the formation of upper bainite and lower bainite is prevented in high carbon steels and low carbon steels respectively [18]. The theory has been used to predict the TTT and CCT curves of bainitic steels with reasonable accuracy, leading to its utilisation in the design of many new bainitic alloys [27]–[30].

In the diffusive theory, bainite transformation is due to a reconstructive nucleation and growth mechanism. This results in the subunits that are not supersaturated with carbon on formation. In this model the ferrite and cementite grow cooperatively. The subunits grow preferentially in the edgewise direction, characterised by formation of ledges. Fielding et al. [22] once again summarised that the evidence for this theory:

- Similarities in bainitic microstructures and other microstructure formed by diffusive transformation [31]
- Evidence for the ledge mechanism with atomic force microscopy (AFM) measurements showing a surface relief in bainite that is characteristic of the ledge effect [32]

The diffusive theory is also beneficial in calculating the limits of both Widmanstätten and bainitic ferrite growth, using the critical carbon content of austenite.

One fundamental issue in solving which of the two theories is the most accurate, is the lack of a clear definition for bainite. The general “microstructural” definition for bainite is that bainite a non-lamellar microstructure form by eutectoid decomposition. The two phases are formed by diffusional nucleation and growth, however, the phases do not grow cooperatively. Pearlite is then the lamellar counterpart and would be the alternative microstructure formed from eutectoid decomposition [22]. The overall reaction kinetics definition describes the bainite reaction as having its own C-curve on a TTT-diagram, providing an upper limiting temperature at which no bainite can form. This is defined as the B_S (bainite-start) temperature. The amount of bainite formed in the matrix increases as the isothermal holding temperature is lowered, up to a bainitic finish temperature, B_f. The closer the transformation temperature is to the B_s temperature, the more incomplete the bainite reaction is. The surface relief definition states that bainite is plate shaped product that forms by shear.

The microstructural and surface relief definitions contrast the most, as the microstructural definition requires the precipitation of a second phase as opposed to the surface relief definition. The two definitions also state the mechanism for the transformation of bainite within them, therefore the definitions are exclusionary to each other. Fielding [22] states that this only adds to the confusion of the problem and that until a fundamental definition can be agreed, it is unlikely that a fundamental mechanism for the bainitic transformation can be concluded.

2.3.3 Carbide-free bainite

Typically, bainitic microstructures are limited in commercial applications by the coarse carbides that develop during the long isothermal heat treatments required for transformation. However, Bhadeshia and Edmonds [33], [34] found that an addition of <2 wt.% Si suppresses the formation of these carbides and in turn expands the industrial applicability of the microstructure. The development of carbide-free bainites then led to the development of nanostructured bainites; microstructures consisting of a mixture of platelets of bainitic ferrite (20-40 nm in thickness) and carbon-enriched retained austenite [21]. This unique microstructure is produced by transforming to bainite at low isothermal holding temperatures, with the martensitic start (M_s) temperature as low as 125 °C being utilised [35]. This allows for the production of nanostructured steel on a large scale, which was previously not achievable through severe deformation methods [36]. Nanostructured bainitic steels have also reached strength/toughness combinations of around 2.2 GPa/30 MPa$^{1/2}$, some of the highest values ever reached by bainitic steels [37]. Due to the incomplete reaction phenomenon, it is not possible to transform all the austenite phase into bainitic ferrite. For carbide-free nanostructured bainite, carbon partitions from the bainitic ferrite into the surrounding austenite during the isothermal holding heat treatments, stabilising it to exist at room temperature by reducing the M_S well below room temperature.

When mechanically deformed, the retained austenite undergoes a transformation into martensite, which is known a transformation induced plasticity (TRIP) effect. TRIP steels are designed to take the full benefit of this effect, as the high work hardening causes results in a moderate gain in both ultimate tensile strength and uniform elongation [37], [38]. There are two main factors that are increasing the work hardening in TRIP steels: the volume and shape changes associated with the TRIP effect and the composite microstructure present. The difference in the mechanical properties of the phases results in stress and strain partitioning during deformation as a result of the formation of the hard martensite during loading. The ongoing transformation to martensitic during deformation achieves the best strength to ductility ratios. Figure 2.6 shows the stress-strain curve and the change in austenite volume fraction during the deformation of three TRIP steels [38]. Whilst bainitic steels are also composite in nature, the relatively soft retained austenite is set in a matrix of hard bainitic ferrite and therefore shows a much more different behaviour.

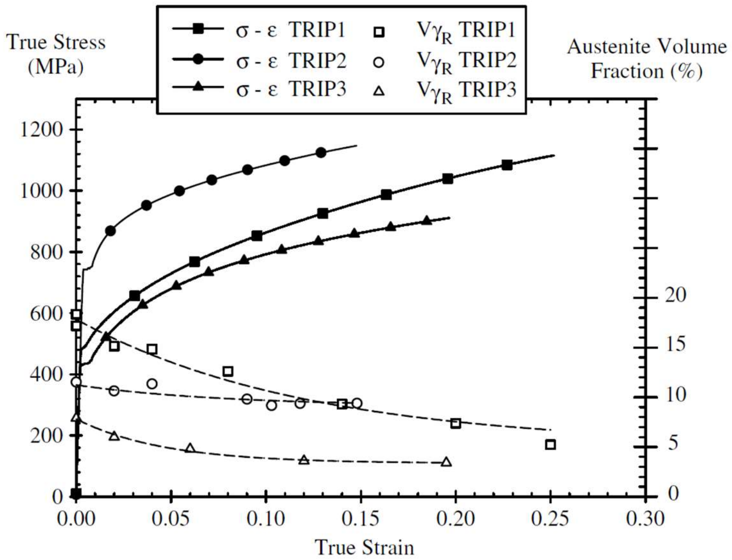

Figure 2.6: Three TRIP steel stress-strain curves and the evolution of the austenite volume fraction during deformation [38].

Work hardening can be taken as a ratio of the ultimate tensile strength and the yield strength of a material. Typically, with TRIP steels, a lower yield strength increases the amount of uniform elongation during deformation before reaching the ultimate tensile strength, due to the work hardening brought on by the TRIP effect. This can be observed in the stress-strain curves of the TRIP steels displayed in Figure 2.6. In comparison, nanostructured bainites do not show this same relationship, as shown in Figure 2.7 (a). The results for Figure 2.7 were taken from Sourmail et al. [39] and adapted by Morales-Rivas et al. [37]. into Figure 2.7 (a), (b) and (c). Furthermore, neither the yield strength or the ultimate tensile strength seems to correlate with the elongation of the nanostructured bainite, as shown in Figure 2.7 (b) and (c).

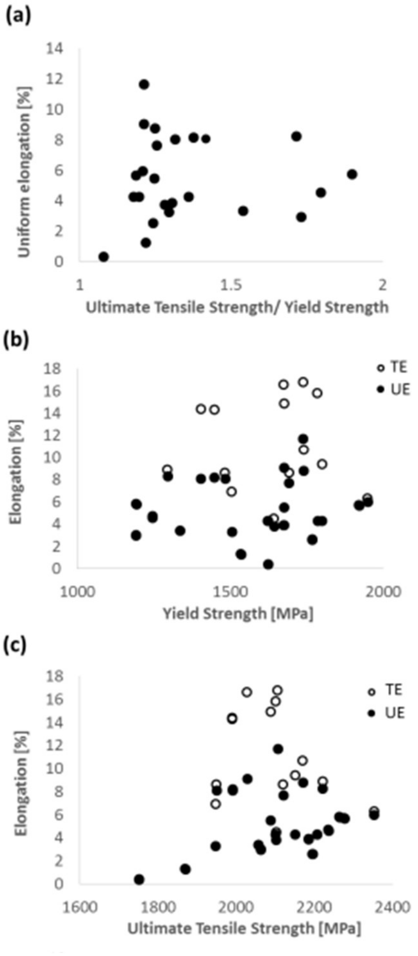

Figure 2.7: Strength vs elongation parameters from different nanostructured bainites [37].

(a) Uniform elongation versus the ratio between the UTS/yield strength.

(b) Elongation vs yield strength (both total and uniform elongation).

(c) Elongation vs UTS (both total and uniform elongation).

The retained austenite morphology in the bainitic microstructures can be categorised in to two different morphologies: thin-films or coarser more polygonal blocks (often referred to as blocky retained austenite). Figure 2.8 shows these two different phase morphologies in two micrographs [33]. In nanostructured bainite, blocky polygonal regions of retained austenite are not desirable. This morphology is not as stable as thin film of retained austenite, that form between the subunits of bainitic ferrite, and therefore the blocky retained austenite is more likely to undergo the TRIP effect into fresh untempered martensite. The formation of this hard phase dramatically reduces the ductility of the bainite. The retained austenite can also transform to martensite during cooling to room temperature if insufficient carbon has partitioned into the austenite. Thin-film retained austenite can contain higher carbon contents due to greater partitioning and the smaller distances covered. Therefore, to improve the mechanical properties of the nanostructured bainite, it is preferential to decrease the volume fraction of blocky morphology retained austenite and increase the volume fraction of the much more stable thin film morphology.

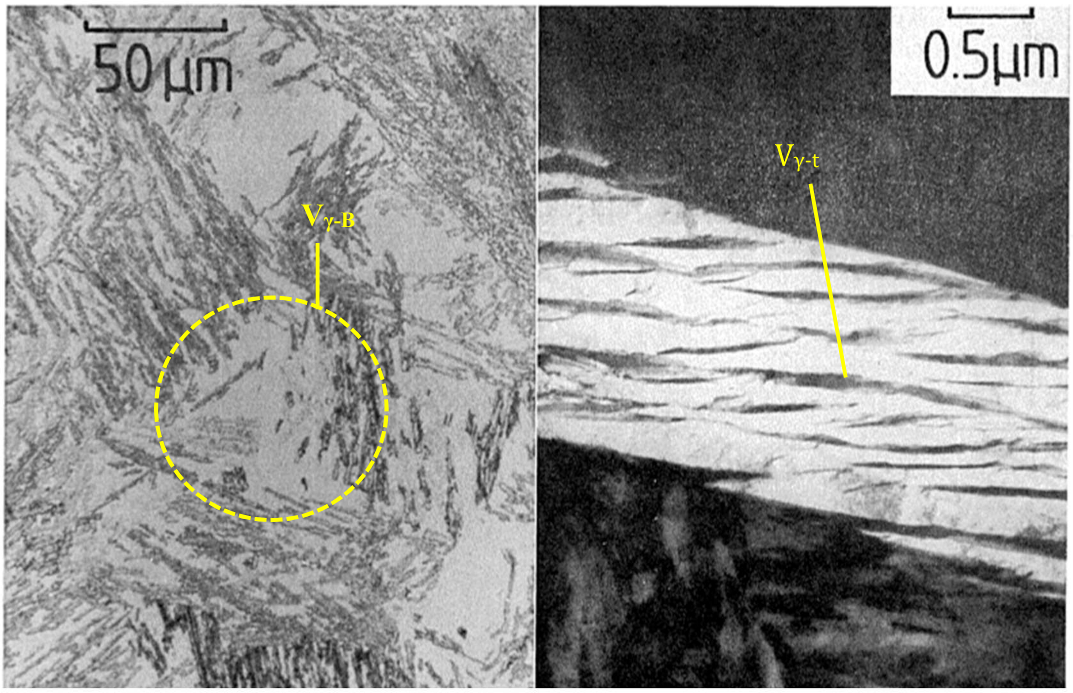

Figure 2.8: left image (a) shows blocky austenite in an optical micrograph while (b) is an electron micrograph showing retained austenite separating the bainite subunits [33].

The residual austenite at the isothermal holding temperature can be determined using Equation 2.5:

$$V_\gamma = 1 - V_B \tag{2.5}$$

Where, V_γ and V_B are the volume fractions of residual austenite and bainitic ferrite respectively. Therefore, the volume fraction of martensite upon cooling can be deduced using Equation 2.6:

$$V_{\alpha'} = (1 - V_B) - V_\gamma \tag{2.6}$$

Where $V_{\alpha'}$ is the volume fraction of martensite and V_γ is the volume fraction retained austenite. Bhadeshia et al. [34] found that the impact energy of a 0.43 C wt.% bainitic alloy (isothermally heat treated at 360 °C for 115 minutes) reached a maximum, but fell off at greater test temperature, attributed to the in-situ tempering of the martensite in the microstructure. Figure 2.9 combines the data from that alloy with the results of as quenched martensitic microstructure and a tempered martensitic microstructure, suggesting that the as quenched, untempered martensite is responsible for the toughness of the developed microstructure. Following on from this finding Bhadeshia et al. suggested from the data found that for the optimum mechanical properties, a ratio of thin film austenite ($V_{\gamma-t}$) to blocky austenite ($V_{\gamma-B}$) must be greater than 0.9.

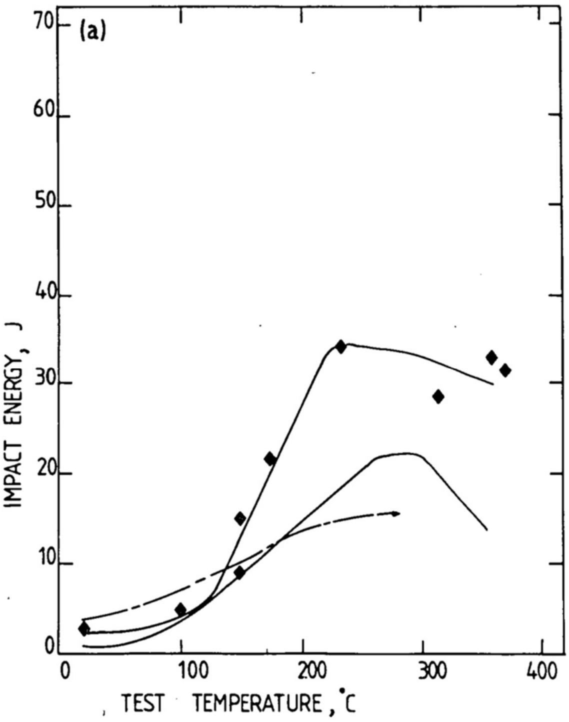

Figure 2.9: Impact transition curves of as quenched martensite (–), tempered marteniste (- -) and upper bainite (♦) [34].

Sandvik and Nevalainen [40] found similar results when testing low alloy high Si bainitic steels. During tensile testing, tensile elongation originally increased with an increasing volume fraction of retained austenite, before reaching a maximum elongation at an optimum volume fraction. A similar relationship can be seen with the toughness, measured by a Charpy V-notch test, and an increasing volume fraction of retained austenite. This is shown in Figure 2.10 (a) and (b). It is suggested that below the optimum maximum volume fraction, the retained austenite is homogenously distributed throughout the microstructure. The increase in tensile elongation up to the optimum value is attributed to the higher work-hardening rate of the austenite as compared to the bainitic ferrite. Above the optimum retained austenite volume fraction, isolated pools (which can be inferred as blocky morphology) of retained austenite appear throughout the microstructure. These pools then transform into untempered martensite and embrittle the microstructure.

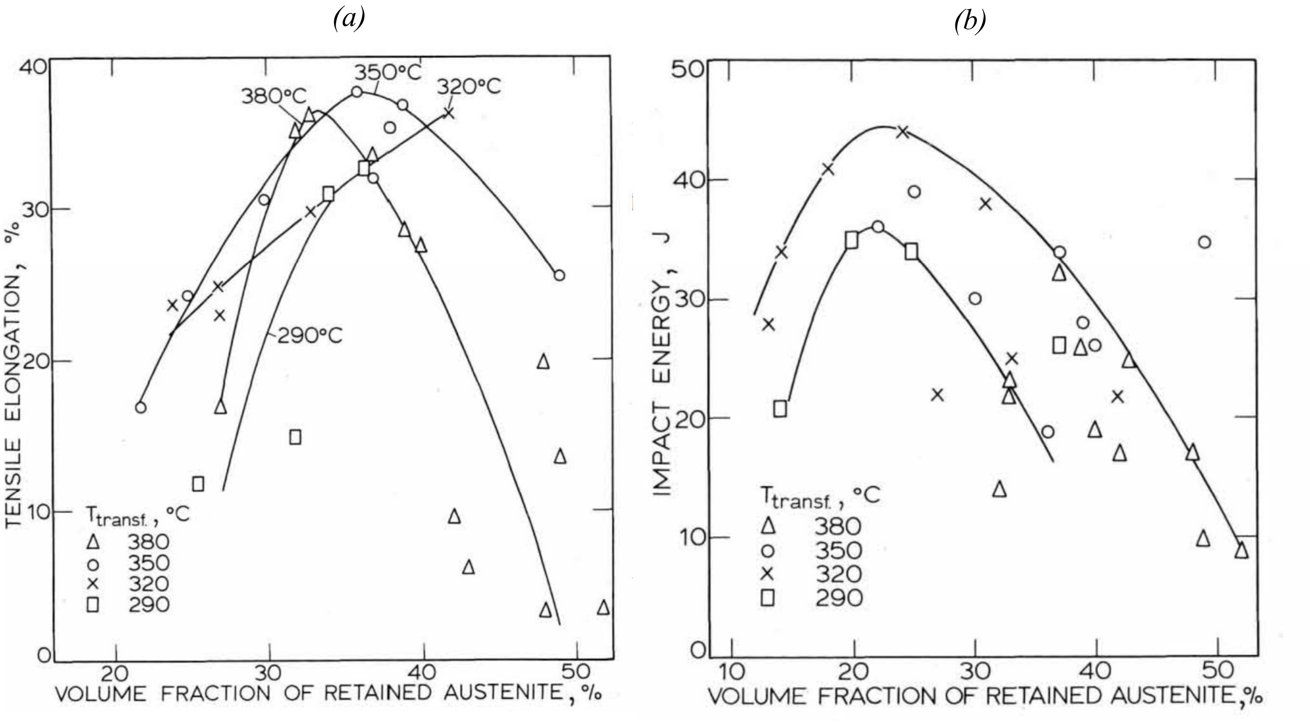

Figure 2.10: (a) Influence of retained austenite volume fraction during tensile elongation. (b) Influence of retained austenite volume fraction on Charpy V-notch impact energy [40].

Garcia-Mateo et al. [43] looked at the stability of retained austenite during interrupted tensile testing to be able to measure the volume fraction of retained austenite as compared to estimating. However, uninterrupted standard tensile tests were performed as well. The study investigated 3 different alloys at varying isothermal transformation holding temperatures and times, with the temperature ranging from 220 to 250 °C. In agreement with previous studies discussed, the study showed no correlation between the initial volume fraction of retained austenite and the tensile ductility, as shown in Figure 2.11 which was adapted by Morales-Rivas et al. [37].

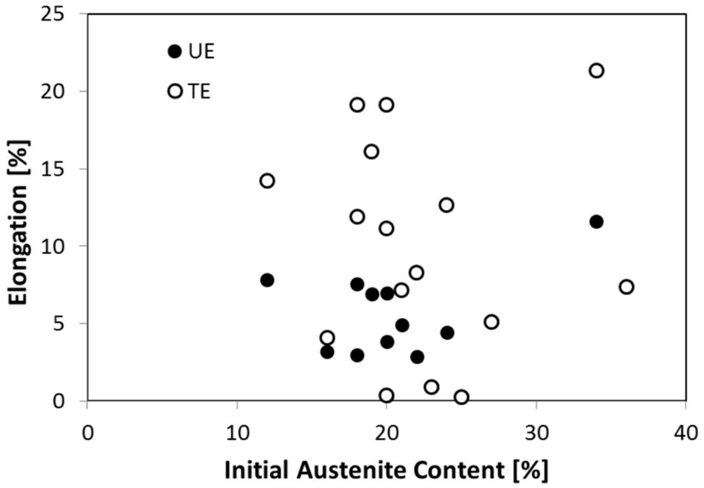

Figure 2.11: Percentage elongation against initial austenite content, for uniform and total elongation [43] adapted by Morales-Rivas et al. [37].

To link the stability of the retained austenite with the tensile ductility, Equation 2.7 was utilised for the relationship. This equation was originally developed by Pyshmintseveta et al. [44] and was used to investigate the effect of hydrostatic pressure on the TRIP effect of retained austenite in TRIP steels. $V_{\gamma 0}$ is the initial retained austenite volume fraction and V_{γ} is the measured retained austenite volume fraction after the application of deformation resulting in a percentage true plastic strain is reached, ε_p.

$$\ln(V_{\gamma 0}) - \ln(V_{\gamma}) \propto k\varepsilon_p \tag{2.7}$$

Using this equation and the measurements taken during interrupted tensile testing, Figure 2.12 illustrates the relationship for two selected steels and conditions [45]. The value for k was then calculated using linear regression to form Figure 2.13, showing percentage tensile elongation (TE,%) against k. Through the two figures, the study summarised that a low value of k is ideal for achieve larger tensile elongations (where the retained austenite is more resistant to rapid transformation and thus more stable). It was also concluded that when k > ∼0.2, the steel showed brittle fracture, with the black and white symbols in Figure 2.13 indicating ductile failures and brittle failures respectively.

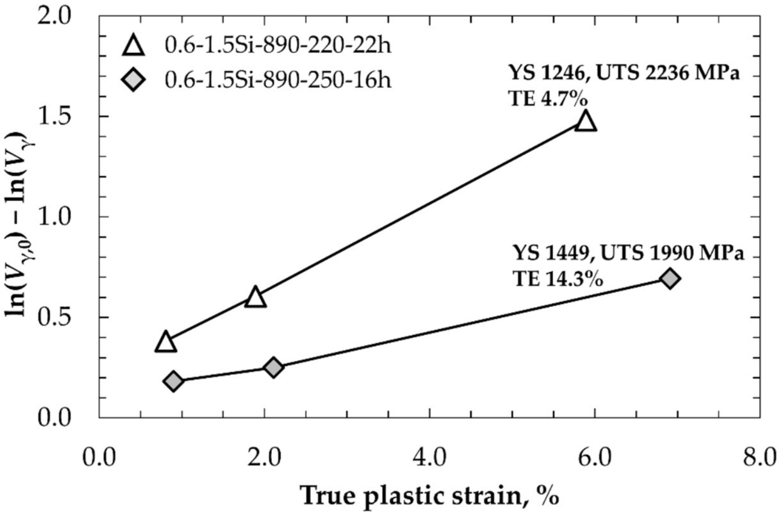

Figure 2.12: The transformation of retained austenite during plastic strain for two selected heat treatment conditions [45].

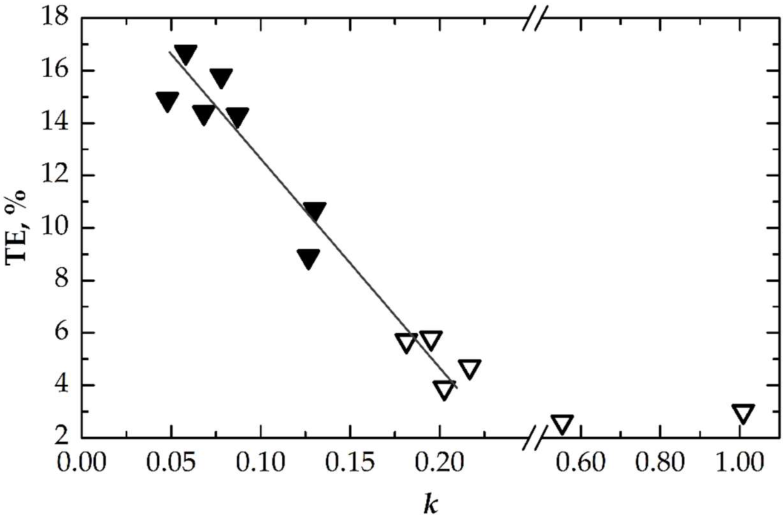

Figure 2.13: Tensile elongation against k. White symbols represent brittle failure while black symbol represents ductile fracture [45].

2.3.4 Transformation Kinetics

Nanostructured bainites can have isothermal holding times between 2 to 60 days. While the low temperature hold results in the process not being energy intensive, the long times involved do limit the applications of nanostructured bainite due to production times [46].

The transformation can be hastened by increasing the free energy associated with the austenite (γ) transforming to ferrite (α). Another method to accelerate the transformation is to refine the austenite grain size. This can be achieved by treating at a lower austenisation temperature or by deforming the austenite to increase the grain boundary area per unit volume. Garcia-Mateo and Caballero [46] utilised both approaches to reduce the bainitic transformation time of the high carbon, high silicon steel from measurements in days to simply hours. Controlled alloy additions of cobalt and aluminium were added to increase the free energy change, in addition to lower austenisation temperatures being implemented to refine the austenite grains. In later work, Garcia-Mateo and Caballero [36] reduced the amount of carbon, manganese and chromium to accelerate the transformation times. The study also investigated adding niobium to further refine the austenite grain size.

2.3.5 Two-step Austempering Heat Treatments

As previously discussed, to improve the mechanical properties of the carbide free bainites it is advantageous to have as much retained austenite in a thin film morphology as possible, as opposed to the less stable blocky morphology. In the same sense, a higher volume fraction of bainite formed during the isothermal heat treatment would also decrease the volume fraction of the polygonal retained austenite. One approach for this would be to transform to bainite at lower holding temperatures or to increase the kinetics of the reaction by the methods previously listed.

However, there has been additional work to investigate two-step isothermal heat treatments for the high silicon steels to further transform the retained austenite. Soliman et al. [47] investigated different heat treatment processing with a 0.26 wt.% C steel. The study compared the volume fraction of retained austenite and the carbon wt.% within the retained austenite of samples that underwent a one-stage isothermal heat treatment and a two-stage isothermal heat treatment. The volume fraction of retained austenite was measured using XRD and the carbon wt.% in the retained austenite was calculated using Equation 2.8, listed below. The samples were first held at 950 °C for 30 minutes, before being held at 305 °C for 6 hours and, in the case of the two-stage heat treatment, held again at 260 °C for 6 hours.

$$C_\gamma = \frac{a_\gamma - 0.3555}{0.0044} \tag{2.8}$$

Soliman et al. found that the steel specimens that underwent a two-stage isothermal heat treatment had higher yield strength than those that underwent a one-stage process. Furthermore, the additional step reduced the amount of retained austenite and increased the carbon content in the retained austenite (C_γ). A second generation bainite formed in the two-step treatment, which is finer than the first generation bainite due to the lower temperature at which it was comparatively formed at (305 °C compared to 260 °C) and the higher carbon content in the austenite it formed from. Other studies have found similar results, with Wang et al. [48] and Avishan et al. [49] noting that the second generation of bainite sheaves that formed were finer and improved mechanical properties. Although, it should be noted that the volume fraction of retained austenite must be considered in the multi-step bainitic heat treatments, as an insufficient level of retained austenite present will result in the loss of ductility that the phase typically provides.

2.3.6 Wire Drawing Retained Austenite

While studies have been done investigating cold drawing retained austenite-containing microstructures, the topic is relatively novel and has not been extensively covered.

Wiewiórowska et al. [50] produced 3 TRIP steel alloys with wt.% carbon additions varying from 0.090, 0.293 and 0.431. The three steels were cold drawn using dies with an angle of 2α = 12º. After pickling and lubrication, the wire rods were able to be drawn down from 6.25 mm to 2.97 mm, in passes of 25% reduction in area. The yield and tensile strength of the drawn wire increased with the increasing carbon in the alloys. The volume percentage of retained austenite was measured post heat treatment, prior to wire drawing, with results compiled in Table 2.1. In addition, the TRIP steels were manufactured into M5x12 screws through a forming process and then mechanically tested in this form. The study compared the mechanical properties of the TRIP steels to that of pearlitic steel, taken from the Polish standards PN-EN ISO 898-1, finding that the TRIP steel screws had both slightly higher tensile and yield strengths. The mechanically properties compared are shown in Table 2.2.

Table 2.1: The amount of percentage retained austenite for the 3 different TRIP-aided steel alloys after heat treatment [50].

Steel	**Amount of Retained Austenite (%)**
TRIP 0.090 C wt.%	7.80
TRIP 0.293 wt.%	23.95
TRIP 0.431 wt.%	28.00

Table 2.2: Comparison of mechanical properties between the TRIP Steel and a standard medium-carbon steel typically used in the industry [50].

	R_m (MPa)	**$R_{0.2}$ (MPa)**
TRIP Steel	836	678
Standard Medium-Carbon Steel	800	640

Unfortunately, the study does not go in to detail the exact heat treatment conditions utilised, making it impossible to replicate the study. Furthermore, while the retained austenite values are provided, there is no mention of how the values were calculated or obtained. Finally, it is difficult to understand the exact effect the deformation has on the retained austenite containing microstructure with the studies lack of EBSD or microscopy results.

In comparison, Yu et al. [51] aimed to investigate the deformation of a bainitic steel rod. The study utilised a composition of Fe - 1.48 Si - 2.02 Mn - 0.13 Al - 0.0028 S - 0.012 P- 0.5 C (all values in wt.%), noting the silicon addition for hindering the precipitation of carbides to produce a carbide free bainite. The work follows on from the initial findings of another study on using bainitic phase steel wire in place of high carbon steel wires [52]. However, the study utilised a much lower wt.% carbon and silicon composition (0.2 and 0.86 respectively) and a much higher chromium addition (0.94), to improve the weldability of the steel and strengthen the carbide precipitation. Yu et al. [51] were able to produce a bainitic microstructure with both film and blocky retained austenite, as shown in the SEM and EBSD micrograph in Figure 2.14. The study estimates a starting fraction of retained austenite at around 10.8%, however, it is not clearly stated if this estimate is a volume fraction.

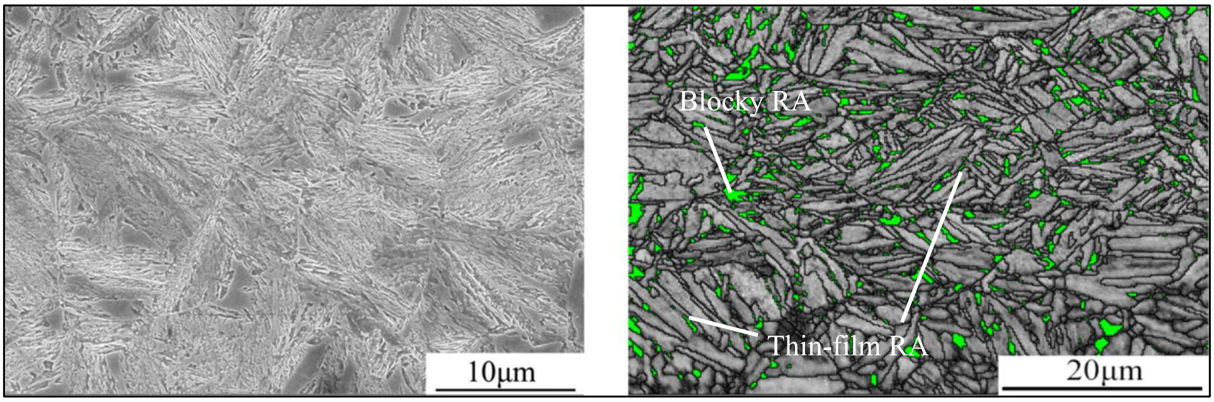

Figure 2.14: SEM image (left) and EBSD image (right) of the developed microstructure. The green in the right image is the retained austenite phase [51].

The heat treated samples were able to be cold drawn at room temperature, through 7 passes each consisting of a reduction in area of 10% from the last pass. This resulted in a total reduction in area equalling 52.2% and a total true strain reached of 0.73. The reduction in area per pass was calculated using Equation 2.9:

$$Reduction\ in\ Area\ (\%) = \frac{A_0 - A_N}{A_0} \times 100\% \tag{2.9}$$

Where A_0 is the original cross sectional area before the pass and A_N is the cross sectional area after the Nth drawing pass. The drawn wire only reached a true strain of ~0.15 before failure, which is quite low when compared to the typical drawing strains pearlitic steel wire reaches. However, the study did find retained austenite in the microstructure of the centre of the drawn samples using EBSD, taken at a true strain of 0.11, whilst only a marginal amount was observed in the wire's surface microstructure.

In addition, Yu et al. [51] described the deformation mechanisms present of the bainitic microstructure during cold drawing. The study found that the peak value of deformation was at a sub surface level, due to the surface microstructure moving in an opposite direction during drawing. The banded bainite-retained austenite (thin film retained austenite and sheaves of bainitic ferrite) preferentially bends and tilts perpendicular to the drawing direction, as shown in the SEM images in Figure 2.15 (a), (c) and (d). The schematic diagram shown in Figure 2.15 (b) is a schematic diagram of the deformation of a pearlitic microstructure for comparison.

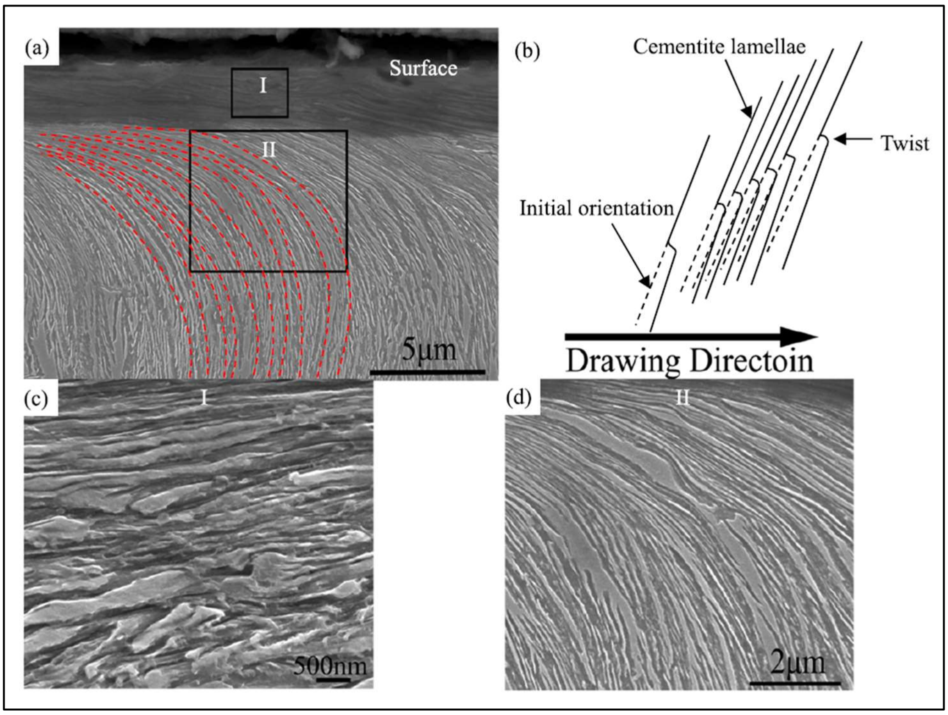

Figure 2.15: Comparison of microstructure deformation between bainite-retained austenite and pearlite (a) retained austenite-bainite; (b) pearlite; (c) larger version of region I; (d) larger version of region II [51].

During 2011 to 2013, Tata Steel and NV Bekaert worked on a collaborative project to investigate the industrial potential of bainitic wire rod. The work was authored by Hobson [53]–[55]. The aim was to investigate wire drawing a carbide-free bainitic microstructure, using large silicon additions to avoid the formation of coarse carbides that are detrimental to drawing. In the initial work, an existing high silicon rod grade, with the composition of 0.91 C, 1.21 Si, 0.51 Mn, 0.19 Cr (in wt.%), was given a bainitic heat treatment. However, the steel grade was not able to achieve a high enough ductility for the necessary wire drawing.

Following on from this, Bekaert provided a list of potential bainitic steel compositions, that would have suitable mechanical properties for high strength wire with adequate drawability [54]. The alloy compositions are shown in Table 2.3 below.

Table 2.3: List of potential alloy compositions for bainitic steel rod and wire provided by Bekaert [54].

	(wt.%)						
Alloy name	**C**	**Si**	**Mn**	**Cr**	**Ni**	**Mo**	**V**
A	0.43	2.02	3.00	0.01	0.01	-	-
D	0.22	2.03	3.00	-	-	-	-
E	0.39	2.05	-	-	4.08	-	-
F	0.32	1.45	1.97	1.26	<0.02	0.26	0.1
G	0.31	1.51	<0.01	1.44	3.52	0.25	0.1
H	0.30	1.51	<0.01	1.42	3.53	0.25	<0.005

Of the alloys listed in Table 2.3, only D and E were drawn without failing in past work. However, for future alloys, the high nickel content of E was documented to be unnecessary and too expensive, with suggestions of using larger additions of Mn as an alternative to reduce the M_S temperature. Through the mechanical data on the compositions listed and other past work done, Hobson concluded that the carbon content of the next alloy should be between 0.3 and 0.4 wt.%. Below 0.3 wt.%, the wire rod did not have ultimate tensile strength (UTS) to compete with that of pearlitic rod. It is important not to lower the carbon content too much to keep the M_S temperature as low as possible, in order to produce a fine bainitic microstructure (the 0.4 C wt.% upper limit suggested). Furthermore, a silicon addition between 1.50 to 2.00 wt.% is suggested in order to supress the formation of carbides. Finally, a Mn content in the range 1.50 - 2.50 wt.% and a Cr content in the range 0.50 - 1.50 wt.% is suggested in order to further reduce the M_S temperature. Therefore, a proposed alloy composition for further research was listed as 0.40 C – 2.00 Si – 1.00 Mn – 1.00 Cr (all in wt.%).

The proposed alloy was produced and isothermally heat treated, at a range of different holding temperatures and times. These are listed in Table 2.4 below [55]. The study found that the optimum mechanical properties were achieved when the alloy was held at 300 °C at both 3 hour and 6 hour holding times. This was as expected from the past research, as this temperature is only slightly above the calculated M_S temperature of the alloy at 285 °C. The percentage of retained austenite in the two conditions was then assessed using XRD and EBSD on SEM samples. The EBSD technique utilised by the study, had a resolution of 0.1 µm and therefore could not detect any retained austenite smaller than this, leading to a lower a prediction of the percentage of retained austenite present. The determined values acquired using both techniques are listed in Table 2.5 and Table 2.6.

Table 2.4: Showing the holding temperature, times and Vickers hardness results (HV30) [55].

Holding Temperature (°C)	Holding Time (Hours)	Hardness (HV30)
300	3	513
	6	510
325	3	469
350	2	435
	16	421
375	2	495
400	2	633

Table 2.5: Measured retained austenite volume fraction after 3 and 6 hours, determined using XRD [55].

Measured Retained Austenite Results using XRD	
Holding Time at 300 °C (Hours)	Retained Austenite (Volume Fraction, %)
3	16.0
6	15.1

Table 2.6: Measured retained austenite volume fraction after 3 and 6 hours, determined using EBSD [55].

Measured Retained Austenite Results using EBSD	
Holding Time at 300 °C (Hours)	**Retained Austenite (Volume Fraction, %)**
3	8.7
6	9.5

As shown, the study found no significant difference in the amount of retained austenite between the 3 hour and the 6 hour held samples. Therefore, the bainitic wire rod that was cold drawn and tested utilised a 3 hour isothermal holding step. Samples from the heat treated material were then tensile tested to assess the suitability of the material for further wire drawing. Table 2.7 shows the results, where the results are compared with Steel D and Steel E, two past experimental steels with measured retained austenite fractions that were successfully drawn.

Table 2.7: Comparing steel 1 and 2 with two past steels that were successfully drawn down to wire from rod [55].

Sample	**UTS (MPa)**	**0.2% Proof (MPa)**	**Reduction of Area (%)**	**Elongation on 5D (%)**
1	1521	1156	50	13
2	1502	1229	60	13
Steel D	1420	1060	52	22
Steel E	1610	1350	56	12

The wire rod was successfully cold drawn through 12 passes, before finally breaking at a total drawing reduction in area of 70% was reached. Limited sample material meant that wire samples were only taken at drawing diameters of 4.43 mm and 3.30 mm. SEM and EBSD images taken of the samples after drawing show that most of the retained austenite seemed to have transformed. Hobson notes that the while the fine retained austenite has deformed in a ductile matter, the larger more polygonal blocks of the phase did not deform as easily and that some appeared to have transformed into martensite. Figures 2.16 and 2.17 show the SEM and EBSD images of the drawn bainitic wire respectively.

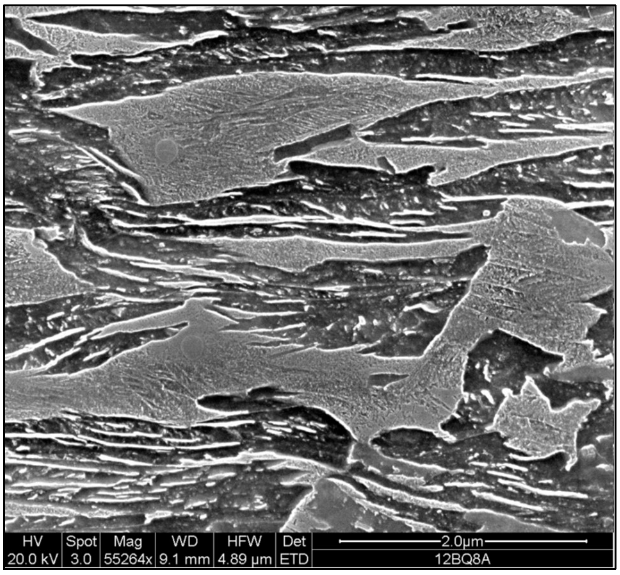

Figure 2.16: SE-SEM images of the drawn bainitic wire [55].

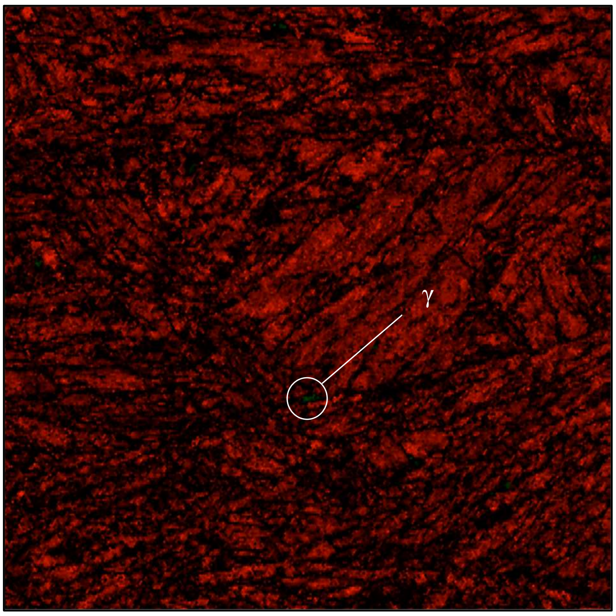

Figure 2.17: EBSD image of the drawn bainitic wire. The bainitic ferrite is shown in red and the retained austenite is shown in green [55].

2.4 Quench & Partitioned Steels

Carbon partitioning has been well documented since 1960 when Matas et al. [56] first reported the process occurring between ferrite and austenite during transformations. However, the full benefits of stabilising retained austenite were not well realised until the development of advanced high strength steels (AHSS). These steels utilise retained austenite and its ability to transform into martensite during deformation, through either TRIP or twinning induced plasticity (TWIP) reactions, to achieve both high strength and high ductility properties. This called for a heat treatment that was able to stabilise the austenite and lower the martensitic start temperature (M_s), in order to have a large amount of the phase present post heat treatment.

This led Speer et al. [57] to develop the “quench and partitioning” (Q&P) process. As the process name suggests, the heat treatment involves initially quenching the austenite to below the M_S temperature in order to form a martensitic-austenitic structure. Once quenched the steel is then heat-treated at a temperature between the M_s and the martensitic finish temperature (M_f), though the steel can be held just above M_s in order to encourage partitioning of the carbon between the martensite and the retained austenite. Figure 2.18 below is a schematic diagram of the heat treatment, in order to better visualise the process [58].

Initially it was deemed that carbon partitioning at such low temperatures would have little effect, as the rate of diffusion of the carbon atoms would be too low and the formation of carbide precipitates would dominate instead. However, the process was possible in Si containing steels where the formation of carbides is suppressed [59]. As such, Speer et al. [57] worked to develop a model of the transformation and suggest favourable conditions for partitioning. The model was more concerned with predicting an “endpoint” for the reaction, than the exact kinetics involved.

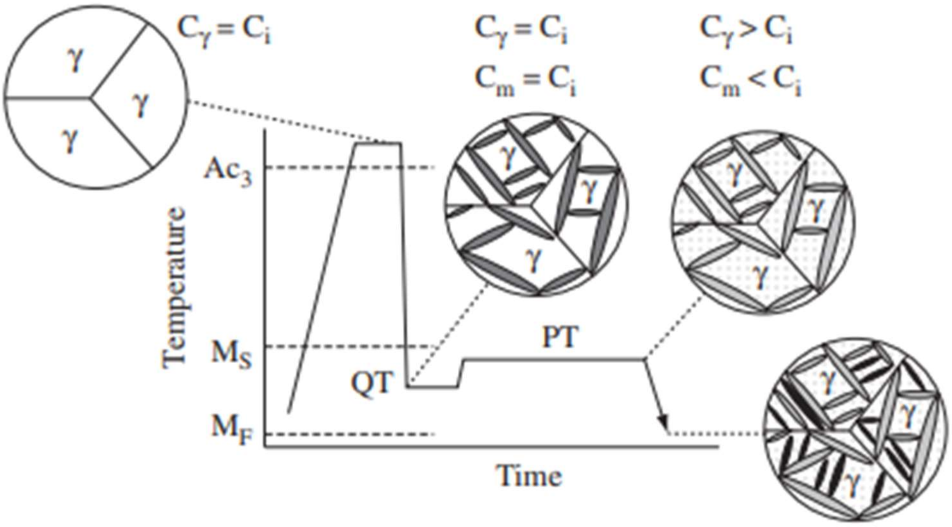

Figure 2.18: Schematic diagram of the Q&P heat treatment process. C_y, C_i and C_m represent the carbon concentrations for the austenite phase, the initial alloy, and the martensite phase respectively. The grey regions represent the martensite phase [57].

The model that was created involved a metastable condition known as constrained paraequilibrium (CPE). Similar to the paraequilibrium condition, the metastable condition is where there is no long range movement of substitutional atoms between the martensite and ferrite phases, however carbon and other interstitial atoms are able to move freely. In the constrained condition, there is no movement of substitutional atoms over a short range either (distances smaller than a unit cell length) at any interface between the phases. In addition, CPE also applies to high order alloys as well as binary Fe-C alloys, unlike paraequilibrium. Through their model and work, Speer et al. [57] showed that the composition of the austenite and ferrite phases in CPE was dependent on numerous factors including: composition, phase fractions and temperature. The amount of carbon present in CPE ferrite was also shown to increase proportional to temperature, whilst the austenite carbon concentration decreased.

When compared to carbide-free bainitic steels, Q&P steels can achieve greater strengths due to the enrichment and stabilisation of the retained austenite [60], [61]. Speer et al. [57] additionally notes that the partitioning involved in bainitic steels is more heavily linked to the isothermal heat treatment (T_0). Both bainitic-ferrite growth and partitioning in these alloys are linked together in the bainitic process, whilst the Q&P process allows for a much greater amount of control over the final microstructure achieved as only carbon diffusion needs to be present. They argue that the ability to simply focus on the carbon diffusion allows for a much larger range of intermediate temperature processes, alloying addition options and designed quenched microstructures prior to partitioning.

Maheswari et al. [62] investigated alloy additions that could be utilised for Q&P steels. Whilst past work had been that looked at effect of differing levels of Si and Al additions in the steels [63], the exact effect of the additions was still not well established. Their aim was to vary the C, Si, Mn and Al additions in 3 different steels, to investigate which combination had the best physical properties and ability to stabilise the retained austenite. The compositions are listed in Table 2.8 below.

Table 2.8: Table of the different steel alloy compositions used by Maheswari et al. [62].

	(Wt.%)			
	C	**Mn**	**Si**	**Al**
Steel A	0.29	1.22	1.65	1.62
Steel B	0.26	1.57	1.06	0.98
Steel C	0.22	1.85	0.41	1.46

The study helps demonstrate the importance of the Mn addition, as Steel A (whilst containing the highest amount of all the other additions) had 50% of its retained austenite transforming after deformation. Whilst this resulted in a high strength, it also preceded a brittle failure due to the formation of martensite during deformation. Steel C with the largest Mn addition had the best ductile properties, having an elongation of 24.4% as compared to the 14.5% reached by Steel B.

Typically, Q&P steels contain large additions of silicon (~2 wt.%) in order to suppress carbide precipitation and promote carbon partitioning into the austenite from the martensite. One study performed by Kim et al. [64] investigated the effect of Si addition content on the Q&P microstructures of martensite and retained austenite. Two alloys containing 0 and 1.98 wt.% Si were utilised for the study. Using atom probe topography (APT) and EBSD, carbide precipitation was found to occur in both steel alloys after processing. In addition, no carbon partitioning is observed without the presence of silicon.

Yan et al. [65] studied the effect of intercritical annealing on the microstructure of Q&P treated steel samples. During a typical Q&P heat treatment, the steel samples are held for some time at a temperature above the Ac_3 to allow for full austenisation. However, during an intercritical anneal, the steels are instead heat treated at a temperature between the Ac_1 and Ac_3 temperatures to provide an initial austenite fraction. The study found that intercritically austenised steels contained larger amounts of retained austenite in a block morphology, as opposed to the film-like austenite grains found in the fully austenised treated steels. The change in morphology resulted in a decrease in strength as partitioning times increased observed in the intercritically annealed steels, due to the decreased stability of the polygonal retained austenite. This detail in combination with the lower fractions of retained austenite present in the samples, resulted in the fully austenised Q&P steel samples having much higher strengths but lower elongation properties than the intercritically austenised Q&P steels.

However, there is still work to be done on optimising the microstructure, specifically the amount of retained austenite. For example, whilst the crack growth resistance increases with increasing amounts of retained austenite [61], Wang et al. [66] found that the optimum amount of retained austenite for the largest possible total elongation was 11%. Wang et al. also noted that although the largest amount of retained austenite that could be obtained was when the microstructure contained 40% martensite, this did not correspond to the highest elongation results. They also concluded that at low initial martensite fractions, yield strengths were low as less carbon was available to stabilise the retained austenite. However, the work hardening rate was a lot higher and the rate decreased with increasing initial martensite fractions. Thus, it was shown that the mechanical properties, ultimate tensile strength, yield strength and ductility were all highly dependent on the retained austenite fraction, the phase's stability and morphology. Similar to bainite [67], [68], the morphology of the retained austenite is critical in Q&P steels. Once again, the aim is to achieve thin fine films of austenite, as the phase is much more stable in this morphology than in a more polygonal form [61], [69].

2.5 Summary

This chapter provides an introduction into pearlitic steel wire and cold wire drawing, and highlights the issue of the dissolution of cementite. Quench and partitioned (Q&P) steels and carbide free bainitic steels are discussed as potential alternatives for high strength steel rod and wire.

Carbide free bainitic steels (commonly referred to as nanostructured bainitic steel) have a good combination of both strength and toughness. The microstructure is composed of bainitic ferrite and carbon enriched retained austenite. Although the long isothermal holding times involved limits the industrial usage of the process, work by Garcia-Mateo and Caballero [46] have found ways to accelerate the transformation times. This has been utilised when investigating carbide free bainites to increase the volume fraction of bainitic ferrite present in the microstructures developed.

Q&P steels are formed by quenching to below the martensitic start temperature, Ms, before holding at a temperature slightly above the Ms temperature to encourage the carbon to partition into the austenite to stabilise the phase.

This literature review found that it is essential to avoid the formation of polygonal (also referred to as “blocky”) retained austenite for both of the alternative microstructures, as this morphology is less stable than thin-film retained austenite [34, 48, 61, 62]. This leads to the unstable retained austenite transforming into untempered martensite through a TRIP effect, which has a detrimental effect on the ductility of the steel [34]. Avishan et al. [49] and Wang et al. [48] found that utilising a second isothermal holding step during the bainitic heat treatment can improve the mechanical properties of nanostructured bainites by transforming some of the polygonal retained austenite. This knowledge was used during this thesis project, to minimise the amount of blocky retained austenite present in the nanostructured bainite, by performing a secondary isothermal holding step.

3.0 Experimental Methods

This chapter reports on the main experimental methods utilised to investigate the research aims highlighted previously. These methods focused on creating new steel alloys and processing routes, to produce and investigate nanostructured bainite and stabilise the retained austenite present in the microstructure. The section initially discusses how the alloy ingots were processed from cast steel ingots to axisymmetric samples. Later the heat treatment techniques and mechanical testing are discussed, before concluding with the microscopy and x-ray diffraction techniques utilised.

3.1 Alloy Processing Route

3.1.1

Table 3.1 shows the two alloys that were utilised for the quenched and partitioned (Q&P) work, discussed in Chapter 4. The steel rods were remaining from past research performed by Lifen Deng for British Steel [70]. Utilising these compositions provided a strong starting point for investigating both Q&P steel rods and microstructures containing retained austenite, while providing more time to developing a processing route to produce new cast steel ingots.

Table 3.1: Steel compositions of the rods utilised in the past Q&P work and in the EngD project. RT stands for room temperature [70].

	Alloy Composition (wt.%)								
Rod No.	**C**	**Si**	**Mn**	**S**	**P**	**N**	**Cr**	**M_s (°C)**	**M_f (°C)**
9JF10	0.305	1.96	1.02	0.009	0.010	0.006	0.005	316	149
9JF13	0.490	0.97	1.96	0.009	0.010	0.006	0.020	238	< RT

The steels were produced by vacuum induction melting (VIM) at Tata Steel Swinden Technology Centre (STC). The cast ingots were forged to 50 mm square bars and subsequently hot rolled to 12.7 mm diameter rods. The rods were then cut and centreless ground, to produce 11 mm diameter rods of 300 mm in length.

3.1.2 VIM Casting

Table 3.2 shows the different alloys that were produced throughout the course of the EngD project. BAIN 0 was utilised for the work discussed in Chapter 5, while BAIN 1-4 were utilised for the work discussed in Chapter 6.

Table 3.2: The different alloy compositions of the 5 steel alloys produced for the project.

Steel	**C**	**Si**	**Mn**	**Cr**	**M_s (°C)**
	(wt.%)				
BAIN 0	0.40	2.00	2.00	1.00	285
BAIN 1	0.40	2.00	0.75	0.50	343
BAIN 2	0.40	2.00	1.25	1.50	295
BAIN 3	0.50	2.00	0.75	0.50	300
BAIN 4	0.50	2.00	1.25	1.50	251

Each of the alloy casts were produced using the Consarc vacuum induction melting (VIM) machine in the Royce Discovery Centre. The machine utilises a 35 kW medium frequency (up to 10 kHz) induction generator to melt the charge in the crucible, and is capable of melting 10 kg of steel, cobalt or nickel-based alloys. The alloy composition of BAIN 0 (the first ingot produced) was investigated using an optical emission spectrometer (OES). OES utilises a sparking process to vaporise and ionise a small portion of the material sample. The emitted light from the process is then analysed by a spectrometer to detect the characteristic optical emission light from the different elements present.

To cast the 5500 g ingots, the alloy components were initially weighed using a scale to a precision of 0.1g. The charge was made up of electrolytic iron flakes, graphite flakes, FeCr, FeSi, and FeMn ferroalloys. An additional 10 wt.% of FeMn was added to compensate for losses due to evaporation. Approximately 3.5 kg of iron and FeCr were placed in the Al68S one-shot liner (Capital Refractories). This accounts for around 80% of the crucible capacity, due to the low packing factor of flakes. The rest of the alloy components were placed in the addition buckets to be introduced into the molten alloy during the melting process. A copper base and steel plates were used to build a cavity with an 80 x 80 mm^2 footprint. The internal surfaces of the steel plates were lined with BN to prevent alloy weld during casting. The chamber was evacuated to 5×10^{-4} mbar using the vacuum pumps and the induction power was turned on at a low setting to prepare the crucible. After drying and heating the crucible slowly at a low power setting, the induction power was gradually increased until the charge was melted. The chamber was then backfilled with argon to suppress the evaporation of the elements to be added (i.e., Mn and Cr). The remaining charge material was added by lowering the steel buckets into the additions chamber over the crucible, holding the molten metal in the melting chamber. Once the charge was completely melted, the temperature of the molten alloy was raised to 1550 °C. The alloy was magnetically stirred at that temperature for 5 minutes, before being cast into the mould.

There were two main concerns prior to rolling the ingots: porosity in the ingots and a shrinkage cavity present on one end of each of the ingot. To address these concerns, the initial ingot cast was ultrasonically tested by British Steel's R&D department where it was found that the casting defect did not extend more than 25 mm into the ingot and that the ingot appeared to be fully dense. Therefore, the shrinkage defect was removed from each ingot by machining past this cavity depth. The ingots were then sectioned into two halves, to reduce the required rolling loads. The sectioning helped to reaffirm that the ingots were pore free, as no visible cavities or pores could be observed. Figure 3.1 shows the cast ingot and the shrinkage cavity present on one side.

Figure 3.1: Images of the cast steel ingot, including the casting defect on the edge.

3.1.3 Hot Rolling

To homogenise the cast microstructure the ingot sections were initially held for 2 hours in a furnace preheated to 1150 °C, to transform the steel into the austenite phase. Each section was approximately 78 mm by 78 mm, by approximately 50 mm in length (varying on the length of the ingot post the shrinkage cavity sectioning) after machining off the shrinkage cavity and sectioning. The 2 hour holding time was to ensure the centre of the sections reached the required treatment temperature. A general rule-of-thumb for heat treating cast ingots is to hold the ingots for 1 hour per 25 mm thickness.

The first alloy processed was rolled using the FENN-MODEL 081 hot rolling mill at the University of Sheffield. To reduce rolling load, the section rolling thickness was taken as the shortest length of the ingot (~ 50mm). The heat treatments were initially performed by the thermomechanical compression machine (TMC) in the university, due to the large amount of control the machine allows the user over the quenching rate and the additional ability to perform cold or hot compression testing. Each section was hot rolled to a final thickness of 11-12 mm, allowing for additional material for machining the 10mm diameter axisymmetric samples out of the rolled slabs. This was achieved by rolling in reductions in thickness of 10mm, resulting in 4 total rolling passes required. At the time, the heated rolls on the hot rolling mill were not functioning, therefore cold rolls were used. The address the heat loss from the workpiece and to reduce the rolling loads, the slabs were reheated between passes for 10 minutes at furnace temperature of 950°C. After rolling the slabs were air cooled. Figure 3.2 shows a schematic diagram schematic diagram of the processing route to transform the steel cast ingot into axisymmetric samples. Figure 3.3 shows a schematic diagram of the orientation of the axisymmetric samples that were machined out of the rolled steel slabs. Table 3.3 shows the rolling schedule that each of the ingot sections received.

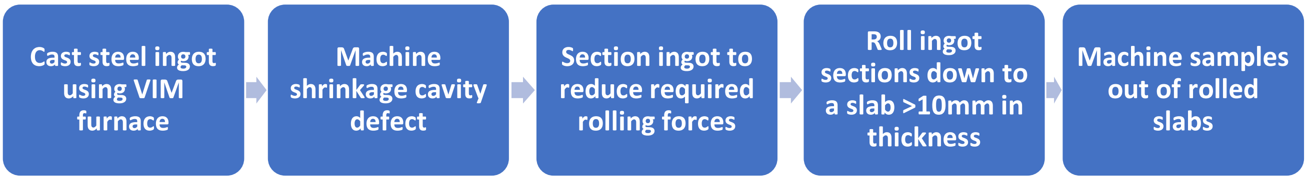

Figure 3.2: Schematic diagram of ingot processing to PSC samples.

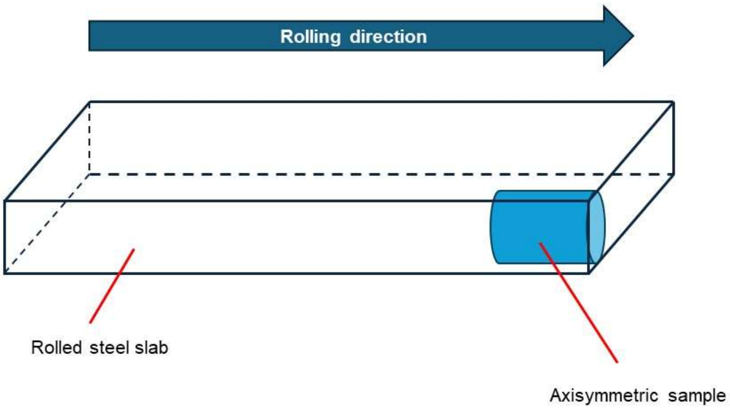

Figure 2: Schematic diagram of the axisymmetric samples position within the rolled slab, prior to removal by machining.

Table 3.3: Rolling schedule for the ingots.

	H_o	H_f	% Reduction in thickness
1st roll pass	50	40	20
2nd roll pass	40	30	25
3rd roll pass	30	20	33
4th roll passs	20	10	50

Unfortunately, technical issues with the hot rolling mill at the university arose such that alternative facilities had to be found. The Steels and Metals Institute (SAMI) rolling facilities at Swansea University was used for the remaining 4 alloy castings. The sections were given a prior heat treatment and rolling schedule similar to the aforementioned one. However, the facilities at Swansea were able to perform hot rolling by heating the rolls, therefore avoiding the need to reheat the slabs after each rolling pass. This also allowed for a final rolling temperature to of 950°C to be specified. Figure 3.4 shows one of the rolling slabs produced using the facilities at Swansea.

Figure 3.4: Image of one of the hot rolled steel slab.

3.2 Isothermal Heat Treatments

The two microstructures that the project investigation focussed on producing, namely Q&P and carbide free bainitic steels, relied on long isothermal holding times at temperatures very close to the martensitic start (M_s) temperature. The facility required for these process routes had to have close temperature control, in both the holding and quenching steps, with the added ability to hold the steels for many hours. The heat treatments were therefore achieved using two main methods: utilising the thermomechanical compression machine (TMC) and molten salt baths located at the University of Sheffield and Summitglow Ltd respectively.

3.2.1 Thermomechanical Compression (TMC) Machine Heat Treatment

The thermomechanical compression (TMC) machine is designed to perform plane strain compression and axisymmetric compression testing, at a wide range of temperatures. The specimens are held using a robotic arm and thermocouples placed into the specimen to control and log the temperature during testing to the PC. The thermocouples were calibrated for high temperatures with an Isotech Pegasus-T. The TMC has two thermal treatment areas, the test furnace and the fast thermal treatment unit (FTTU).

The test furnace is where the two tools used for compression testing are located. The tools can be heated within the test furnace to perform compression testing at a specified temperature. The top tool height is controlled by hydraulics. Over long holding periods, the hydraulic oil can overheat due to lack of sufficient cooling. To avoid this issue, all the heat treatments were performed using only the FTTU.

The FTTU consists of both a quenching and heating unit, where heating is controlled by induction coils. The FTTU can quench using air, water mist or water spray to decrease the specimen temperature. The two tools for the compression testing are located in a separate test furnace. The tools can be heated within the test furnace to perform compression testing at a specified temperature. The top tools height is controlled by hydraulics. Over long holding periods, the hydraulic oil can overheat due to lack of sufficient cooling. To avoid this issue, all the heat treatments were performed using only the FTTU.

3.2.2 Salt Bath Heat Treatments

Both the initial work on quench and partitioned steels and the work on the carbide free bainites, BAIN 1-4, were heat treated using molten salt baths. The baths are located at Summitglow Ltd and allow for large amount of control on the temperature and quench rate conditions.

To heat treat the quench and partitioned steels, 4 different molten salt bath steps were required. The steel alloys were first submerged in a relatively low temperature salt bath (~300 °C) before being moved into a much hotter salt bath at 950 °C for the austenisation heat treatment. This avoids the steels causing the hotter bath to “spit” out molten salt, due to sudden temperature difference between the steel and salt bath. After holding, the steel was then moved into a low temperature salt bath to quench the steel, before quickly being moved to a slightly higher temperature salt bath for the isothermal holding step. No thermal couples could be utilised to monitor the program, as the facilities did not exist and the multiple transfers between baths proved it very difficult to setup a portable thermocouple system. It was attempted, but spillage of molten salt on the equipment proved it unfeasible.

The multitude of baths required, and the lack of thermal data originally lead the project to try and use the TMC instead for the heat treatments. The added benefit was that the TMC could also compression test the samples, providing mechanical data without the need for further machining. The TMC thermocouple readings additionally allowed for a complete temperature log to be produced for the process. However, the issue that was later discovered was that the TMC could only provide a heat treatment for one sample at a time, as the robotic arm needed to grip each sample individually. With multiple samples needed for statistical mechanical data and microscopy specimens, it was later decided to return to the salt bath heat treatment to allow for multiple processing of samples. The axial symmetric samples that were machined still allowed for compression testing using the TMC and that this alternative heat treatment was still available if any external factors intervened with access to the Summitglow Ltd salt baths.

3.3 Thermomechanical Compression Testing

As discussed, the TMC machine was operated to perform compression testing and gain stress-strain data on the different heat treated alloy samples. The machine can perform either plane strain or axisymmetric compression tests, at temperatures ranging between room temperature and 1100 °C. Before testing, the samples were placed within the robotic arm, thermocouples were attached in the pre-drilled holes, and boron nitride spray was used as an anti-stick barrier. The tools are made of a nickel-based superalloy (M22), which consists of 71 wt.% Ni, 6 wt.% Cr, 2 wt.% Mo, 11 wt.% W, 3 wt.% Ta, 6 wt.% Al, 0.6 wt.% Zn and 0.13 wt.% C. During testing, the bottom tool is still while the top tool is moved downward by hydraulic systems to deform the sample, placed by the robotic arm between the tools. The TMC can produce a maximum strain rate of 200 s^{-1} for 10 mm initial thickness specimen and can reach a maximum engineering strain of 2. The axisymmetric compression samples had dimensions of 10 mm in diameter and 15 mm in length, with 1.1 mm thermocouple holes drilled at centre height and width, at a depth of 5 mm. Figure 3.5 show the machining drawing for these sample.

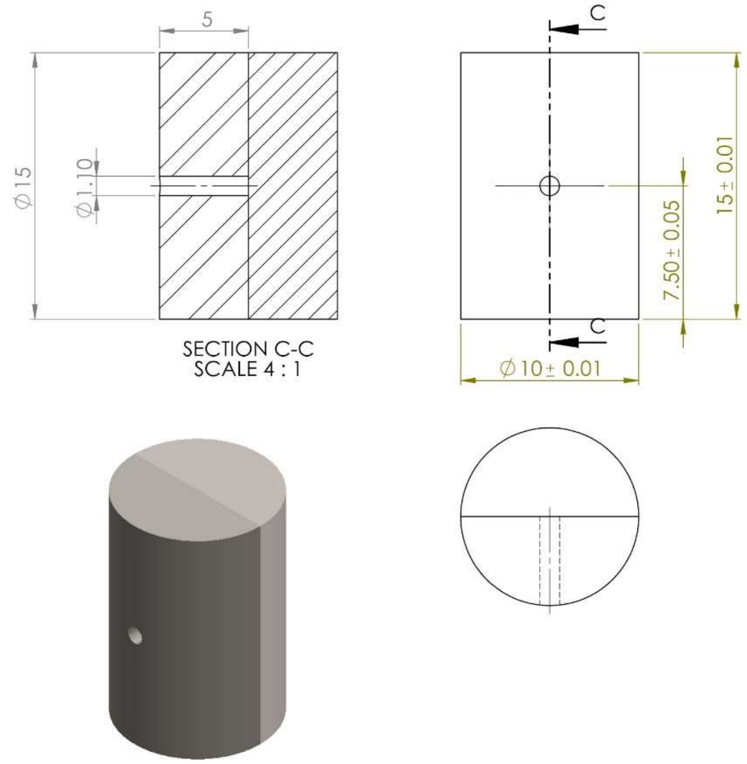

Figure 3.5: Engineering drawing of the axisymmetric samples.

3.4 Specimen Preparation

Specimens for microscopy were prepared using one of the two different methods: one involving the sample ground, polished and etched encased in Bakelite, the other one producing a thin film sample to be electropolished for TEM. Most of the specimen preparation was done within the micro-preparation laboratory in the Material Science and Engineering Department at the

University of Sheffield. However, electropolishing and the fume cupboard utilised for the operation were within the Sorby Centre. It should be noted that for both specimen preparation routes, the samples have a high affinity to oxidise and therefore it is best to prepare the samples and perform the necessary microscopy all in the same day. If possible, the samples should be stored in isopropanol filled containers and the containers under a vacuum.

Specimens were sectioned using either a hand operated saw, the Buehler Abrasimet, or by one of the two automated saws, the Struers Secotom-20 or Secotom-50. The type of saw utilised depended on the initial specimen size and the sample size needed to be sectioned. The Secotom saws provided much more precise cuts and were typically used to produce the final sample cuts before grinding and polishing. However, the machines cut much slower and therefore larger initial specimens were first sectioned using the Abrasimet. Longitudinal sections were taken from the axisymmetric samples that were deformed under compression, to assess the microstructures obtained after deformation. Figure 3.6 shows that the sections were taken from the plane parallel to the direction of compression.

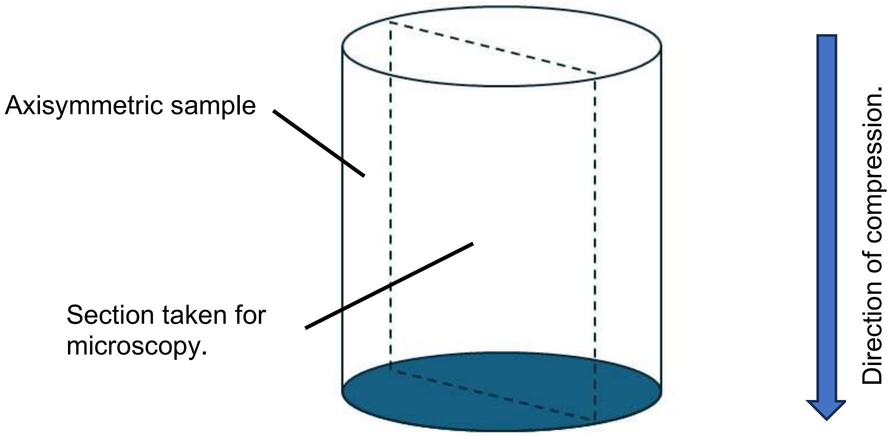

Figure 3.6: Schematic diagram showing the orientation of the sections taken from the axisymmetric samples for microscopy.

3.4.1 Bakelite Samples

Mounting the sectioned samples in Bakelite is the most common route used. This allows multiple mounted samples to be held within the AutoMet™ Grinder Polisher machine to be ground and polished, to produce a flat and highly polished surface for optical and scanning electron microscopy (OM and SEM respectively). The sectioned pieces were mounted in conductive Bakelite (as non-conductive Bakelite is not suitable for SEM) using the Buehler SimpliMet machine. The mounted samples were then wet ground using a range of SiC grinding papers to remove scratches, using increasingly finer paper with a finishing grit size of 1200. Once ground, the samples were then polished using 6µm and 1µm diamond-based paste for 10 and 5 minutes respectively. At this stage it should be noted that no water should be utilised, and the samples must be cleaned solely with isopropanol. Finally, the samples were etched using 2 vol.% Nital, using a swab to carefully apply the etchant using the change in surface colour to decide when the etch has occurred. The reaction is stopped by submerging the samples in isopropanol, before inspecting the etch using optical microscopy. If the etch is insufficient, more Nital is applied with a swab. Under-etching is a better practice in these steps, as over-etching meant that the samples must be repolished before further etching.

3.4.2 Thin Film Samples

Thin film samples are necessary to produce samples that could undergo transmission electron microscopy (TEM). The samples need to be electropolished to produce a hole, resulting in regions thin enough to be observed using TEM. The initial thickness of the disc specimens needed to be <100 µm. The samples were punched out of a thin film of this thickness for electropolishing, to create samples that are 3mm in diameter.

To make these thin films initially, sectioned steel specimens were glued to small holding stubs. The glue can be melted easily on a hot plate so that the specimen's thickness can be readily checked. The specimen is then ground on the SimpliMet machine by hand, using multiple rough SiC paper typically around grit size 120 and 240 and water. The impact of oxidisation at this stage is not as large as earlier, as these samples will be electropolished which will remove the oxidised surface. A small barrier of blue tissue roll can be put to surround the drain (not cover the drain) under the plate helps to reduce the risk of sample loss (however, it does not eliminate it). Every 5 minutes of grinding, the specimen is unglued using the hot plate and flipped, before receiving more grinding. When the film begins to lose noticeable outer sections, it is best to move to grinding the remainder of the thickness by hand using a much lower rotation speed on the machine and wearing finger gloves. If the thickness is still >200μm, it is best to continue using the stub method with perhaps lower speeds. Either way, any loss in material should indicate the need to use finer SiC paper with a grit size 400. As previously mentioned, a final thickness of <100μm needs to be achieved for TEM samples. However, EBSD samples prepared in the same way have less strict final thickness requirements. This is due to these samples being electropolished but without the need to produce a hole in the film samples, therefore the only thickness requirement is to be able to punch the 3mm diameter samples out of the film.

3.4.3 Electropolishing

The 3mm diameter samples were thinned further using twin-jet electropolishing with the Struers TenuPol machine. The electropolishing electrolyte consisted of 30 ml perchloric acid, 370 ml 2-butoxyethanol and 600 ml methanol. The 3mm metal disc samples were placed in the twin-jet thinning holder, which was then placed into the TenuPol machine. The electropolishing process stops automatically when light is detected passing through the sample but can be manually stopped at any time. The voltage utilised for electropolishing varied between the samples from 21 to 27 V, where the polishing voltage was determined as a scan.

The voltage chosen was to produce a steady current between 30 to 40 mA, so that the sample surface was not etching. The electropolishing was always performed at a temperature of -35 °C. Any water present would cause issues with the electrolyte and as such, all parts of the TenuPol and the holder were cleaned using methanol. For TEM samples, the process was stopped at the point at which a hole forms in the disc samples, determined when a set amount of light is detected to pass through the hole in the sample. For EBSD samples, the process was stopped after 1 minute and 30 seconds, to allow for adequate polishing. The electropolished disc samples were then assessed using optical microscopy.

3.5 Characterisation Techniques

3.5.1 Scanning Electron Microscopy

Scanning electron microscopy (SEM) was essential to study the fine microstructures achieved through the various heat treatments. Secondary electron (SE) SEM images were taken using a FEI Inspect F50, field emission electron gun (FEG) machine, operated from a range of 15 to 20 kV, to try to observe more of the microstructure surface whilst not compromising the resolution of the image. Some images were taken using the SEM located at the British Steel R&D department, however, the SEM could not produce high quality images past a magnification of 20,000x because of the tungsten electron source. All the images were taken using a spot size of 3.5, a working distance greater than 10 mm and in secondary electron imaging mode. The specimens were prepared using the method listed in 3.3.1.

3.5.2 Transmission Electron Microscopy

Transmission electron microscopy (TEM) is a key microscopy technique that uses the transmission of high energy electrons through thin sample areas. The transmitted electrons then form an image onto a fluorescent screen or a detector. The technique is essential for looking at nano-scale microstructures, for example the presence of carbides or thin film retained austenite. A similar technique performed was scanning transmission electron microscopy (STEM). Like SEM, this technique utilises a focussed scanning electron beam to produce high resolution images, however, using transmitted electron rather than secondary or backscattered electrons. The microscope can also form diffraction patterns of the scattered electrons through the crystal lattice. This allows for crystallographic data such as the lattice parameter of the phase or the type of unit cell.

Energy dispersive X-ray spectroscopy (EDS) was used to analyse the composition of different phases present in the images. During both SEM and TEM, high-energy electrons interact with atoms on the sample surface. This can cause the ejection of an inner-shell electron from the atom. A high energy electron from the outer-shell of the atom will then move to the inner-shell to fill the vacancy. This electron will then release the excess energy in the form of an X-ray. The X-rays emitted by this event are unique for each element, therefore this can be used to create elemental maps of samples by measuring the energy and intensity of the X-rays for each pixel.

The TEM, STEM and EDS work was performed utilising the JEOL JEM F200. The microscope uses a cold field emission gun (CFEG) source and an acceleration voltage of 200 kV. It has a point resolution: 0.19 nm, a magnification ranging from 30 to 2,000,000 X and can perform elemental analysis using either dual EDS detectors (SDD) or Dual EELS (Quantum GIF). TEM samples were prepared using the method listed in 3.32 and electropolished using the method listed in 3.3.3.

3.5.3 EBSD

Electron backscatter diffraction (EBSD) is a popular technique used to characterise the microstructure of a sample, by attaining diffraction patterns from bulk samples. The technique is performed in scanning electron microscopes (SEM), where flat polished samples are tilted so that angle between the beam direction and the sample surface is typically 70°. The electrons from the electron beam are scattered by atoms in the crystal lattice on the surface of the sample, which produces a pair of diffracted electrons for each of the lattice planes. These diffracted electrons then appear as bands, known as "Kikuchi bands", on the fluorescent phosphor screen of the EBSD detector, with multiple bands making up a diffraction pattern. The diffraction patterns are detected from multiple points in the interaction volume from the electron beam. Each point (also known as pixel) then has the phase and crystal orientation noted, which are then collected by the software to produce a full EBSD map. EDS was also procured when performing EBSD, allowing for EDS maps of the different distribution of elements across an EBSD image.

The EBSD and related EDS work was performed using the JEOL JSM 7900F and the data was processed using AZtecCrystal software. Whilst EBSD samples can be mounted in Bakelite, it was found that thin samples produced and electropolished using the methods listed in 3.3.2 and 3.3.3 provided better results, with much higher hit rates. However, unlike the typical procedure for producing TEM samples, whereby a hole is produced in the thin disc samples, EBSD samples only needed to be polished and therefore could be slightly thicker in addition.

3.5.4 X-ray Diffraction

X-ray diffraction (XRD) is a key analysis technique which measures the x-rays produced by diffraction from a material that is irradiated with a focused beam of x-rays, from a known source and known wavelength. The setup of the machine is known as a goniometer, with a common geometrical setup utilised being the θ-2θ. In this setup, the sample surface is at a set angle of θ while the detector rotates at an angle of 2θ. The sample can also rotate in the plane of its surface, labelled as angle ϕ in Figure 3.7. For randomly orientated polycrystalline samples, this does not affect the diffraction and is not necessary, however, the rotation is beneficial when looking at samples where texture is a concern.

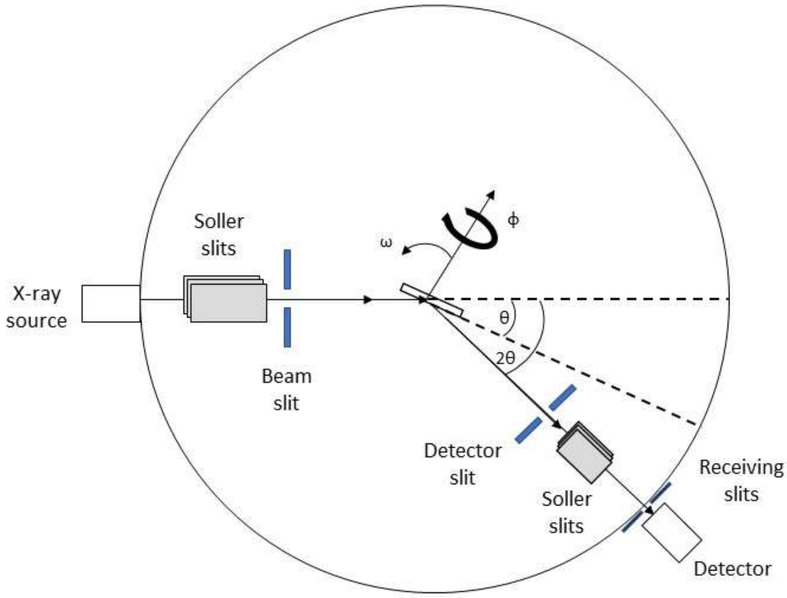

Figure 3.7: XRD schematic

XRD specimens were prepared using the grinding and polishing procedures mentioned in the previous SEM section. However, the final height of the specimens was required to be below 5 mm for the XRD analysis. The XRD was performed using a PANalytical X'pert^3 diffractometer with Cu K-α x-ray source (1.544 Å).

The volume fraction of retained austenite for each sample and condition, was calculated using the reference intensity ratio method (RIR method). The method utilises Equation 3.1 shown below.

$$\frac{\left(\frac{I}{I_c}\right)_a}{\left(\frac{I}{I_c}\right)_b} = \frac{X_a}{X_b} \tag{3.1}$$

I/I_c is the intensity of a phase divided by the intensity of corundum in a 50-50 mixture, and X is the fraction of a phase. With known values I/I_c within PDF-4+, the volume fraction of a phase can be calculated using this method. Whilst typically in research, Rietveld analysis is used for quantitative phase analysis of retained austenite in steels, large amounts of fluorescence in the XRD patterns caused a lot of difficulties in utilising the technique.

3.5.5 Vickers Hardness Testing

Samples were etched using Nital to prepare for hardness testing, allowing for easy identification of the indent shapes and sizes. The hardness testing was performed using a Vickers hardness testing machine, with a force of 1kgf and a dwell time of 18 seconds. The square pyramid shaped tip had an angle (α) of 136° between faces and was made of diamond. The Vickers hardness was calculated by taking the 2 diagonal lengths (in μm) of the indent and calculating the mean length. The Vickers hardness number can then be calculated using Equation 3.2:

$$HV = \frac{2000Psin(\frac{\alpha}{2})}{d^2} = \frac{2000(0.927)P}{d^2} = \frac{1854.4P}{d^2} \tag{3.2}$$

Where HV is the Vickers hardness value, P is the applied load in gf, d is the mean diagonal length and (α) the angle between the faces. A template of calculated HV values for a set load and horizontal and vertical diagonal lengths was utilised to speed up calculations.

To ensure a statistically meaningful result, 10 indents were made and measured per heat treated sample. To reduce the influence of previous indentations, the indents were spaced at least 2 diagonal lengths of the indents apart.

4.0 Q&P Work

4.1 Introduction

Quench and partitioned (Q&P) steels were chosen as the initial alternative steel microstructure to investigate. Q&P steels have a dual phase microstructure consisting of martensite and retained austenite. The microstructure was suggested as an alternative by British Steel, due to the high work hardening rate of the retained austenite when compared with ferrite. Additionally, the R&D team at British Steel had previous experience with Q&P rod and some rods with compositions designed for Q&P treatment remained from past experiments. This saved a large amount of time while a process route to produce new steel ingots was developed. The aim was to investigate the rod microstructures after utilising a Q&P heat treatment. The objectives were:

- To observe the microstructure present after the heat treatment, to confirm the processing route utilised was sufficient to produce a Q&P microstructure, containing martensite and retained austenite.
- To gain mechanical data from the heat treated steels, to assess the suitability of the alternative steel microstructure for high strength steel wire and rod.

The past work on Q&P steel rod was studied by Lifen Deng, Peter F Morris and the industrial supervisor of the EngD project, Shaun Hobson [70]. The Q&P steel rods that remained from the previous study, were processed using the same heat treatment schedule developed by L.Deng in 2013. This was to compare the results to those achieved in Deng's work, and act as a starting point while a process to develop custom steel alloy ingots for future work. Deng's work was based on optimising a Q&P heat treatment for steel rod, testing multiple steel alloy compositions, as well as quench and partition temperatures. Deng created 5 different compositions in total. Whilst Deng had the best combination of drawability and strength results from rods 9JF12, however, only 9JF10 and 9JF13 rods were still available from the experiments and thus were utilised in this project. The compositions of the two remaining steel alloy rods are listed in Table 3.1 in Section 3.1.1. The martensitic transformation start and finish temperatures of each of the different steel rod compositions (M_s and M_f respectively) were measured by Deng using dilatometry. Each of the samples were austenised at 950 °C and a cooling rate of 150 °Cs^{-1} was used. The temperature of the rods throughout the experiments were measured using a thermocouple inserted into the centre of one end of the rod specimen.

Two of the remaining rods, referred to Sample 1 and 2, had the alloy composition of 9JF10. Three rods remained that had the alloy compositions of 9JF13, which became Sample 3, 4 and 5. Table 5.1 relates the industrial alloy composition with each numbered sample and the corresponding heat treatments.

Table 5.1: Heat treatment schedule for samples 1-5.

Rod Steel Alloy	Rod Sample No.	Austenisation Temperature/ °C	Quenching Temperature/ °C	Tempering Temperature/ °C	Holding Time
9JF10	Sample 1	950	200	525	10 s
	Sample 2	950	200	525	30 s
9JF13	Sample 3	950	200	300	1 min
	Sample 4	950	200	300	5 min
	Sample 5	950	200	300	10 min

Each of the rods were 11mm in diameter but of varying lengths. In Deng's original work, the 9JF10 rods were all quenched in a salt bath to 220 °C and partitioned in another high temperature salt bath at 400 °C, whilst the 9JF13 rods were quenched to 200 °C and partitioned at 500 °C. However, the remaining rods heat treatments had to be modified from Deng's original plan for several reasons. The first reason was the number of available salt baths. Deng's experiments were done at a time when British Steel had their own salt baths available at the Swindon Technology Centre (STC) site in Rotherham. This meant there were multiple baths that could be set to a variety of specific temperatures beforehand. However, the STC closed shortly before the start of the project. Unfortunately, the same heat treatment options were not available using the salt baths at Summit Glow Ltd. Due to the hazards involved with certain molten salts, the facilities did not have any way to perform salt bath heat treatments at 400 °C. Therefore, rod Sample 1 and 2 were to be tempered at 525 °C as that was the only high temperature salt bath available. It was decided that the heat treatment for rod sample 3, 4 and 5's should follow the 9JF12 rods to aim to obtain a carbide free martensitic/bainitic microstructure containing retained austenite. The rods in the original study were to be quenched at 200 °C and then partitioned at 300 °C, however, there was only one available salt bath that could operate at both relatively low temperatures. With the large amount of time taken to decrease the temperatures within the salt baths, it was instead decided to air temper the rods in an air-tempering furnace to obtain the microstructures.

A thermocouple reading was taken for the heat treatment carried out on rod 5, with the thermocouple being placed in an axial hole drilled into the end of the rod. Rod 5 was chosen out of the air-tempered rods to be measured due to having the longest holding time. Therefore, it is assumed the other temperature-time plots could be predicted using the data. Data was also to be recorded for the pure salt bath heat treatments (rod samples 1 and 2), however the risk of the equipment and user getting damaged by molten salt spills during transfers was deemed too great.

Additional work was done to investigate the microstructures of the rod alloys prior to tempering. These rod specimens were given the same austenisation step as the previous experiments before being quenched down to 200 °C in a molten salt bath and held for a few seconds, before finally being quenched in water to room temperature. These additional experiments were done to gain a better idea on the development of the microstructure throughout the Q&P process. The Q&P rods were additionally planned to be cold drawn, as was one of the objectives, to gain more information on the mechanical properties and directly compare the properties to that of cold drawn pearlite. However, issues with British Steel's drawing bench and access to the facility (through the COVID pandemic) meant that this was not achieved.

4.2 Results

4.2.1 Heat Treatment

Figure 4.1 shows a schematic diagram of the different heat treatment temperatures and times utilised for each of the rods. The samples were held at the austenisation temperature for 5 minutes, whilst the tempering step was varied between samples. The austenisation step was performed using molten salt bath, while the tempered step varied as mentioned earlier between utilising another salt bath or in air in a furnace. Figure 4.2 below displays the temperature readings recorded during the salt bath heat treatment for rod 5. The thermal data readings were logged every 50 ms.

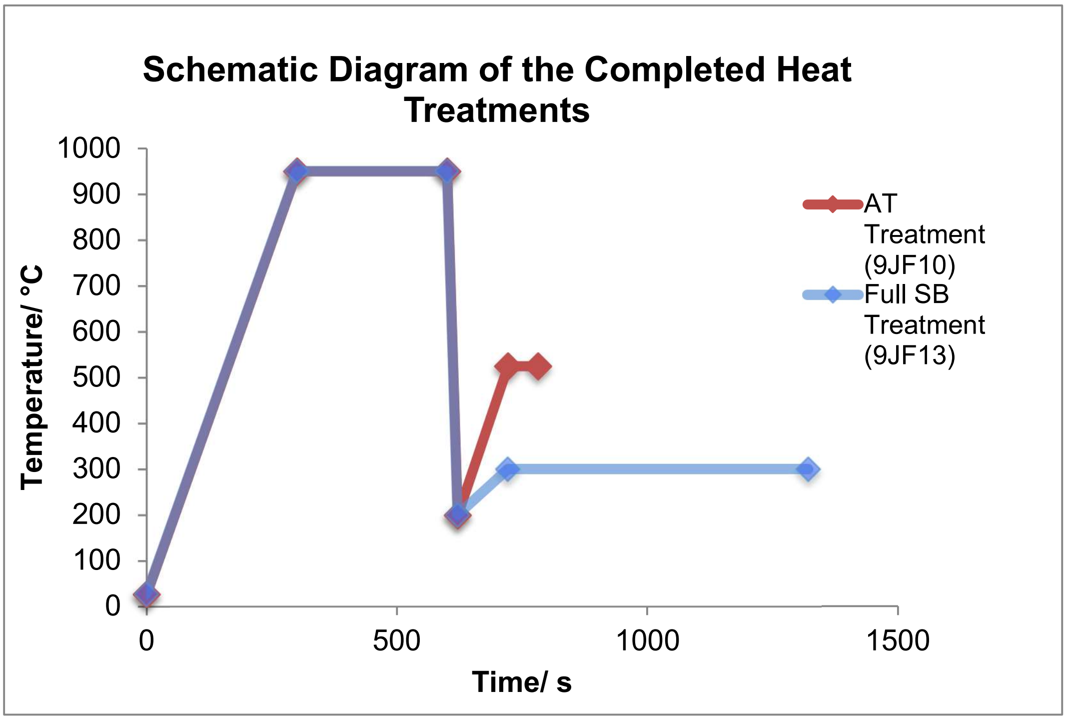

Figure 4.1: Schematic diagram of the Q&P heat treatments applied to the rod samples. AT and SB stand for air tempered heat treatment and salt bath heat treatment respectively. Sample 1 and 2 followed the AT heat treatment route, while Samples 3, 4 and 5 followed the SB heat treatment route.

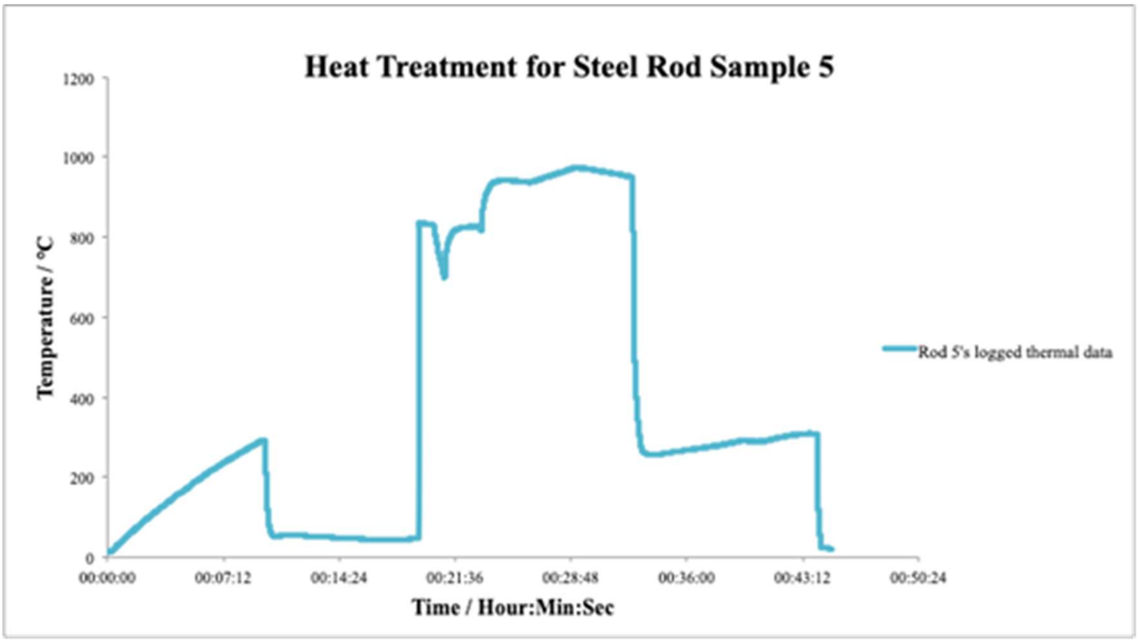

Figure 4.2: Data logged during the Q&P heat treatment for rod sample 5 using the molten salt baths. The loss of data in areas is due to salt contaminating the measuring equipment.

The average cooling rate during the quench from 950 °C to 200 °C is estimated to be 12 $°Cs^{-1}$. It should be noted that the sudden drop in temperature logs around the 10-minute time mark was caused by a molten salt spillage onto the data logger. Thankfully the issue was resolved relatively quickly between the 8 to 18 minute mark, while the rod specimen underwent the austenisation step.

4.2.2 SEM Images

Figures 4.3 through 4.7 show the SEM micrographs of the rod samples after the heat treatments. The images were taken using the FEI Inspect F50, with the experimental technique described in Section 3. The microstructures are predominantly composed of the lath martensite (α') and blocky regions of retained austenite (γ).

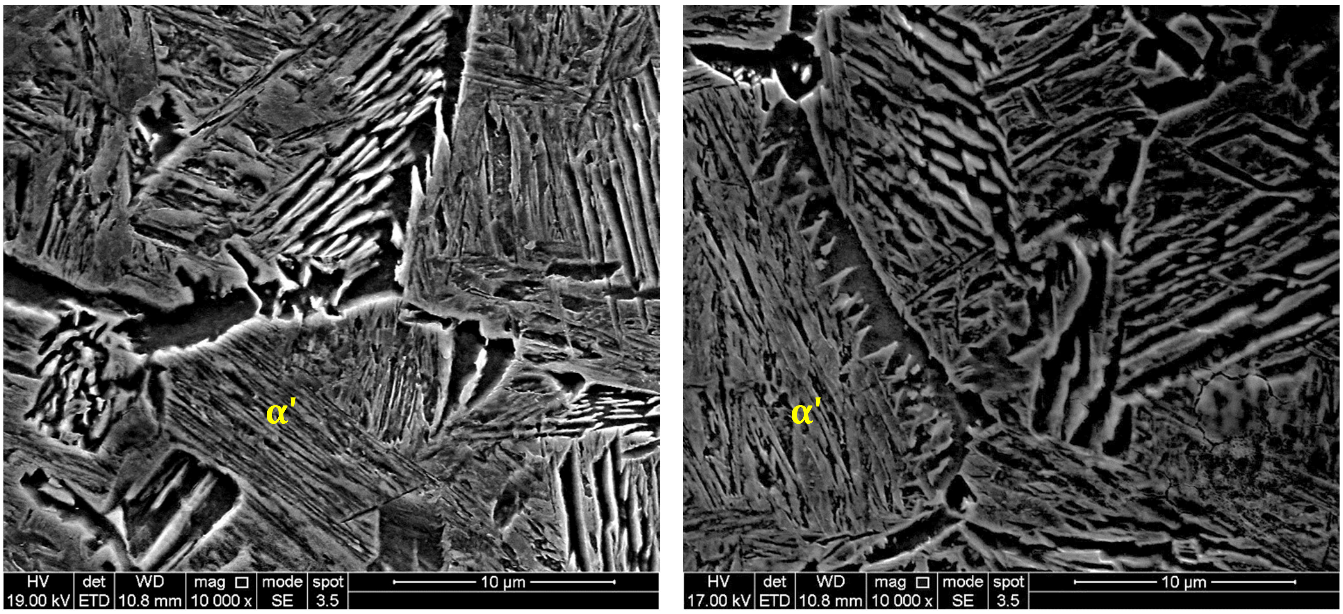

Figure 4.3: SE-SEM micrographs showing the martensitic microstructure of Sample 1, obtained after heat treatment. Sample 1 had the composition of alloy 9JF10 and was partitioned in air at 525 °C for 10s.

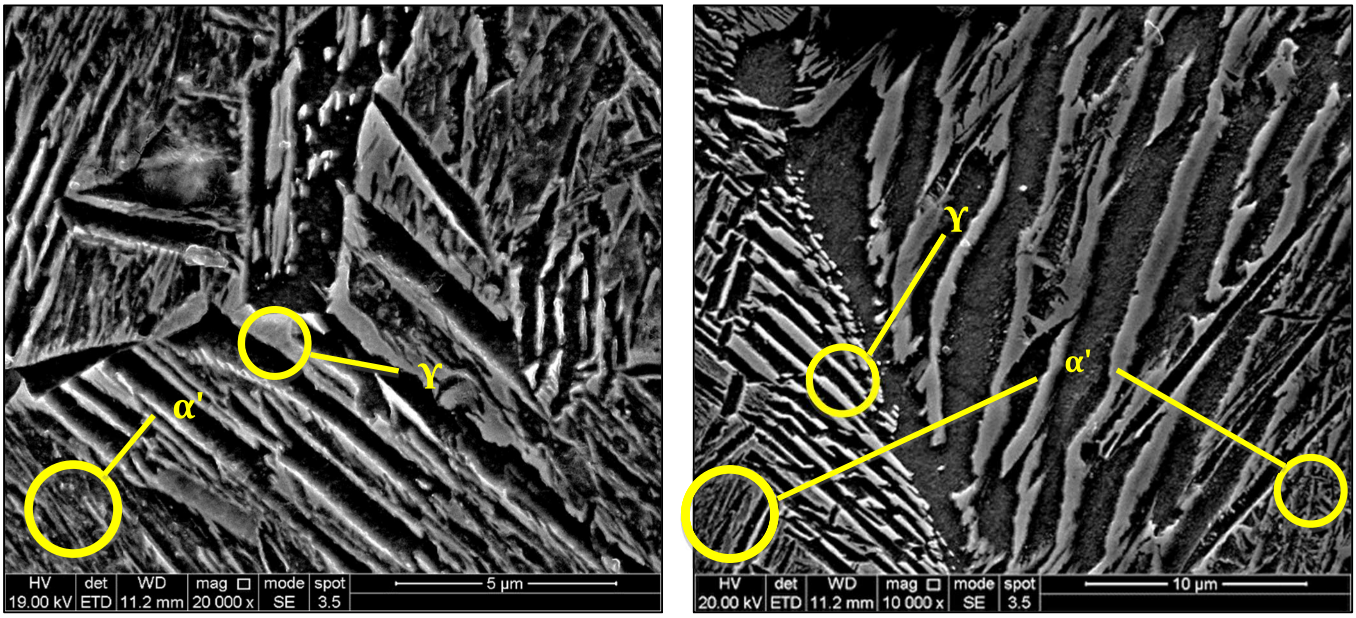

Figure 4.4: SE-SEM micrographs showing the martensitic microstructure of Sample 2, obtained after heat treatment. Sample 2 had the composition of alloy 9JF10 and was partitioned in air at 525 °C for 30s.

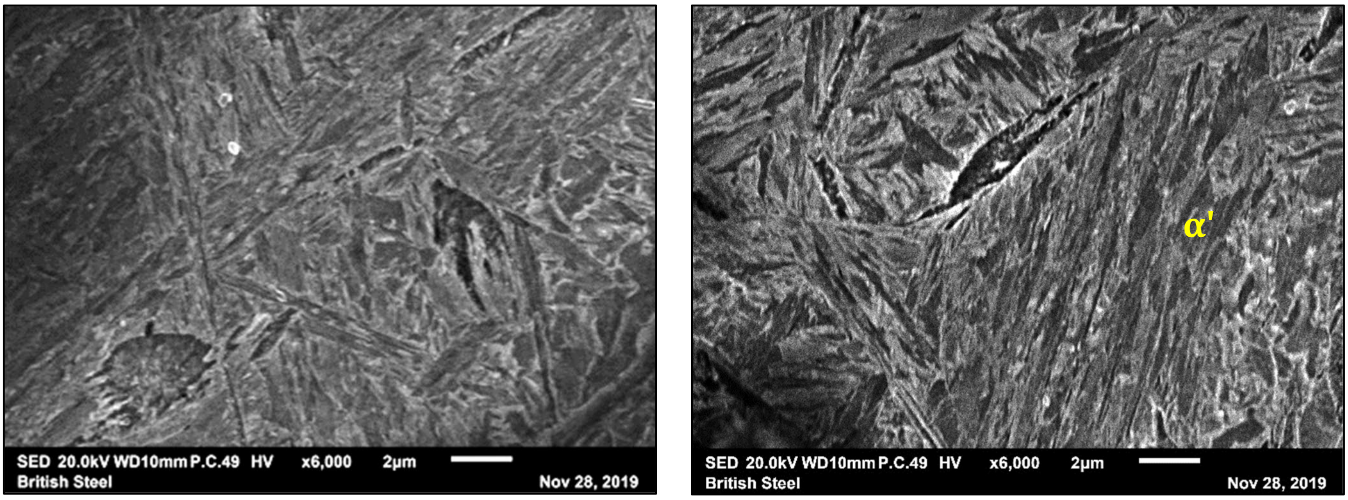

Figure 4.5: SE-SEM micrographs showing the martensitic microstructure of Sample 3, obtained after heat treatment. Sample 3 had the composition of alloy 9JF13 and was partition treated at 300 °C for 1 minute, using a molten salt bath.

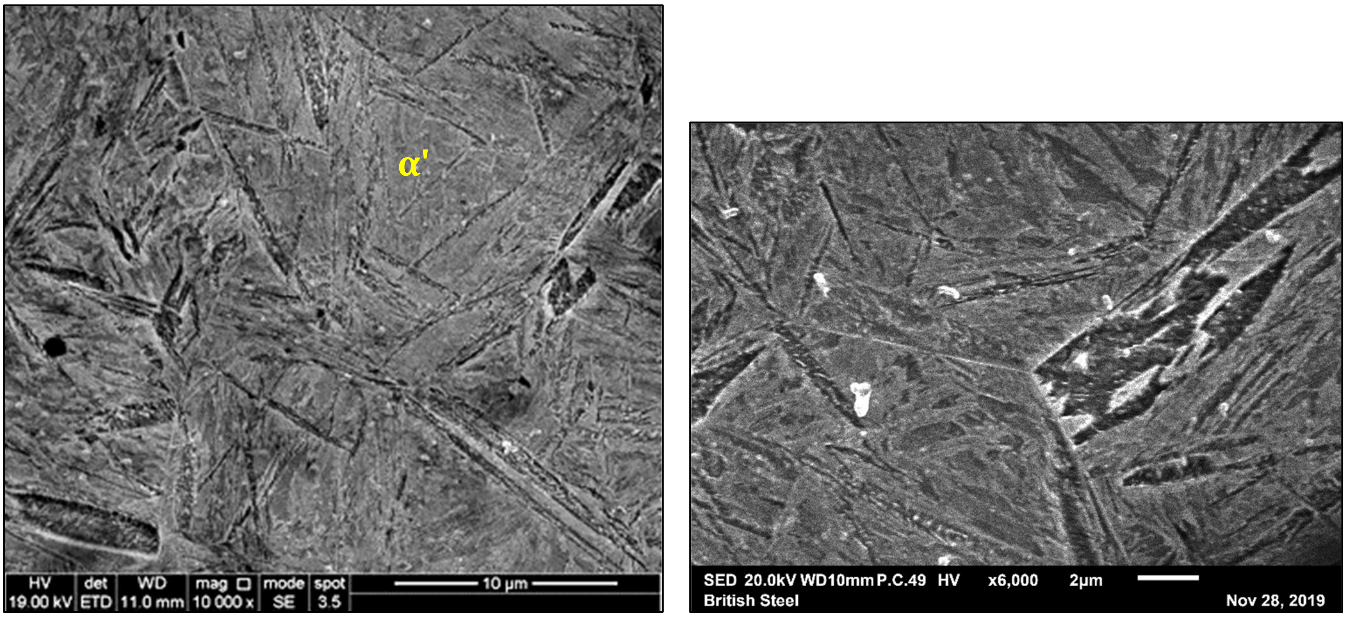

Figure 4.6: SE-SEM micrographs showing the martensitic microstructure of Sample 4, obtained after heat treatment. Sample 4 had the composition of alloy 9JF13 and was partition treated at 300 °C for 5 minutes, using a molten salt bath.

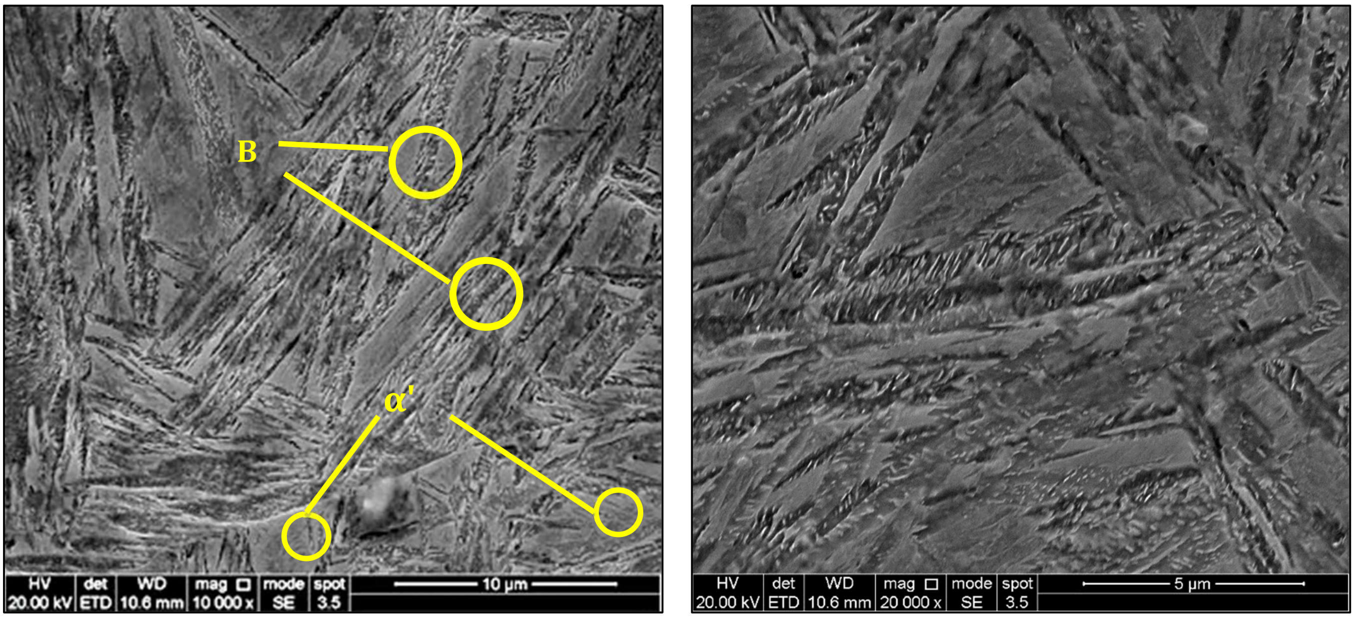

Figure 4.7: SE-SEM micrographs showing the martensitic microstructure of Sample 6, obtained after heat treatment. Sample 6 had the composition of alloy 9JF13 and was partition treated at 300 °C for 10 minutes, using a molten salt bath. The regions marked as B are believed to be bainitic in nature or potentially carbides.

Figure 4.8 shows the microstructures of the two alloy compositions after being quenched in water, after the initial quenching step down from 950 °C to 200 °C.

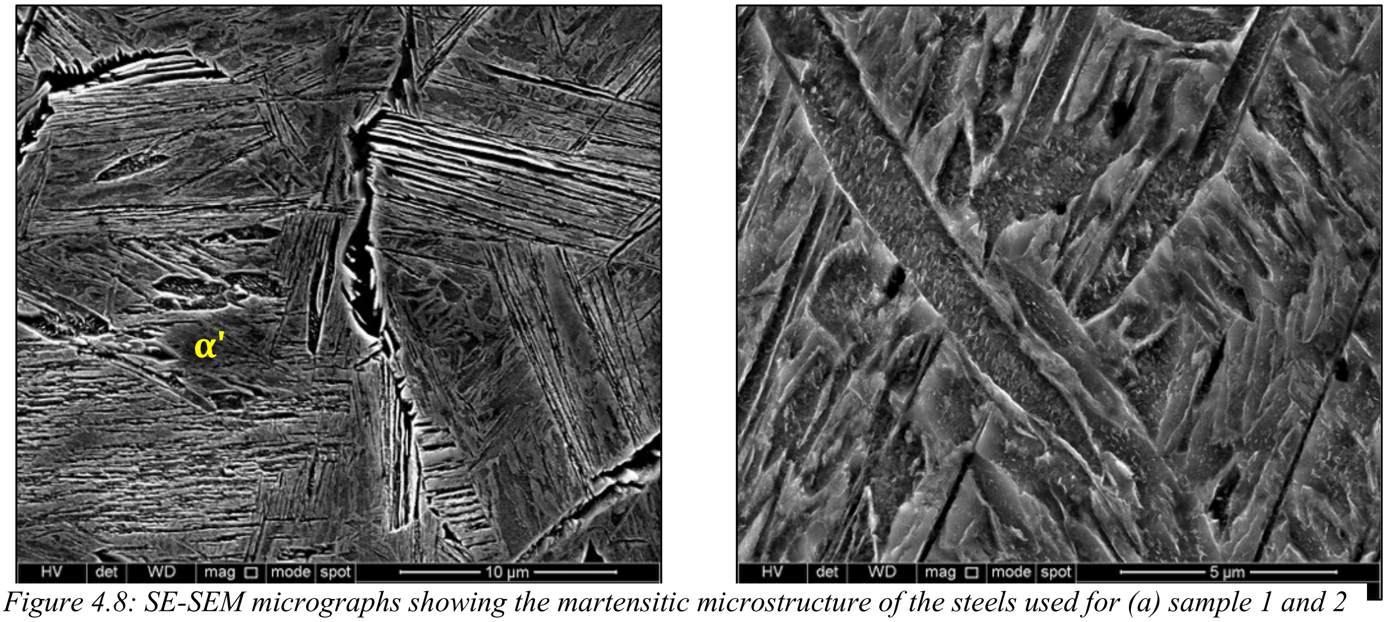

Figure 4.8: SE-SEM micrographs showing the martensitic microstructure of the steels used for (a) sample 1 and 2 & (b) samples 3, 4 of the samples that were water quenched after the initial quench from 950 °C to 200 °C.

4.2.3 Vickers Hardness Testing

The mean Vickers hardness testing values obtained for each of the samples are plotted in Figure 4.9, with standard deviation error bars added for each set of results. As previously mentioned in Section 3, a force of 1kgf was utilised for all the samples and the mean value was calculated from 10 different values taken on the surface of the mounted samples.

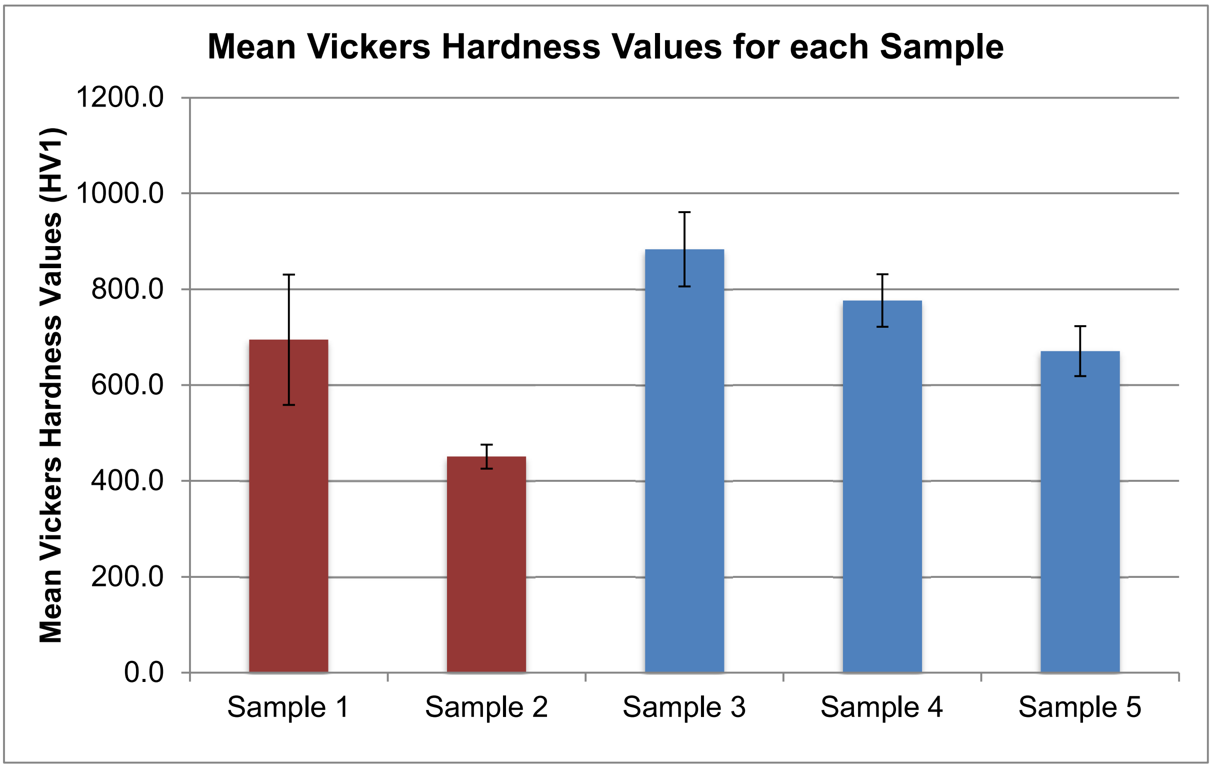

Figure 4.9: The calculated mean hardness values for the heat-treated samples, with standard deviation error bar. The bars in red represent the samples from the alloy composition 9FJ10, while the bars in blue represent the samples from the alloy composition 9FJ13.

4.3 Discussion

It appears that the formation of carbides was more suppressed in rod samples 1 and 2 than in samples 3, 4 and 5. This can be observed more clearly when comparing the SEM images from rod samples 2 and 5, as shown below in Figure 4.10. Samples 4 and 5 appear to have microstructures consisting of martensite and lower bainite, whilst samples 1 and 2 appear to have finer predominantly martensitic structures. It is difficult to distinguish whether either sample 1 or 2 are carbide free structures (particularly with sample 2's SEM images), however comparatively the structures contain less carbides if any to samples 3, 4 and 5.

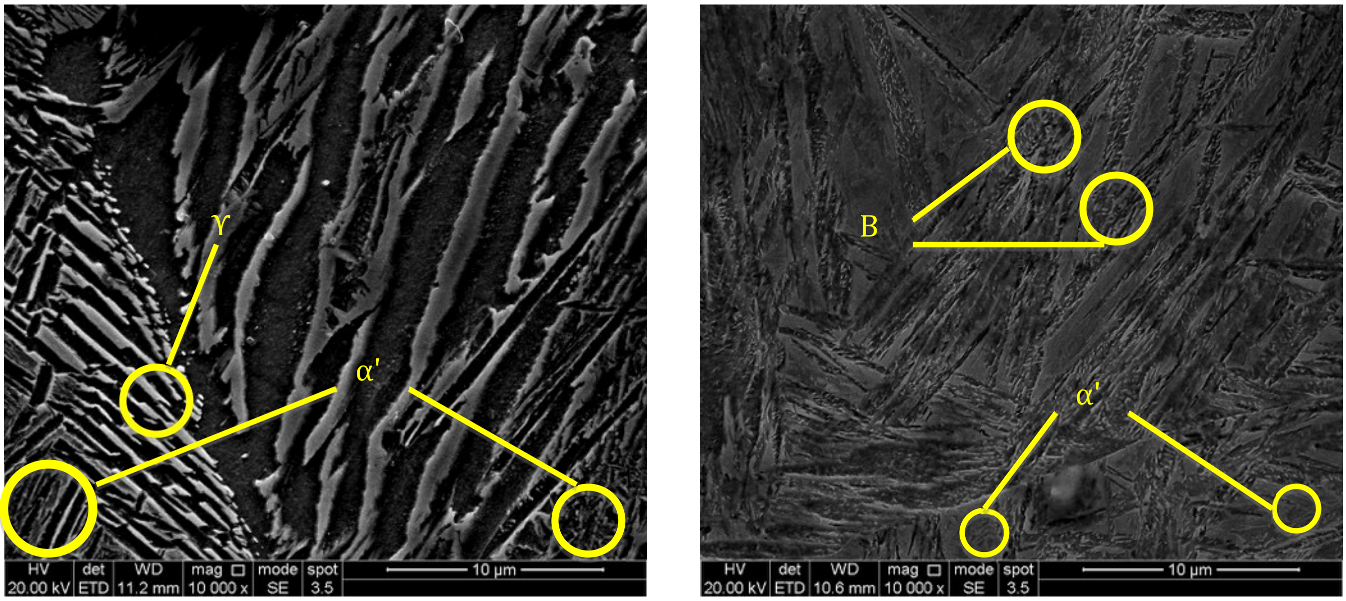

Figure 4.10: SE-SEM image from sample 2 (left) and sample 5 (right) after heat treatment.

The most likely explanation for the greater formation of carbides in samples 3, 4 and 5 is due to the lower Si wt.% in the steel alloy utilised. Rod alloy 9JF10 (from which sample 1 and 2 were composed of) has 1.96 Si wt.% compared to the 0.97 Si wt.% amount present in rod alloy 9JF13 (the steel alloy used for rod samples 3, 4 and 5). Si is known for its ability to suppress the formation of carbides for both bainitic and Q&P carbide free steel microstructures [33], [67]. As discussed earlier, suppressing the formation of carbides during the Q&P process is crucial, as it results in a condition known as constrained paraequilibrium (CPE) [57]. This metastable condition allows for the movement of carbon atoms from the martensite to the retained austenite regions, stabilising the retained austenite in addition to tempering the martensite. The formation of carbides not only has a detrimental effect due to the mechanical properties, but also, results in less stabilised austenite forming fresh martensite upon the final quench to room temperature.

The Vickers hardness results for the samples shows that samples 1 and 2 appear to have tempered more than samples 3, 4 and 5 as shown by the decrease in hardness. This is likely due to samples 1 and 2 being partitioned at a temperature of 500 °C compared to the 300 °C used for 3, 4 and 5, resulting in a much higher tempering effect. This also resulted in coarser martensite and polygonal retained austenite in the sample, suggesting a lower partitioning temperature should still be utilised for a finer microstructure. However, the contrast in tempering could also be due to the difference in alloy compositions of the two parent rod steels.

The formation of bainite in quenched sample 2 appears to be from either an insufficient quench rate or an excessive hold time for quenching. The quench from 950 °C to 200 °C has a cooling rate estimated to be around 12 $°Cs^{-1}$. This is lower than the quenching rate used in Lifen Deng's past work, where a quench rate of 37 $° Cs^{-1}$ was reached. Therefore, the bainite present in samples 3, 4 and 5 SEM micrographs may have formed during quenching. The microstructures of the two quenched samples appear to have been inadequately quenched, as both samples' microstructures appear to contain bainite and carbides to some degree. This could be due to several factors such as the molten salt baths being set to an incorrect temperature or due to human error mixing up the rods. This could explain why quenched sample 1 from rod 9JF10 formed bainite, considering the results of the Q&P heat treatments and the SEM micrographs of rod samples 1 and 2. However, without further analysis of quenched sample 1, that is difficult to confirm.

It should be noted that due to the irregularities of the quenched sample results, further work would have been completed to amend these results if not for the COVID-19 isolation period that took into effect. This is also true for the lack of TEM, XRD and mechanical results, which were unable to be added to this study, which would have further aided in identifying the phases present in the end rod microstructures.

4.4 Conclusions

In summary, these results demonstrate that it is essential to have a large addition of silicon in the compositions for steel alloys to be utilised in the Q&P process. The silicon is required to suppress the formation of carbides and allow for the constant paraequilbrium condition to be reached. With insufficient silicon, course carbides and untempered martensite are present in the microstructure and will lead to large difficulties in further drawing the rod.

As expected, the hardness of the heat treated rod samples decreased with increasing tempering time, as more time is given for carbon to partition into the austenite. This effect is even larger at higher hold temperatures (>400 °C), whilst tempering at temperatures just above M_S takes much longer for the specimens to reach an equivalent level of tempering. This is caused by the higher temperatures increasing the kinetics involved, allowing for the carbon in the martensite to diffuse out at a higher rate. Rod samples 1 and 2 had a higher degree of tempering due to the higher temperatures utilised. This results in microstructures closer to the aim microstructure of tempered martensite. For future work, it is recommended that heat treatments on Q&P rods are carried out at a partitioning temperature just above M_S. This is an attempt to keep the martensite fine, to allow for as much partitioning between the martensite and retained austenite as possible by shortening the diffusion distance for the carbon atoms.

Furthermore, this research has demonstrated that the molten salt bath quench does not reach adequate cooling rates for the Q&P process. The formation of bainite is an indicator that the quench rates were insufficient. In addition, the measured quench rate was lower than the quench rate used by Lifen Deng in the past work performed by British Steel. It is important to achieve an adequate quench rate to avoid the nose of the TTT diagram and in turn the formation of bainite.

5.0 Carbide Free Bainite Work 1

5.1 Introduction

The project was originally designed to examine both quench and partitioned and nanostructured bainitic steels. However, the scope was changed after the realisation that the quenching step into a higher temperature holding step was unachievable with the available molten salt bath facilities and the TMC within university. Furthermore, focussing on one heat treatment route and microstructure streamlined sample production and allowed for more analysis between the results. Therefore, the VIM cast steel ingot was to be heat treated with the aim to produce a carbide free bainitic microstructure, akin to the super-bainitic microstructures achieved by Bhadeshia [33], [71], Garcia-Mateo [43], [46], [72] and others[26], [49], [51], [72]. Figure 5.1 shows a SEM image the aim microstructure from Garcia-Mateo et al [72].

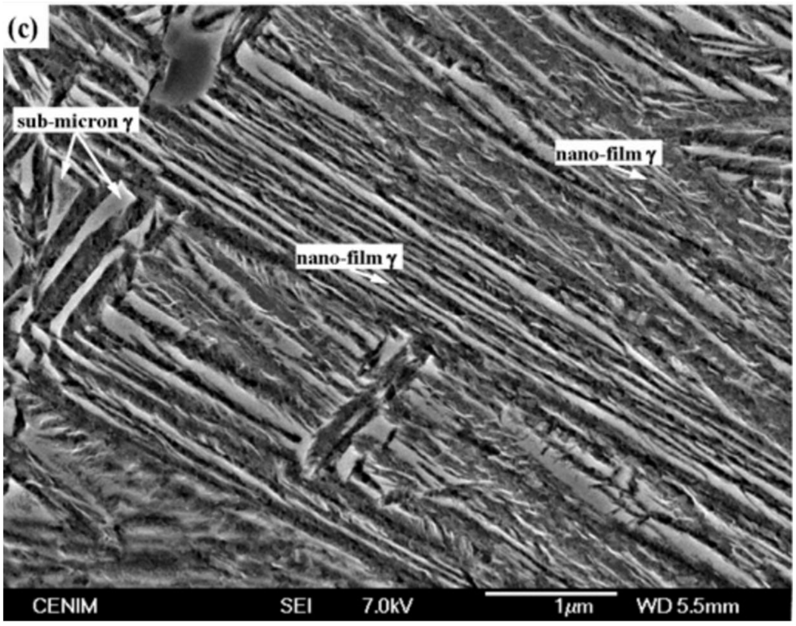

Figure 5.1: Example of the nanostructured bainite microstructure, obtained by isothermally holding at 250 °C for 16 hours [72].

Whilst lower bainite provides higher work hardening rates in drawn steel wire than a conventional pearlitic microstructure, there are two main drawbacks with this alternative for steel rod and wire use. One is that retained austenite in the steel undergoes a transformation induced plasticity (TRIP) reaction whereby the retained austenite is transformed into martensite. This dramatically decreases the ductility and drawability of the wire, causing brittle failures. In addition, the untempered martensite formed by the TRIP reaction results in inferior torsional ductility in wire, when compared to pearlitic grades [55]. The other issue is the relatively long transformation times to produce nano-bainite with little to no carbide precipitation. These transformation times can be more than two days. Therefore, there are two main aims for the following work:

- To create a carbide free nanostructured bainitic microstructure containing minimal retained austenite, preferably with a needle-like morphology
- To investigate the stability of retained austenite under deformation/wire drawing.

The steel ingot was produced with an aim alloy composition of 0.40 wt.% C - 2.00 wt.% Si – 2.00 wt.% Mn – 1.00 wt.% Cr. The composition of the alloy was chosen to continue to investigate a past bainitic grade steel produced during British Steel's preliminary work [55]. Typically, carbide free bainitic grades have a carbon composition ranging from 0.6 to 1.0 wt.% [37]. The relatively low carbon composition utilised compared to other work on nanostructured bainites is due to British Steel's own research in the area. It was found that high carbon grades (around 0.7 to 1.0 wt.% C) could not reach adequate elongation and ductility levels for wire drawing. Therefore 0.3 to 0.4 wt.% C was recommended, as any lower carbon wt.% would result in rod with an inferior UTS to a pearlitic grade. The silicon addition suppresses carbide precipitation and encourages carbon partitioning to stabilise any retained austenite present. The silicon addition was set as high as possible before the formation of delta ferrite becomes a problem. The Mn and Cr additions' main role was to lower the M_s temperature to approximately 300 °C, as past research by the company suggested this would result in a fine bainite with needle-like retained austenite as opposed to large polygonal blocks of retained austenite. However, it should be noted that manganese additionally increases the transformation times to form fully bainitic structures.

To refine the cast ingot microstructure, the ingot was first hot rolled before being machined to produce axial symmetric samples, as described in Section 3. Each of the sample heat treatments began with an austenisation step by holding the sample for 5 minutes at 950 °C, to produce a fine prior austenite grain size (PAG). The samples were then quenched down to different isothermal holding temperatures, using forced air cooling. One additional sample (sample 0) was fully quenched to room temperature to investigate the PAG size in future work. Table 5.1 and Figure 5.2 show the schematic heat treatment for the samples.

Table 5.1: The 3 sample sets and associated isothermal holding temperatures.

Sample ID	Austenisation Holding Temp. (°C)	Isothermal Holding Temp. (°C)	Holding time (hours)
Sample 1	950	300	6
Sample 2	950	325	6
Sample 3	950	350	6

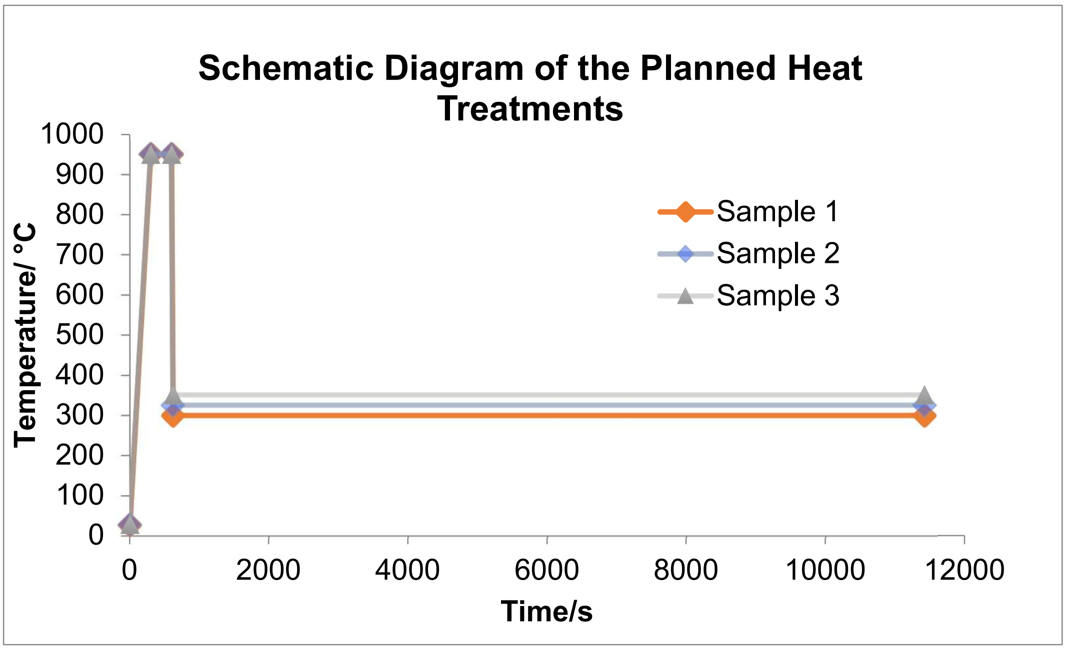

Figure 5.2: Schematic diagram of the heat treatments performed by using the TMC.

The temperatures chosen were to investigate the effect of the isothermal holding temperature on the retained austenite volume fraction and stability. The long low temperature isothermal hold was utilised to promote the formation of bainite without producing pearlite. The heat treatments were carried out using the thermomechanical compression machine (TMC). The microstructures of the samples were analysed using optical microscopy and scanning electron microscopy (SEM), while stress-strain curves for the samples were collected using compression testing with the TMC.

5.2 Results

5.2.1 Alloy Composition

The composition of the VIM cast ingot was analysed to show that the alloy weight additions were identical or similar to the aim alloy composition. The aim composition for the cast ingot is shown in Table 5.2. The composition was investigated using optical emission spectroscopy (OES) by British Steel, as shown in Table 5.3.

Table 5.2: The aim chemical composition for the VIM produced ingot.

	Alloy Additions (wt.%)			
	C	**Si**	**Mn**	**Cr**
Aim Steel Ingot Composition	0.4	2.0	2.0	1.0

Table 5.3: Chemical composition analysis taken at different points in the ingot samples using OES.

	Alloy Additions (wt.%)						
	C	**Si**	**Mn**	**P**	**S**	**Cr**	**N**
Test sample 1	0.41	1.94	1.71	0.004	<0.001	1.00	0.0014
Test sample 2	0.39	1.96	1.71	0.003	<0.001	1.00	0.0019

5.2.2 Heat Treatments

To ensure the heat treatments were performed at the designated temperatures, heating/cooling rates and times, the temperature was recorded through thermocouples in the samples during the TMC heat treatment. Figure 5.3 shows the thermocouple readings recorded for each of the heat-treated samples. The heating rate for the samples to reach the austenisation temperature was 9.77 °Cs^{-1}. The cooling rate to quench down to the isothermal holding temperature from the austenisation temperature was 17.97 °Cs^{-1} respectively. The heating feedback system of the TMC's FTTU has a small latency, therefore there is a marginal amount of overheating and undercooling as seen in Figure 5.3 for the austenisation step and right after the quench to the isothermal holding step.

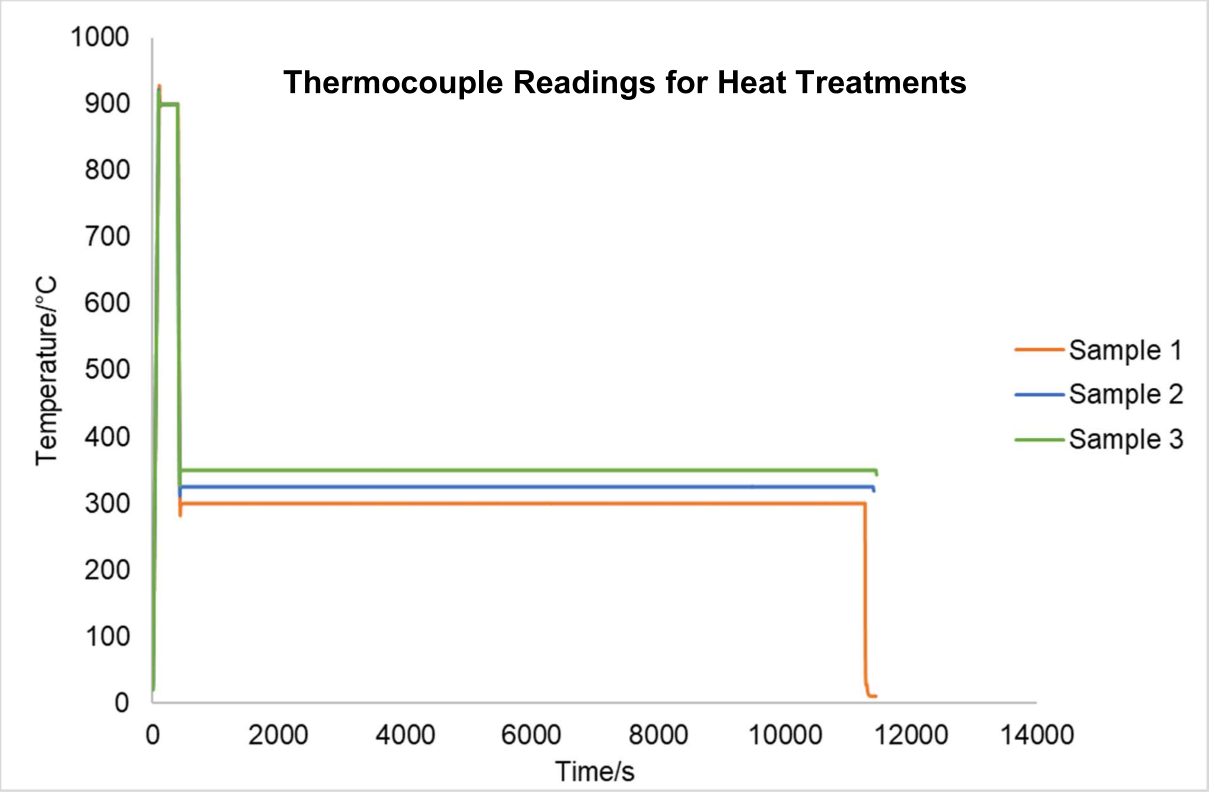

Figure 5.3: Thermocouple data obtained during the TMC heat treatments for Sample 1, 2 and 3.

5.2.3 Optical Microscopy Images

Optical microscopy images were taken of the different samples, polished and etched using the methods laid out in Section 3. Figure 5.4 (a), (b) and Figure 5.5 show the optical micrographs taken for sample 1, 2 and 3 respectively. Each of the images were taken at magnification of 20 and after etching in 2 vol% Nital. The isothermal holding temperature is displayed in the top left corner of each image. The microstructures contain fine laths, indicative of martensite or bainite. Pitting is present in some of the micrographs, brought on the micropreperation of the samples.

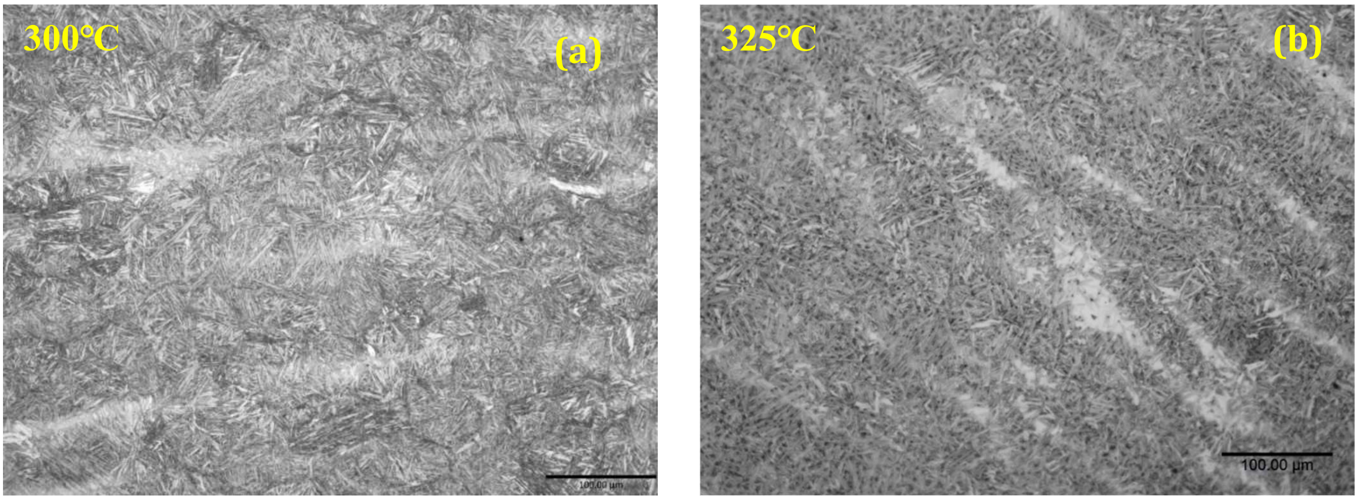

Figure 5.4: Optical micrographs of the microstructures obtained after the isothermal heat treatment, for (a) Sample 1 and (b) Sample 2.

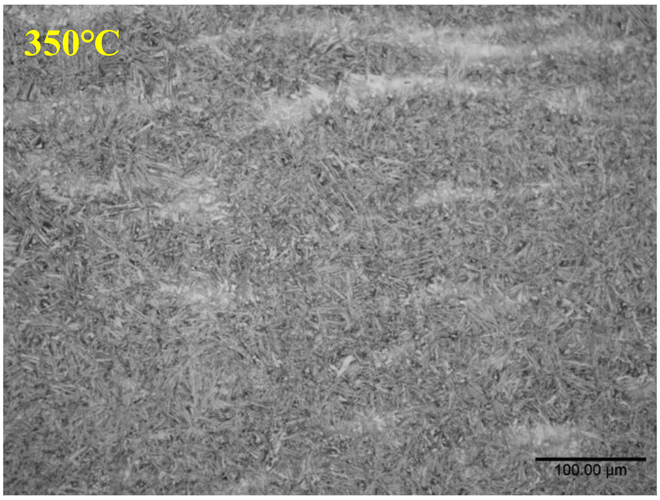

Figure 5.5: Optical micrograph of microstructure obtained after the isothermal heat treatment for Sample 3.

5.2.4 SEM Images

SEM of the etched sample surfaces was carried out using the equipment and method listed in Section 3. Figure 5.6, Figure 5.7 and Figure 5.8 shows the SE-SEM images taken for sample 1, 2 and 3. The (left) and (right) SE-SEM images were taken at a magnification of 10,000 and 20,000 respectively. The microstructures consist of nanostructured bainite and retained austenite, in both blocky and thin film morphology.

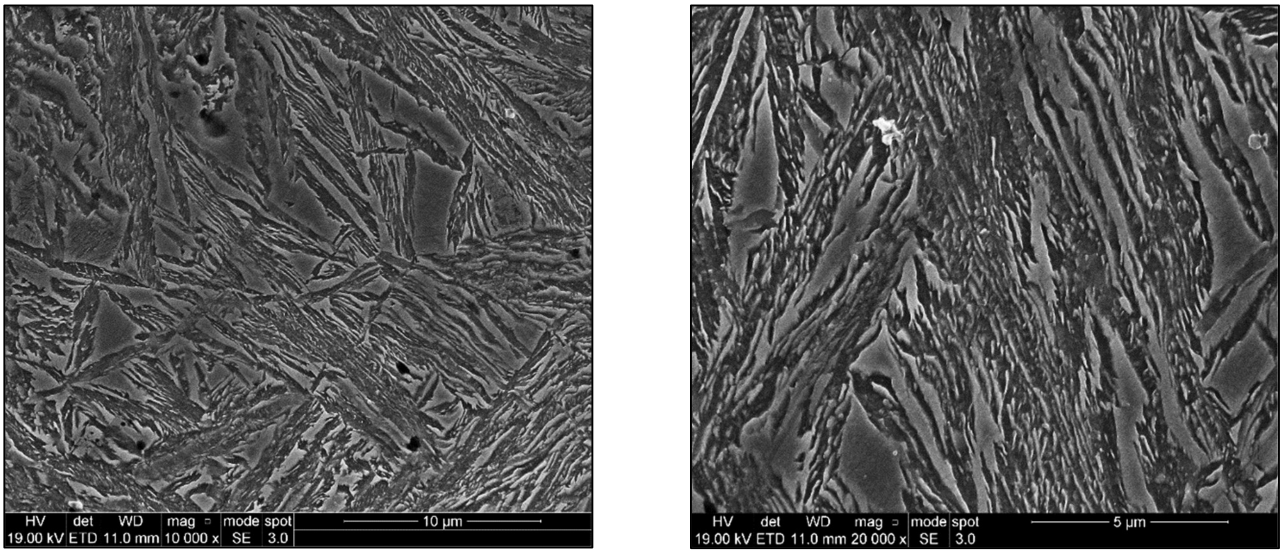

Figure 5.6: SE-SEM micrographs obtained from Sample 1 after heat treatment, isothermally held at 300 °C for 6 hours.

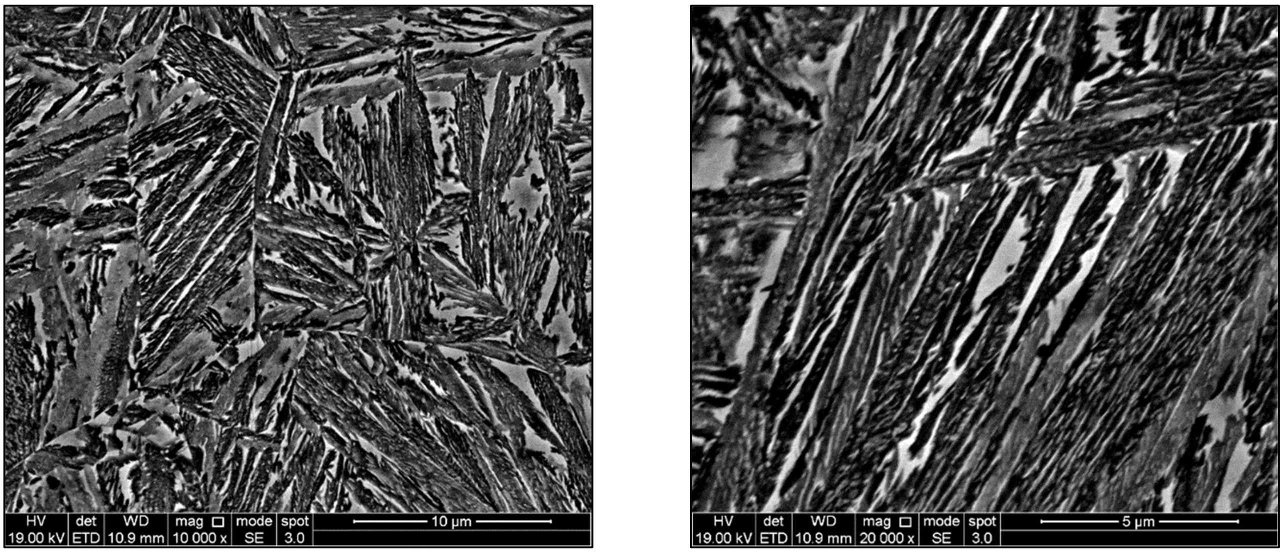

Figure 5.7: SE-SEM micrographs obtained from Sample 2 after heat treatment, isothermally held at 325 °C for 6 hours.

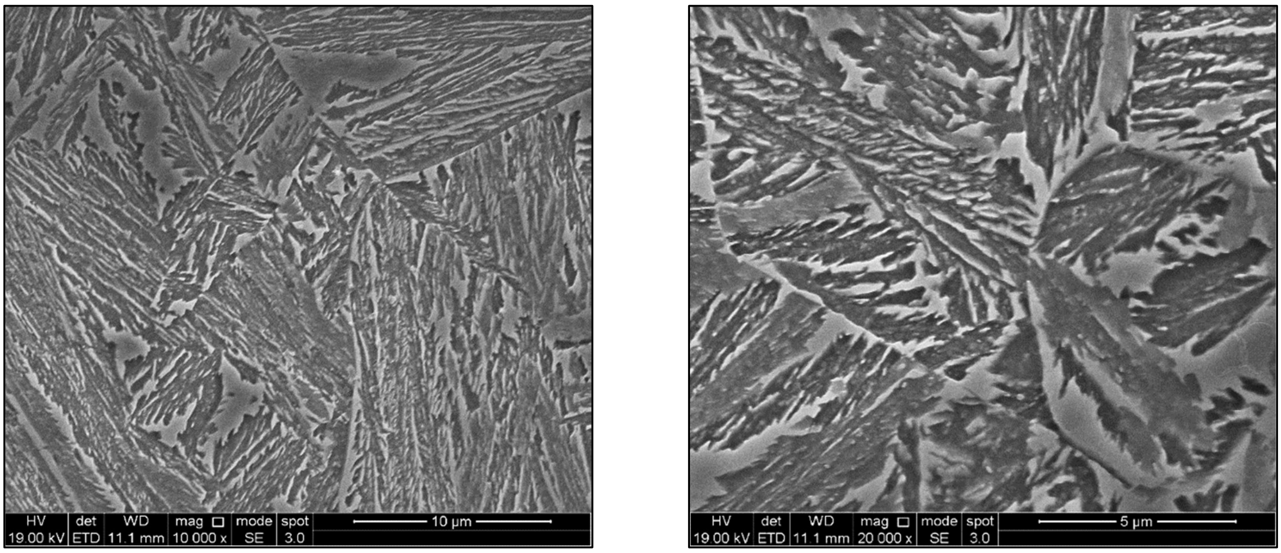

Figure 5.8: SE-SEM micrographs obtained from Sample 3 after heat treatment, isothermally held at 350 °C for 6 hours.

5.2.5 Compression Testing

Stress-strain curves from compression testing results could only be acquired for Sample 2, isothermally held at 325 °C. Sample 1 and Sample 3 had brittle failures for each test before reaching the aim strain of 0.5, resulting in data reading issues. Figures 5.9 and 5.10 show two examples of the failed compression test results for Sample 1 and 3 respectively.

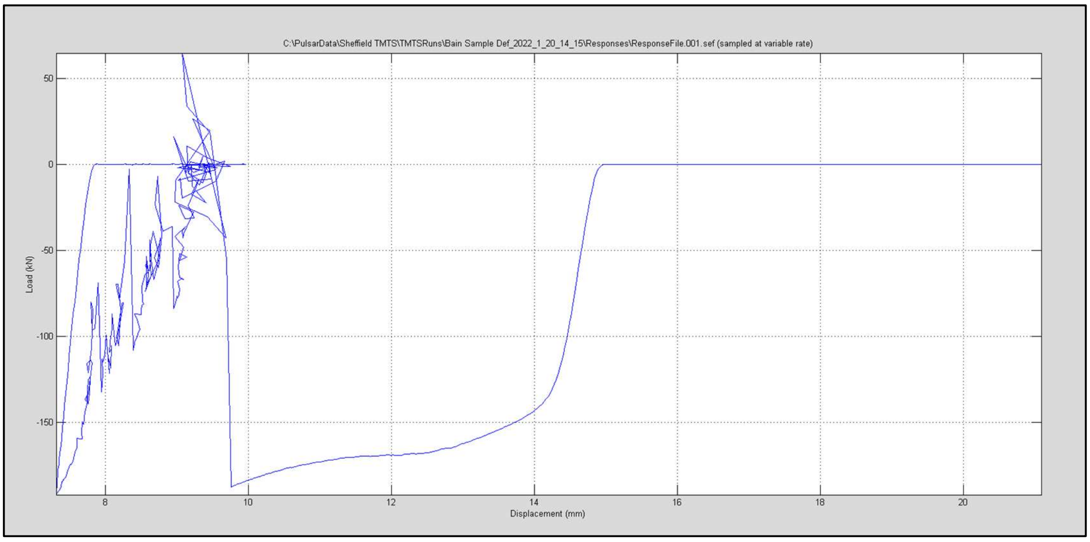

Figure 5.9: Load-displacement graph for Sample 1 after heat treatment, showing the early brittle failure.

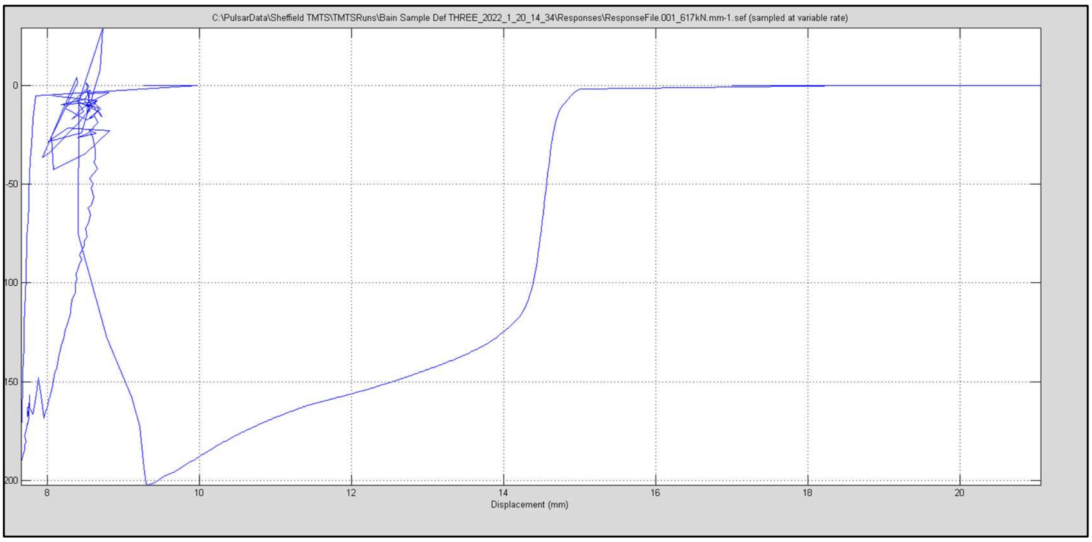

Figure 5.10: Load-displacement for Sample 3 after heat treatment, showing the early brittle failure.

Figure 5.11 shows the stress-strain curve obtained for sample 2.

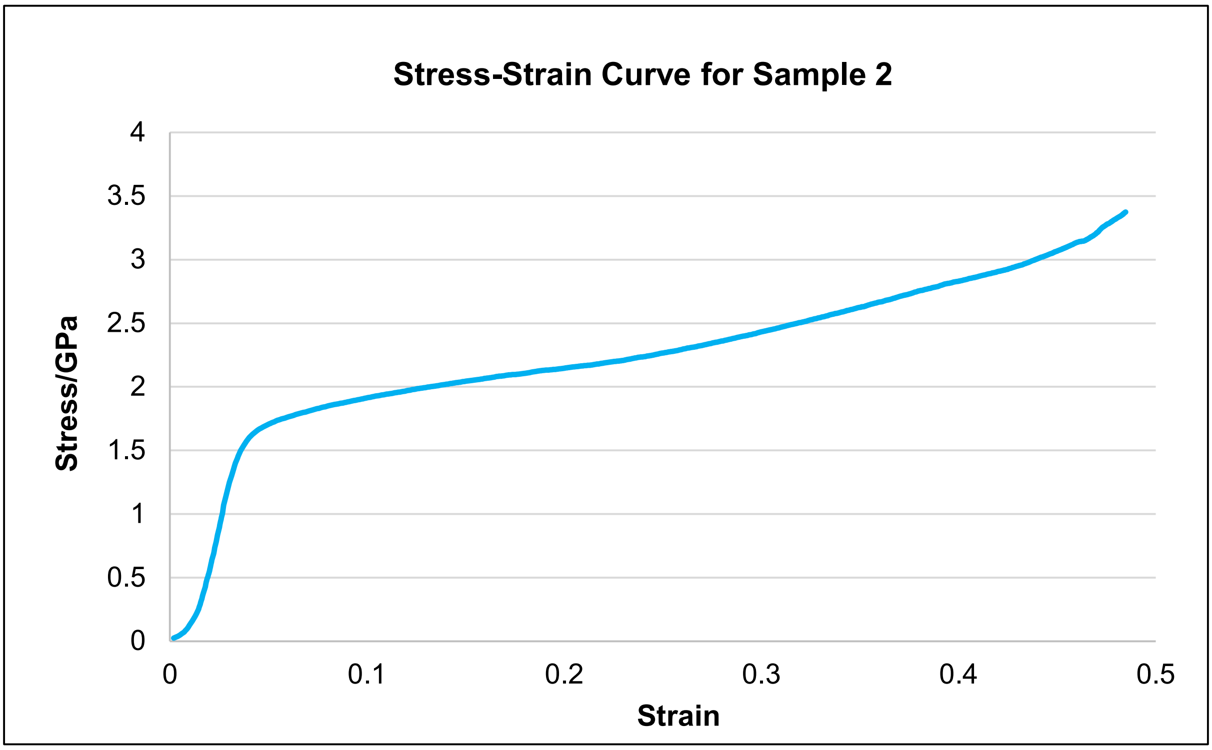

Figure 5.11: Compression stress-strain curve for Sample 2, deformed to a strain of 0.5.

5.3 Discussion

5.3.1 Alloy Composition and OES Results

The OES results in Table 5.3 show that the manganese content is lower than the 2 wt.% aim content, due to either segregation or losses during the casting process.

5.3.2 Thermocouple Readings

The thermocouples readings displayed in Figure 5.3, show that the TMC machine is sufficient for the long isothermal treatments utilised, with little to no deviation in temperature during the hold. However, the machine can take time to correct the temperature mainly during the rise to the austenisation heat treatment step and the quenching step. While the temperature fortunately did not drop below the M_s temperature of the steel (285°C), the machine's slow correction should be noted for any future work with the TMC and isothermal holding temperatures close to the M_s temperature of the steel.

5.3.3 Microscopy Images

The sample microstructures appear to consist of bainitic sheaves and a mix of both thin film and blocky morphology retained austenite, which was the aim microstructure for the steels. This can be observed from the SE-SEM images displayed in Figure 5.6, Figure 5.7 and Figure 5.8, which helps to confirm that the current heat treatment route using the TMC machine available is sufficient to produce fine structured bainite. Figure 5.12 compares the SE-SEM image of Sample 2 with the example nanostructured bainite microstructure from Garcia-Mateo et al [72].

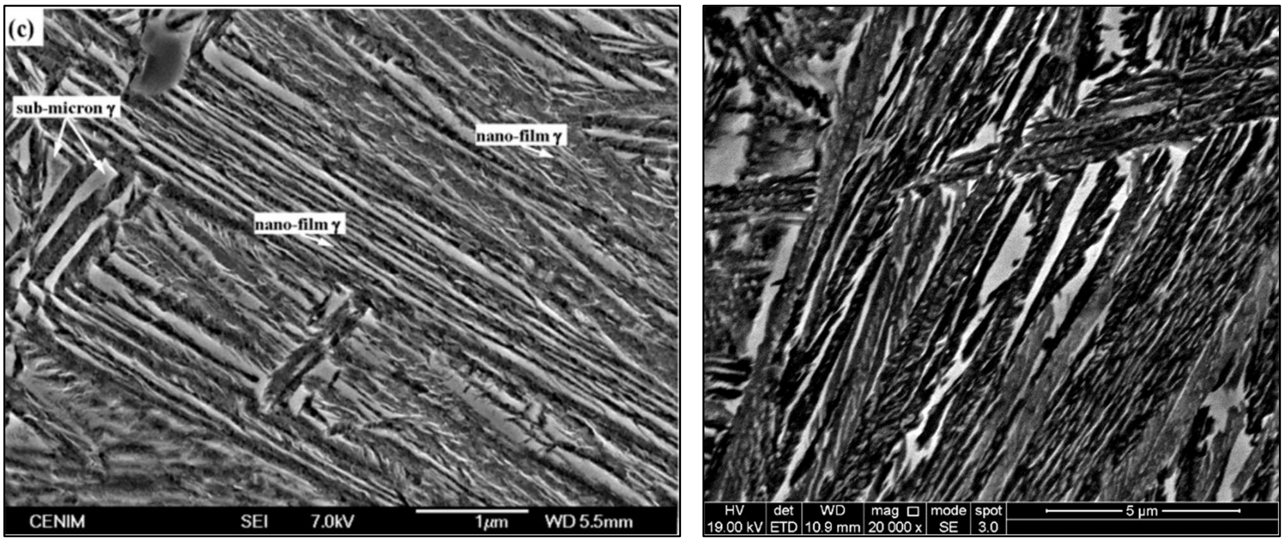

Figure 5.12: (Left) Example of the nanostructured bainite microstructure, obtained by isothermally holding at 250 °C for 16 hours [72]. (Right) SE-SEM images of Sample 2 after heat treatment.

The microstructures are both made from bainitic sheaves and retained austenite. However, there is a large proportion of thin film retained austenite in the microstructure from Garcia-Mateo et al. This is likely due to the lower M_s and transformation temperature utilised, as the microstructure in Figure 5.12 (left) was transformed at 250 °C for 16 hours, compared to the 325 °C for 3 hour transformation time for Sample 2.

The microstructures consist of lower bainite due to the low isothermal holding temperatures utilised, with the measured M_s of the steel being 285°C. It is difficult to observe whether any carbides have precipitated from the SEM images reported, however future transmission electron microscopy (TEM) imaging in could help to determine this. Morales-Rivas et al. [37] noted that coarser bainitic microstructures are produced at higher transformation temperatures, shown by larger bainitic sheave thicknesses and retained austenite blocks/films. This can also be observed with the higher isothermally heat treated samples, as shown in Figure 5.4, the effect is more clearly apparent between sample 1 (seen in Figure 5.6) and sample 3 (seen in Figure 5.8).

The optical micrographs can be observed to have bands of brighter regions, likely segregation of Mn within the samples. This could indicate that the one hour, 1150°C, holding heat treatment the ingot blocks were given prior to rolling, was insufficient to fully homogenise the microstructure. British Steel's R&D team suggested holding the ingots for at least 2 to 3 hours prior to rolling to correct this.

5.3.4 Compression Testing Results

The brittle failures of Sample 1 and Sample 3 under compression, at a strain rate of 0.1 s^{-1}, indicate that the TRIP effect likely occurred in both samples during deformation. This would cause the retained austenite to form untempered martensite, leading to brittle failure. It is unclear as to why Sample 2 did not fail in a similar manner and was able to be deformed to the aim strain of 0.5. It must be considered that the compression testing was performed on only one sample from each condition due to time constraints through COVID-19, and therefore it would not be accurate to state that Sample 1 and 3 would always fail before reaching a strain of 0.5. With the stress-strain curve for Sample 2, the results show that the sample has a high yield strength of 1.6 GPa and has a moderate work hardening rate as expected due to the retained austenite present.

5.4 Conclusion

Nanostructured bainite containing retained austenite was able to be produced using the TMC machine. The temperature is well controlled during the isothermal heat treatment and the PSC samples allow for compression testing using the TMC machine in addition. However, the morphology still contains a large amount of blocky retained austenite. As stated previously, future alloy compositions will have lower transformation times to alleviate this issue, in addition to secondary tempering steps to help transform some of the larger remaining retained austenite blocks.

Unfortunately, it was not possible to investigate the stability of the retained austenite present in the samples due to issues caused by the pandemic. This will be rectified in future work, where samples will undergo compression testing using the TMC machine to investigate the TRIP reaction in more detail. Alloy compositions of interest will also be developed to rod form, heat treated and cold drawn to study the drawability of the carbide-free bainite microstructure. The work from this past year and the route established to produce nanostructured bainite within the university should assist in investigating whether it is possible to develop an alternative to pearlitic rod that can be drawn to high strain and retain adequate ductility. In doing so higher strengths, and therefore cost savings in weight, could be achieved in the rod and wire industry and the applicability of nanostructured bainite would expand.

6.0 Carbide Free Bainite Work 2

6.1 Introduction

With the success of using the heat treatment route that produced the first carbide free bainite samples (this alloy being referred to as BAIN 0), the next stage was to develop more carbide free bainitic microstructures. Though the first bainitic steel grade samples were a success, the retained austenite volume fraction was quite high, and a lot of the retained austenite appeared to be blocky in nature. Therefore, four new alloy grades were to be developed. The aim of processing these alloys was to:

- To investigate the effect of the varied M_s temperature between the alloys, had on the microstructural and mechanical properties
- To investigate whether the changing the additions of Mn and Cr present in the alloys, had on the kinetics of the bainite transformation
- To investigate whether the increasing the addition of carbon from 0.4 to 0.5 C wt.% changed any of the mechanical or microstructural properties
- To observe whether a secondary isothermal hold (referred to as a tempering step) would further reduce the fraction of retained austenite present

The effect of the martensitic start temperature was investigated by utilising different weight percentage amounts of the alloying additions: carbon, manganese, and chromium. As mentioned previously, the silicon addition cannot be modified to <1.5 wt.%, as the addition suppresses the formation of cementite during the bainitic transformation that would otherwise form. This also encourages the carbon to stabilise the retained austenite. Typically, very fine bainitic microstructures are produced using very low transformation temperatures, with some treated at temperatures as low as 125°C [35], [72]. This is to produce a fine microstructure which not only improves the mechanical properties of the steel due to the higher grain volume, but transforming at such low temperatures helps to produce film-like retained austenite. This morphology is more stable than the blocky polygonal morphology. The microstructures produced by this technique have thin ferrite plates that can be less than 150 nm in thickness [48], [49]. The fine microstructure has the added benefit of allowing carbon atoms to diffuse over shorter distances into the retained austenite, helping to stabilise the phase and discourage the TRIP effect from occurring during deformation [41], [73]. With this aim in mind, the 4 alloy compositions that were chosen are shown in Table 6.1.

Table 6.1: The alloy compositions of the 4 different produced steel grades.

Steel	C	Si	Mn	Cr	M_s (°C)
	(wt.%)				
BAIN 1	0.40	2.00	0.75	0.50	343
BAIN 2	0.40	2.00	1.25	1.50	295
BAIN 3	0.50	2.00	0.75	0.50	300
BAIN 4	0.50	2.00	1.25	1.50	251

The M_s temperature varies by approximately 50°C between the 4 grades. The M_s temperature of each of the compositions was determined using the MAP_STEEL_MUCG83 program, a free source code program available through the University of Cambridge, materials algorithm project (MAP) library [74]. All the grades were isothermally transformed at as low temperature as possible, to ensure a fine microstructure. Then the microstructures and mechanical properties of the alloys were compared to distinguish the effect on the variation between the M_s and the subsequent transformation temperatures.

Varying the additions of manganese and chromium was not only done to produce different M_s temperatures between the grades. Caballero et al [46] investigated accelerating the transformation times for the nanostructured bainites by varying the chemical composition of the steels. One variation between the alloys investigated was to reduce the amount of carbon, manganese, chromium and molybdenum additions. By changing the additions in between alloy samples BAIN 1-4, the aim is to increase the transformation times in the alloys with lower amounts of Cr and Mn. This would result in a larger and a lower volume fraction of bainite and retained austenite respectively and therefore improving the mechanical properties of the treated alloys. However, this comes at the expense of lower possible transformation temperatures and as such, it will need to be seen which of two effects (transformation temperature or kinetics) has a larger impact on the final microstructure and mechanical properties.

The carbon weight percentage of the alloys was chosen to follow on from British Steel's preliminary work investigating past bainitic steel grade steels. Morales-Rivas states that carbide free bainitic grades typically have a carbon composition ranging from 0.6 to 1.0 wt.% [37] whilst in reality, lower carbon nanostructured bainite exists as shown in the work on 0.26 C wt.% bainite by Soliman et al [47]. However, with such low carbon, the chemistry composition is often more complex to maintain a low Ms temperature, such as utilising Nickel.

The relatively low carbon composition utilised in the composition of BAIN 1-4 compared to other work on nanostructured bainites is due to British Steel's own findings on the topic. It was found that high carbon grades (around 0.7 to 1.0 wt.% C) could not reach adequate elongation and ductility levels for wire drawing. Therefore, the aim of the preliminary work was to produce bainitic steel with a UTS of 1600 MPa and elongation values of 20-30%. Subsequently, 0.3 to 0.4 wt.% C was recommended, as any lower carbon wt.% would result in rod with an inferior UTS to a pearlitic grade. BAIN 3 and 4 have slightly higher carbon contents at 0.5 C wt.% for comparison, to determine whether the additional carbon has any benefits on stabilising the retained austenite or through achieving a lower transformation temperature.

The final aim is to investigate the effect of tempering the bainitic microstructures. This involves providing a second isothermal holding treatment to each of the samples after the initial bainitic heat treatment. In research, a similar technique is performed and referred to as two-step isothermal heat treatment. The reasoning behind two or even multiple isotheral holding steps is to further transform the retained austenite present within the microstructures. As the retained austenite is stabilised and the carbon content within the phase increases, the Ms of the temperature of the phase is lowered such that transformation upon further isothermal holds is possible. Work by Soliman et al. [47] and Papadimitriou and Fourlaris [75] has found that the transformation can result in another generation of bainitic ferrite, enhancing the impact toughness and tensile strength of the steels. However, unlike in the research of Soliman et al, producing a single heat treatment schedule with two different isothermal holding temperatures was not possible with the resources available and as such, samples underwent the second isothermal holding step at a later stage. The aim is to investigate the effect of a second isothermal holding step on the different alloys. This step may further decrease the volume fraction of retained austenite and comparatively increase the volume fraction of bainitic ferrite, which help to stabilise the retained austenite that remains and enhance the ductility of the bainite by delaying the TRIP effect during deformation.

6.1.1 Laboratory Work

The steel ingots were once again produced and processed using the route discussed in section 3. Unlike the previous cast ingot slabs, the sectioned ingots were rolled using the facilities at SAMI, University of Swansea. Unfortunately, the compositions of the 4 new alloy ingots were not checked as was the previous produced alloy, BAIN 0, due to time constraints.

The samples were given heat treatments using the salt bath facilities at Summitglow Ltd. Figure 6.1 and Table 6.2 display the heating schedule of the different PSC samples. The initial heating to the austenisation step for 5 minutes at 950 °C was performed by two high temperature salt baths, as placing the samples directly in the 950 °C salt bath would cause a dangerous overflow of molten salt. The samples were quenched down and held to the isothermal holding temperature in a final lower temperature salt bath, before being water quenched to room temperature. Unfortunately, BAIN 4 was not processed in time to produce samples for the project. The temperature within the samples was monitored using thermocouples during the heat treatments.

Table 6.2: The heat treatment schedule chosen for the 4 alloys to produce a bainitic microstructure. Note that BAIN 4 was not processed due to time constraints.

Sample ID	Austenisation Holding Temp. (°C)	Isothermal Holding Temp. (°C)	Holding time (hours)
BAIN 1	950	350	3
BAIN 2	950	310	3
BAIN 3	950	310	3
BAIN 4	950	260	3

Table 6.3 shows the second isothermal holding step performed. This second isothermal hold was performed using a box chamber furnace facility within the university. Each sample was held for 3 hours before being water quenched to room temperature.

Table 6.3: The heat treatment schedule for the 2nd isothermal holding step for the 3 heat treated alloy compositions.

Sample ID	2nd Isothermal Holding Temp. (°C)	2nd Holding time (hours)
BAIN 1 T	270	3
BAIN 2 T	270	3
BAIN 3 T	270	3

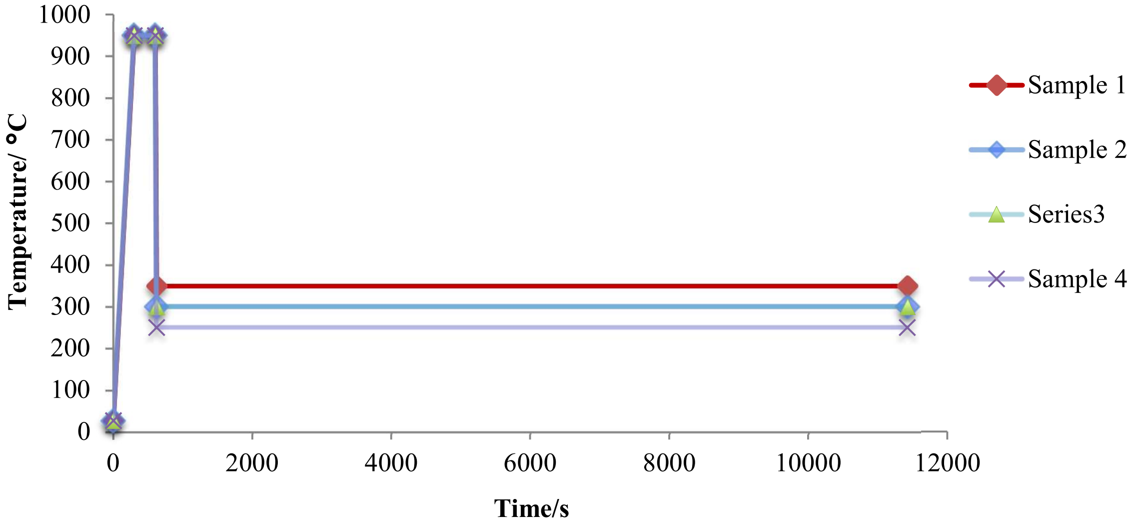

Figure 6.1: Schematic diagram of the heat treatment schedule for the 4 different alloys.

To analyse the microstructures of the different samples, SEM, TEM, STEM and EDS were utilised. XRD and EBSD were required not only to quantify the amount of retained austenite present, but also, to assess the morphology of the retained austenite within the samples.

Deformation was performed using the TMC at ambient temperature to gather data on the mechanical properties. In addition, Vickers hardness testing was performed to compare the hardness between the different alloys and change through the multiple processing stages.

6.2 Results

6.2.1 SEM

Figure 6.2 through to Figure 6.4 are SEM images taken of the samples after the heat treatment performed using molten salt baths. The images were taken using the FEI Inspect F50, with the experimental technique described in Section 3. The microstructures consist of nanostructured bainite and both blocky and thin film morphology retained austenite.

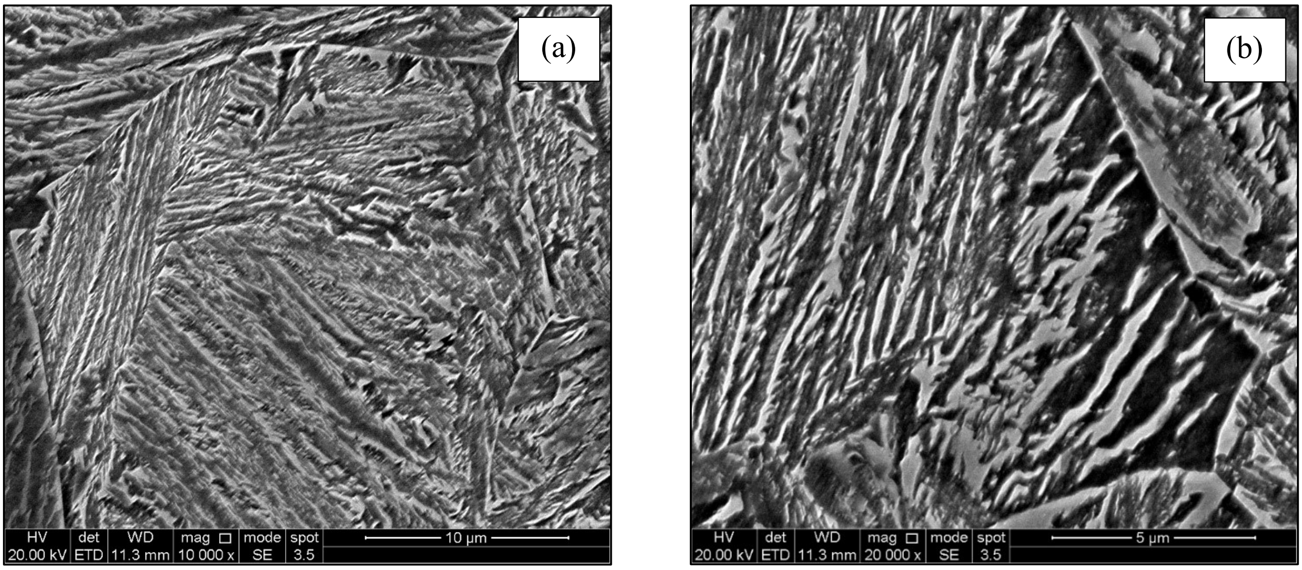

Figure 6.2: SE-SEM micrographs obtained from BAIN 1 after heat treatment showing the nanostructured bainitic microstructure. BAIN 1 was isothermally held at 350 °C for 3 hours.

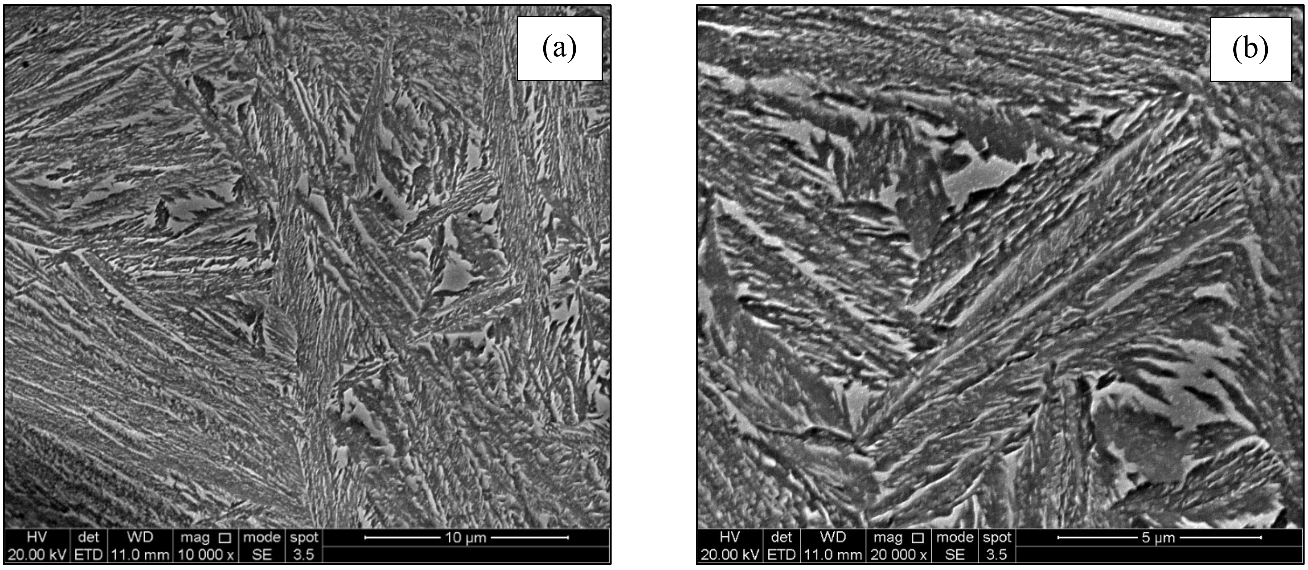

Figure 6.3: SE-SEM micrographs obtained from BAIN 2 after heat treatment showing the nanostructured bainitic microstructure. BAIN 2 was isothermally held at 310 °C for 3 hours.

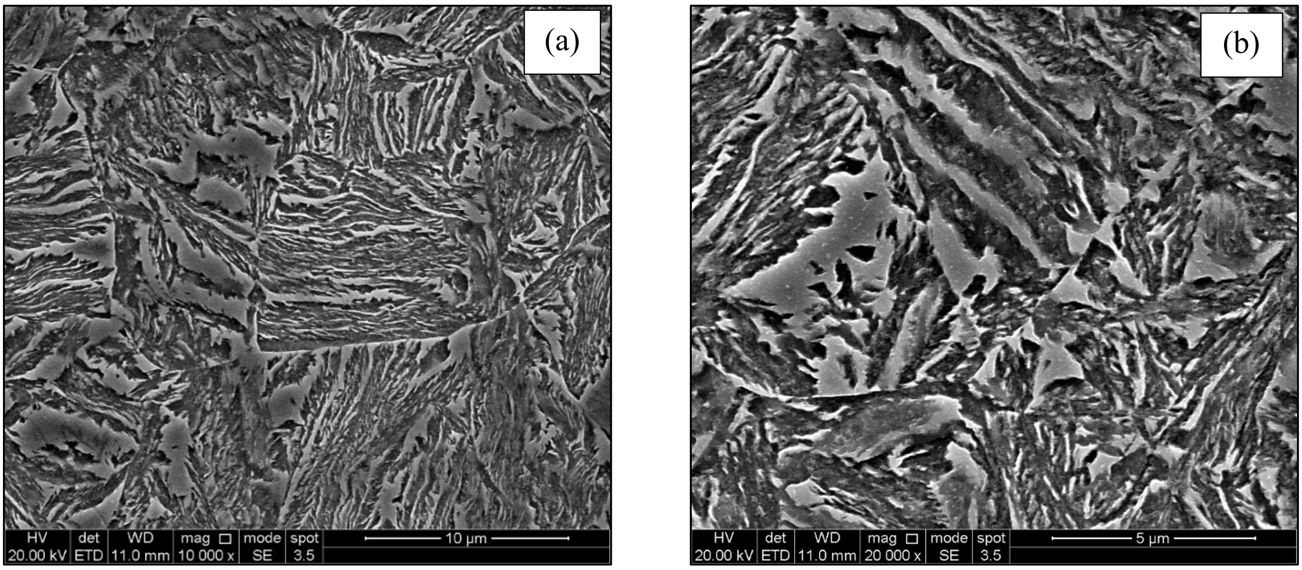

Figure 6.4: SE-SEM micrographs obtained from BAIN 3 after heat treatment showing the nanostructured bainitic microstructure. BAIN 3 was isothermally held at 310 ℃ for 3 hours.

Figures 6.5 through to Figure 6.7 displays the SE-SEM images of the microstructures obtained from the samples that were given a second isothermal holding heat treatment (referred to as tempered samples occasionally).

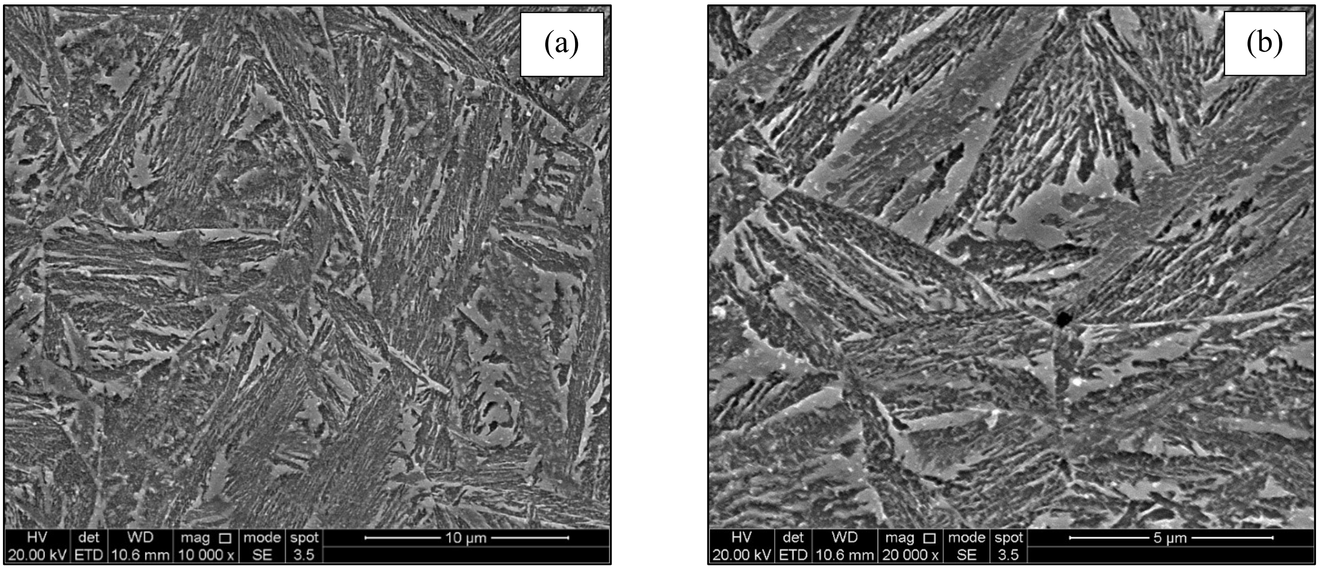

Figure 6.5: SE-SEM micrographs showing the nanostructured bainitic microstructure obtained from BAIN 1, after the second isothermal holding heat treatment. The second isothermal heat treatment was performed at 270 ℃ for 3 hours.

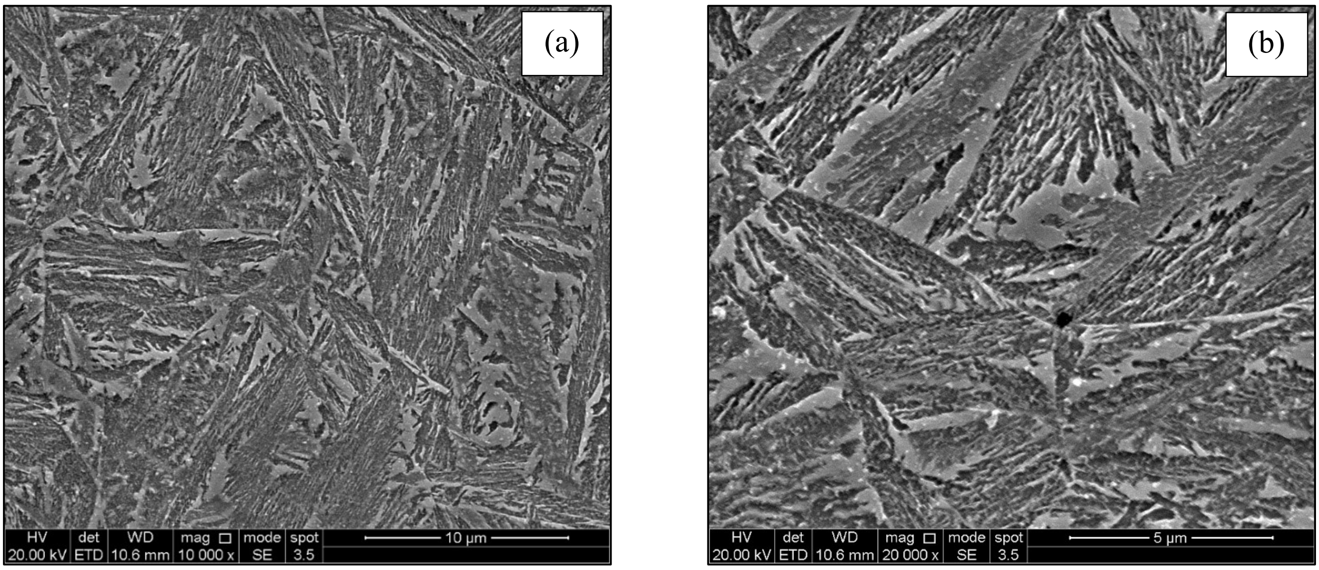

Figure 6.6: SE-SEM micrographs showing the nanostructured bainitic microstructure obtained from BAIN 2, after the second isothermal holding heat treatment. The second isothermal heat treatment was performed at 270 ℃ for 3 hours.

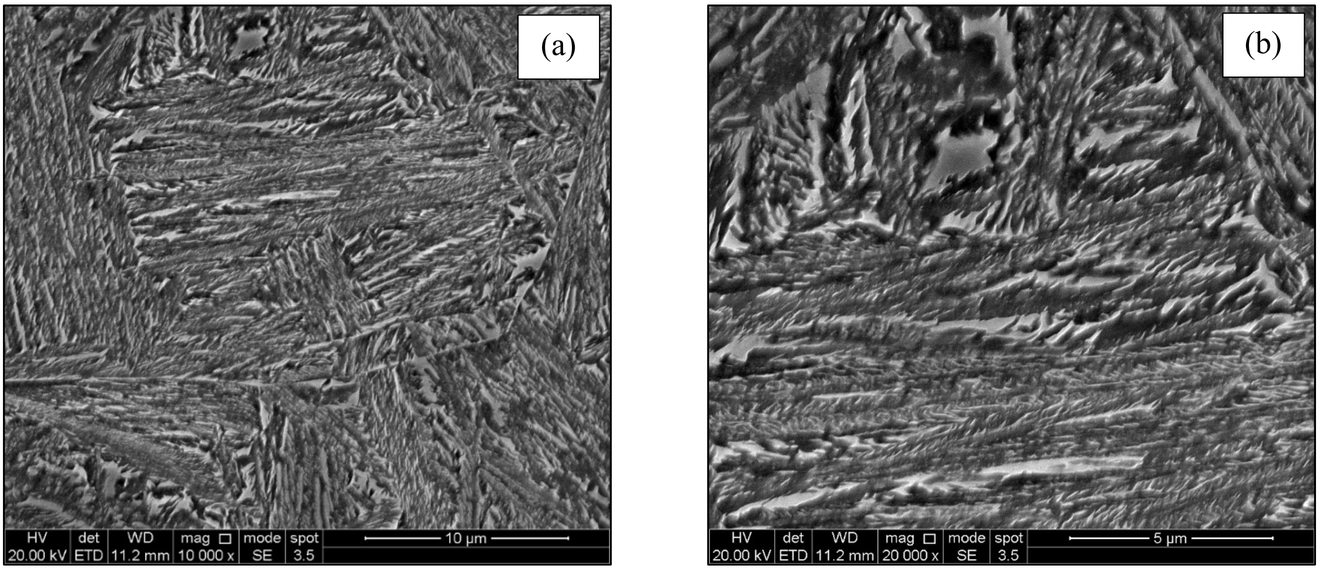

Figure 6.7: SE-SEM micrographs showing the nanostructured bainitic microstructure obtained from BAIN 3, after the second isothermal holding heat treatment. The second isothermal heat treatment was performed at 270 ℃ for 3 hours.

Figures 6.8 to Figure 6.10 display the SE-SEM images of the microstructures obtained after the samples were tempered and deformed, using the TMC. Each of the samples were cold compression tested to a strain of 0.5, at strain rate of 0.1 s^{-1}.

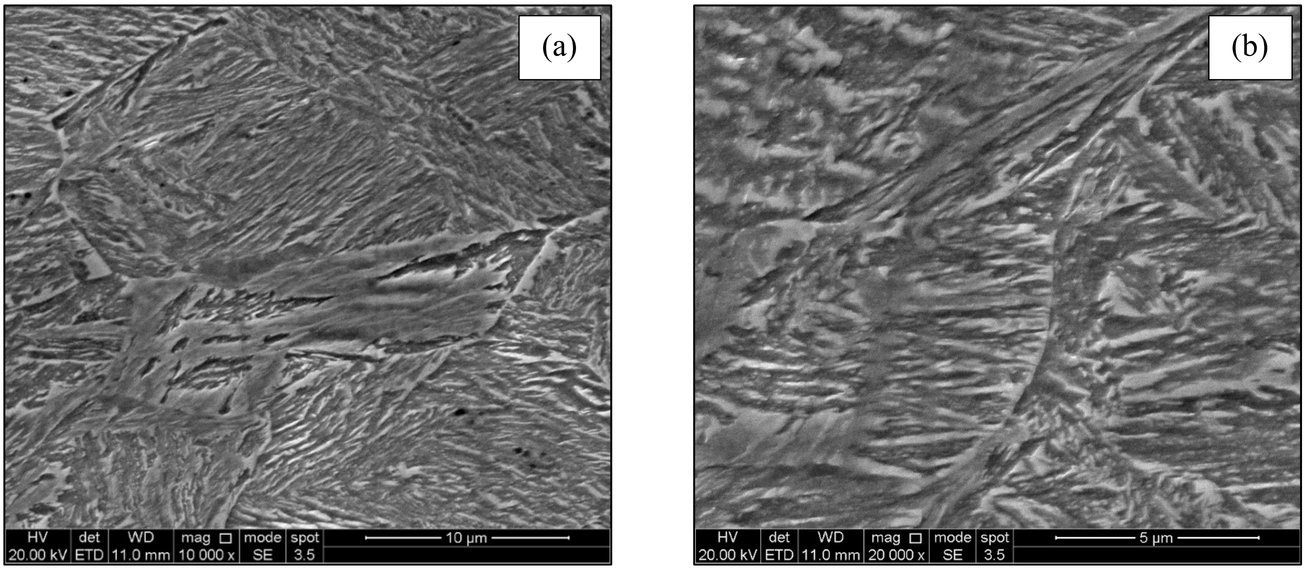

Figure 6.8: SE-SEM micrographs showing the microstructure obtained from BAIN 1, after the second isothermal holding heat treatment and cold compression testing.

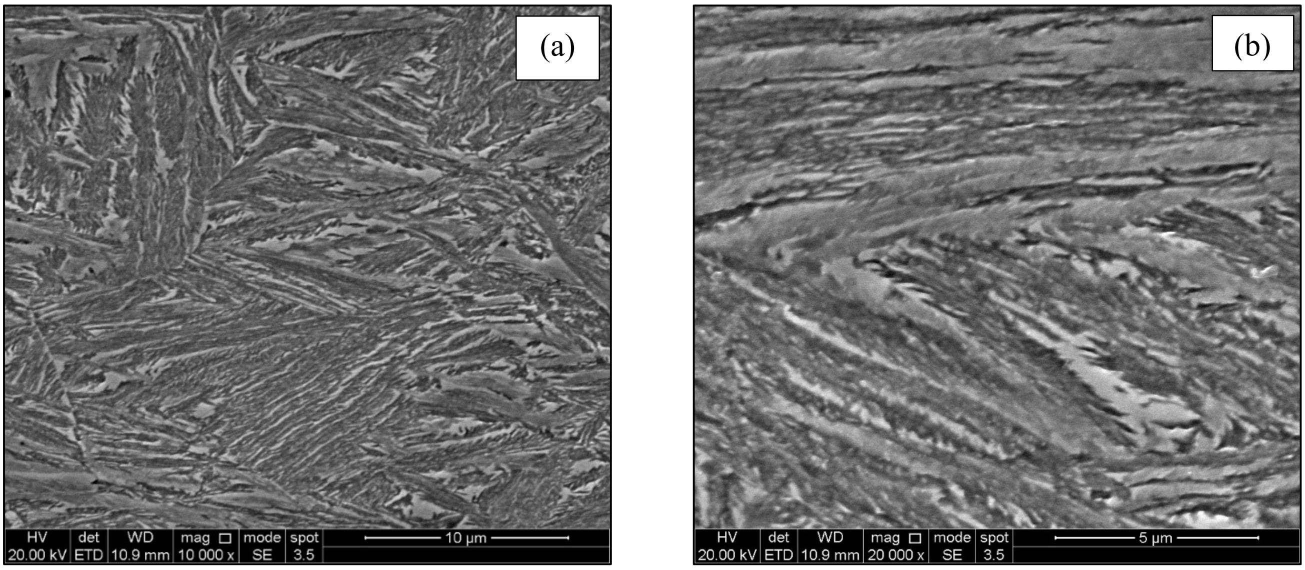

Figure 6.9: SE-SEM micrographs showing the microstructure obtained from BAIN 2, after the second isothermal holding heat treatment and cold compression testing.

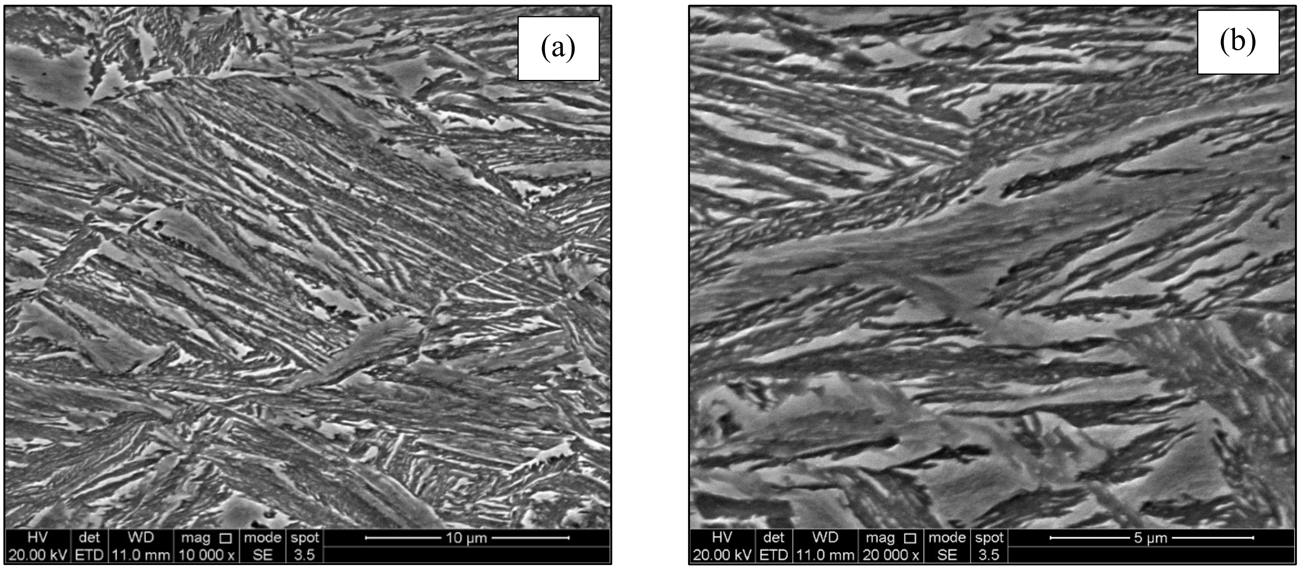

Figure 6.10: SE-SEM micrographs showing the microstructure obtained from BAIN 3, after the second isothermal holding heat treatment and cold compression testing.

6.2.2 TEM

Figures 6.11 to 6.16 are selected bright field TEM images of the alloy microstructures after being tempered and deformed. Figure 64 shows a diffraction pattern obtained from BAIN 1.

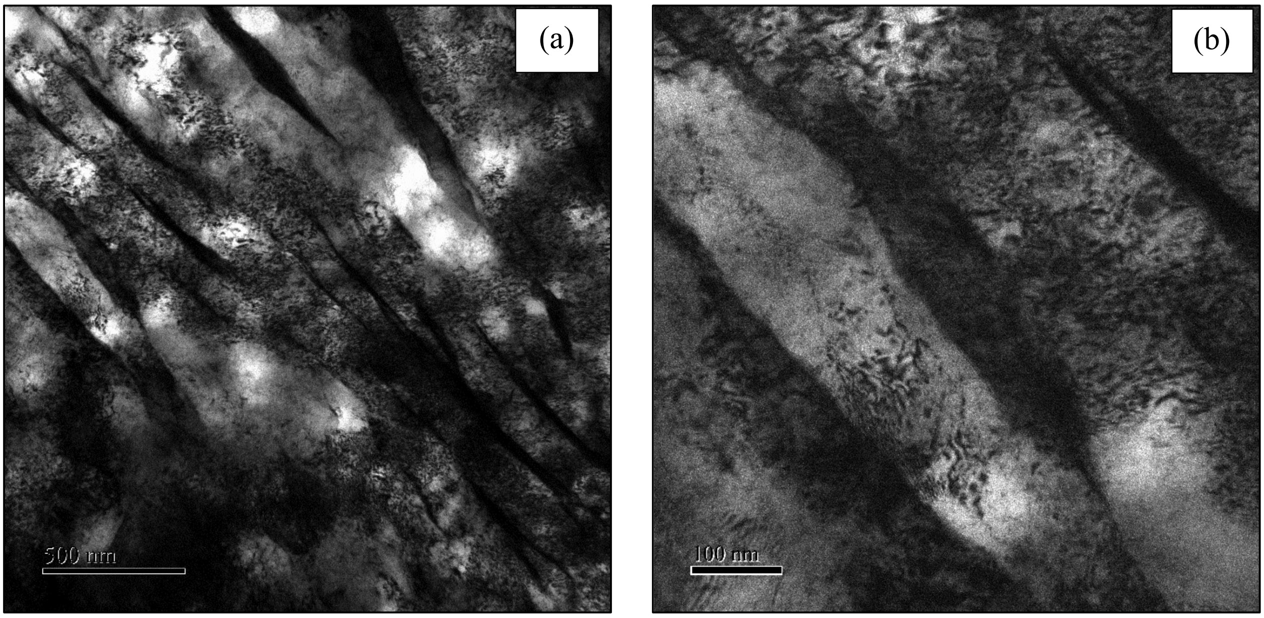

Figure 6.11: (a) and (b). TEM Images of the microstructure obtained in BAIN 1, after tempering and deformation.

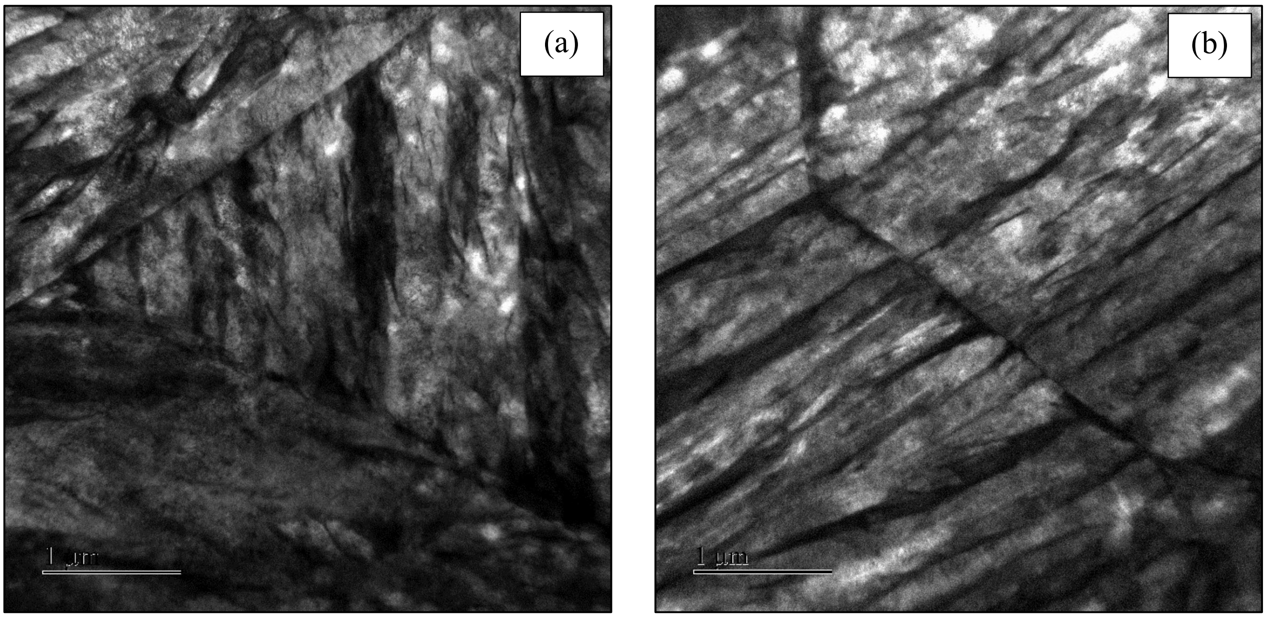

Figure 6.12: (a) and (b). TEM Images of the microstructure obtained in BAIN 1, after tempering and deformation.

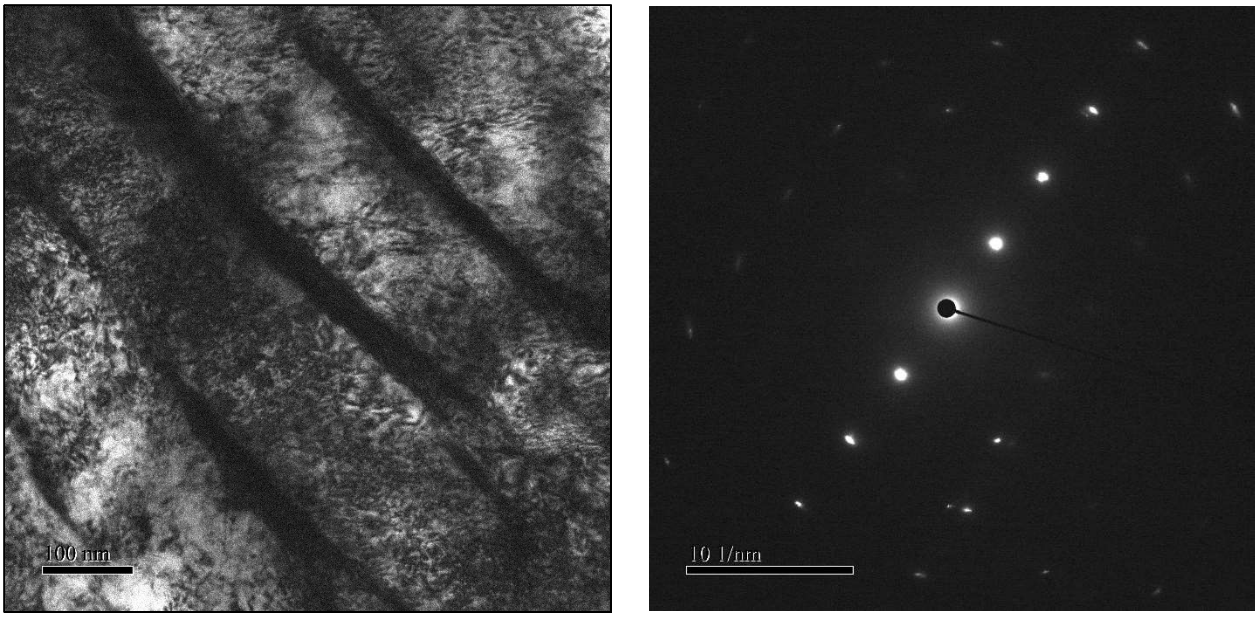

Figure 6.13: (Left) TEM image of the microstructure obtained in BAIN 1, after being tempered and deformed. (Right) The corrosponding diffraction pattern produced by focusing on the dark thin film regions.

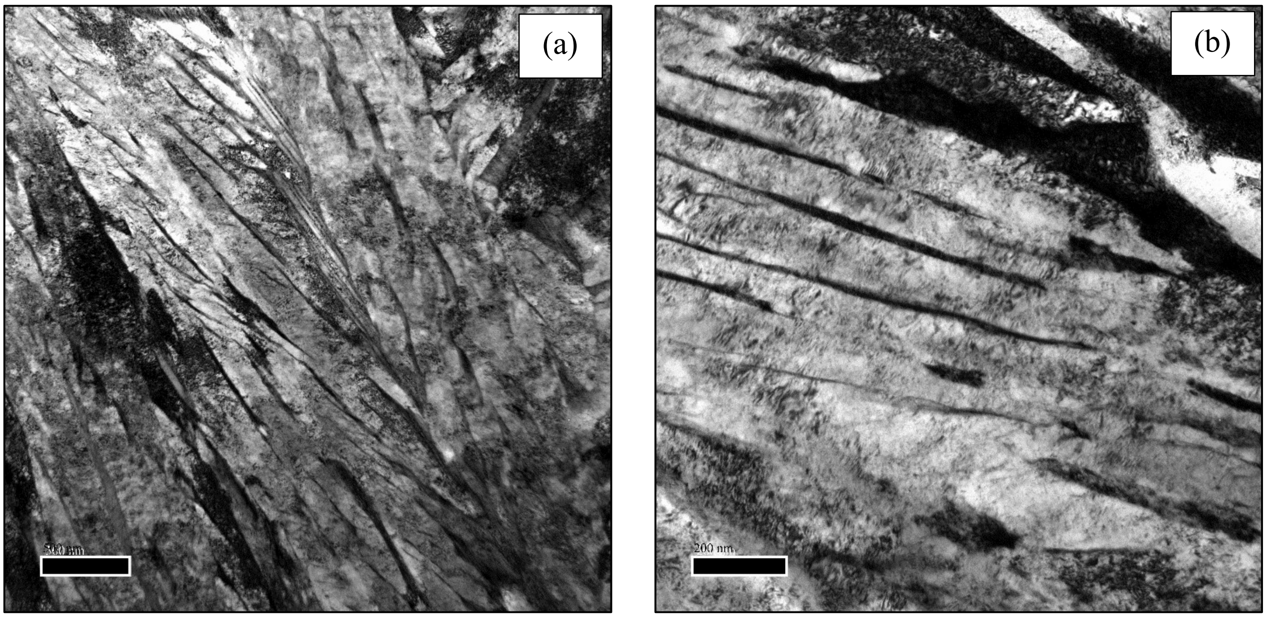

Figure 6.14: (a) and (b). TEM Images of the microstructure obtained in BAIN 2, after tempering and deformation.

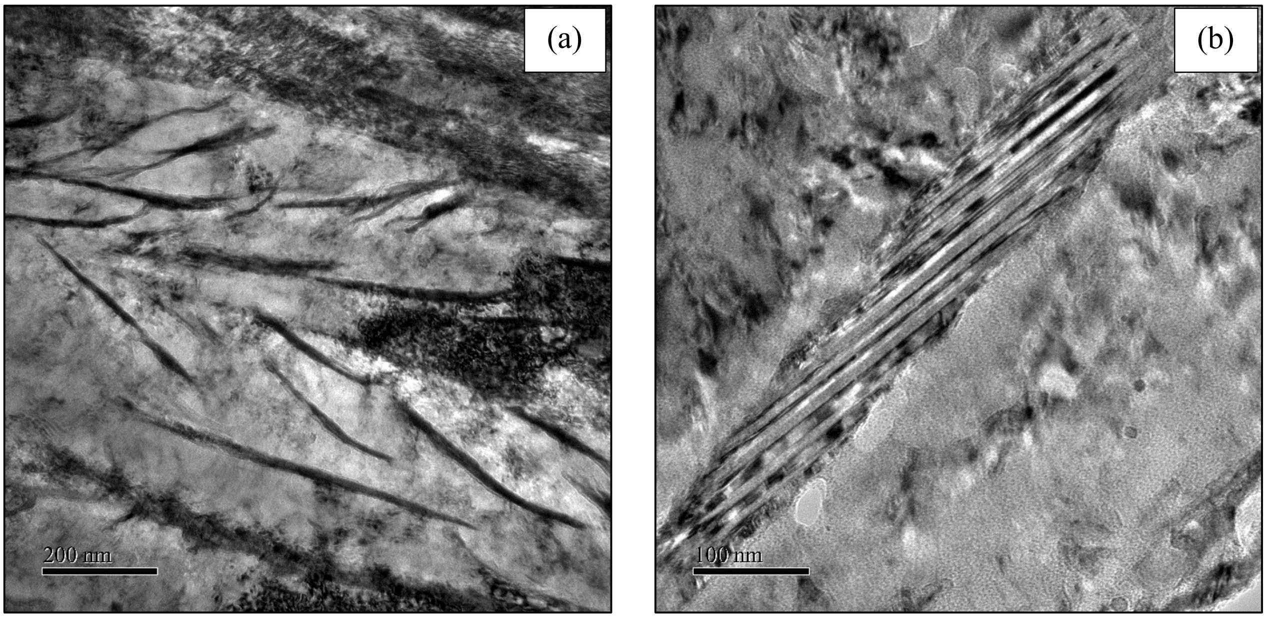

Figure 6.15: (a) and (b). TEM Images of the microstructure obtained in BAIN 2, after tempering and deformation.

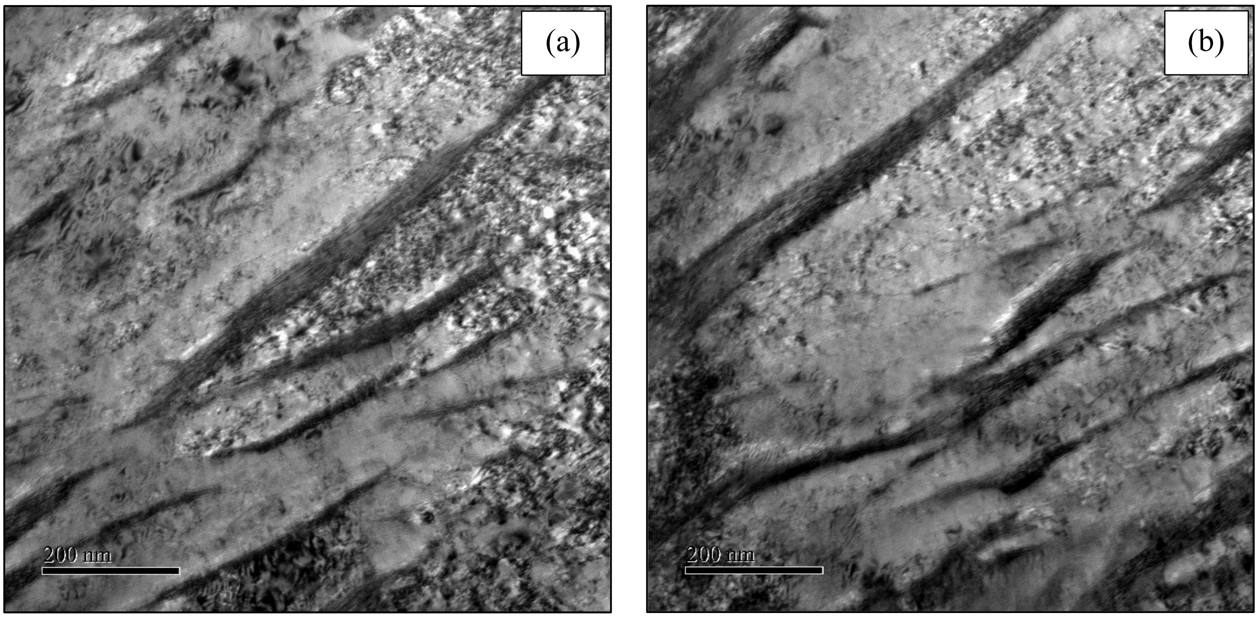

Figure 6.16: (a) and (b). TEM Images of the microstructure obtained in BAIN 2, after tempering and deformation.

6.2.3 STEM

Due to the quick forming oxide layer on the TEM samples and the difficulties in imaging the heavily deformed samples, STEM was utilised to gain more clearer microstructural images as seen in Figures 6.17 to Figure 6.24. EDS was also performed on these images, to study the distribution after heat treatment of the different elements present within the alloys.

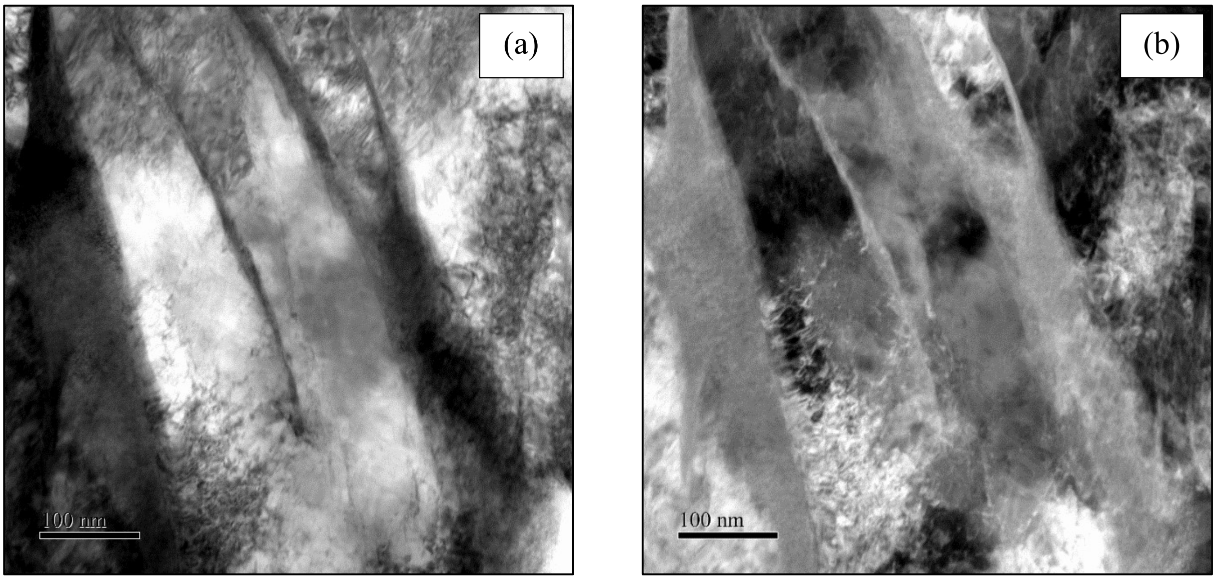

Figure 6.17: STEM images of BAIN 1 after being tempered and deformed where (a) is the brightfield image and (b) is the dark field image.

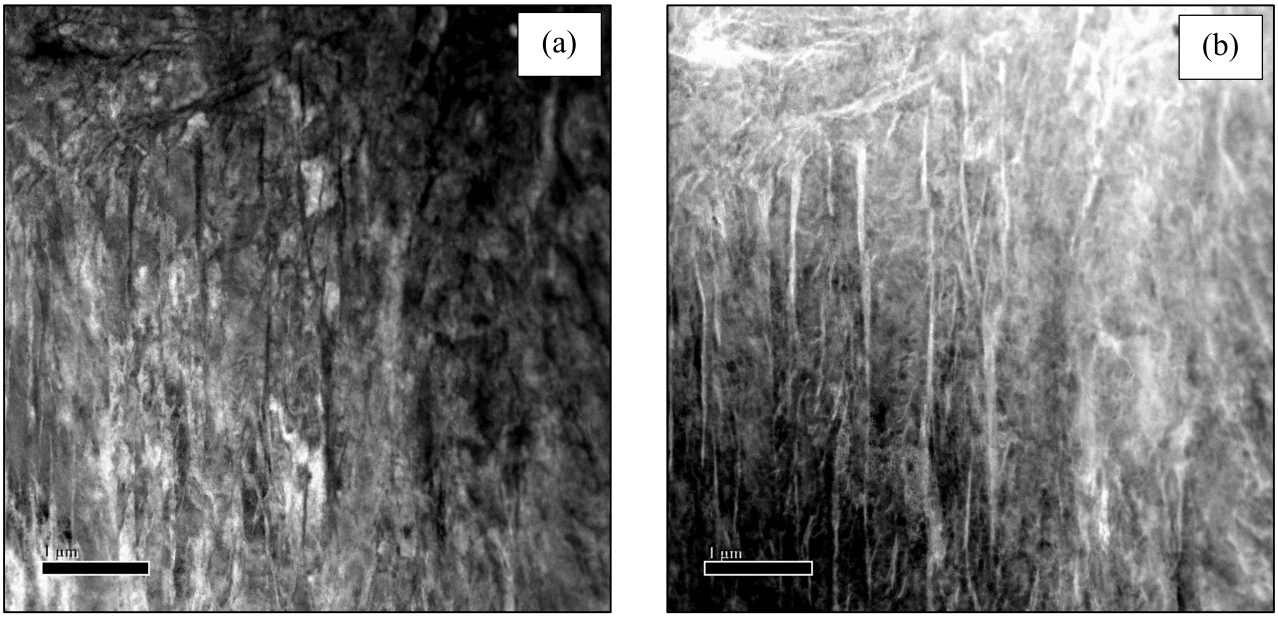

Figure 6.18: STEM images of BAIN 1 after being tempered and deformed where (a) is the brightfield image and (b) is the dark field image.

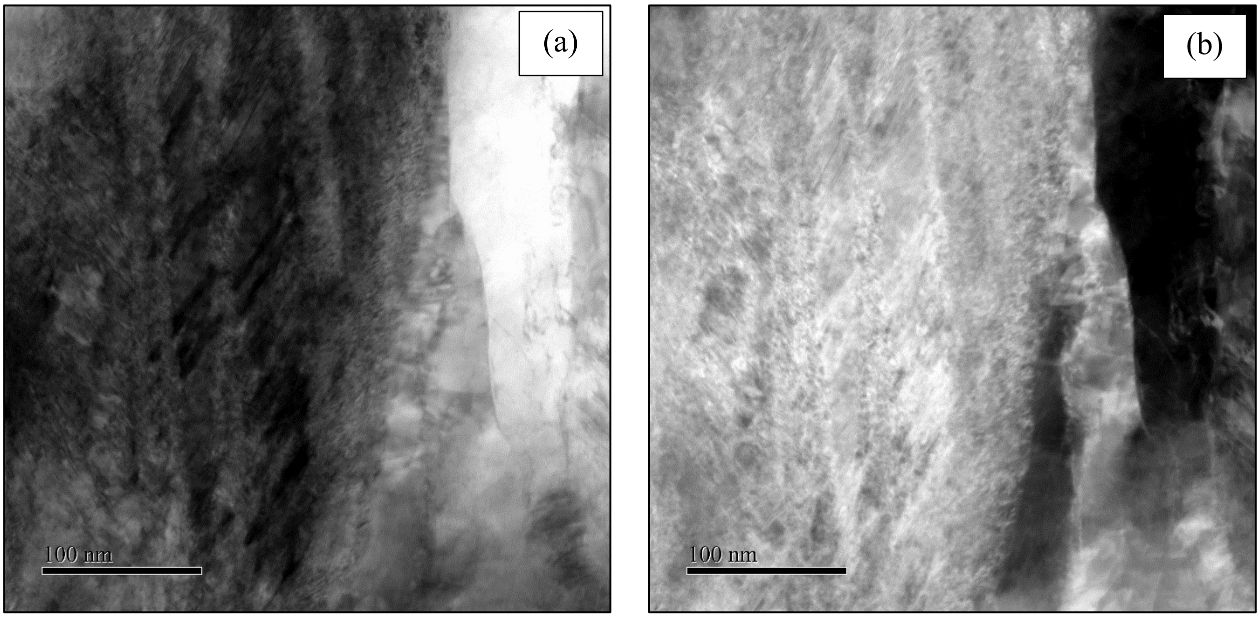

Figure 6.19: STEM images of BAIN 1 after being tempered and deformed where (a) is the brightfield image and (b) is the dark field image.

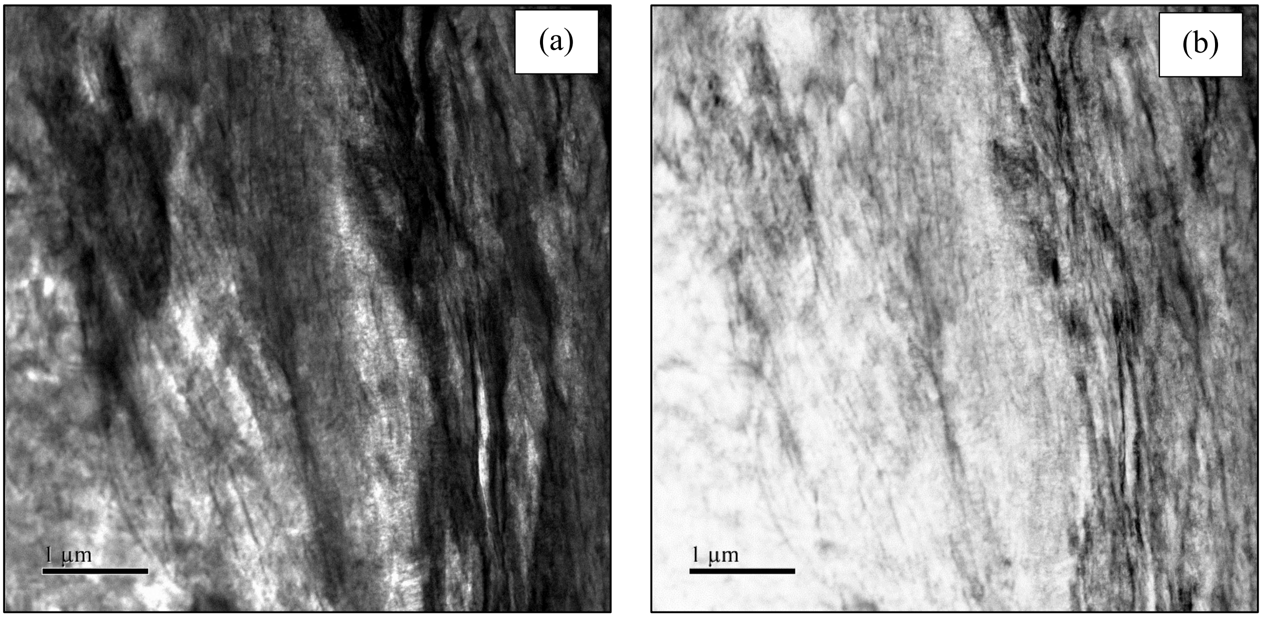

Figure 6.20: STEM images of BAIN 2 after being tempered and deformed where (a) is the brightfield image and (b) is the dark field image.

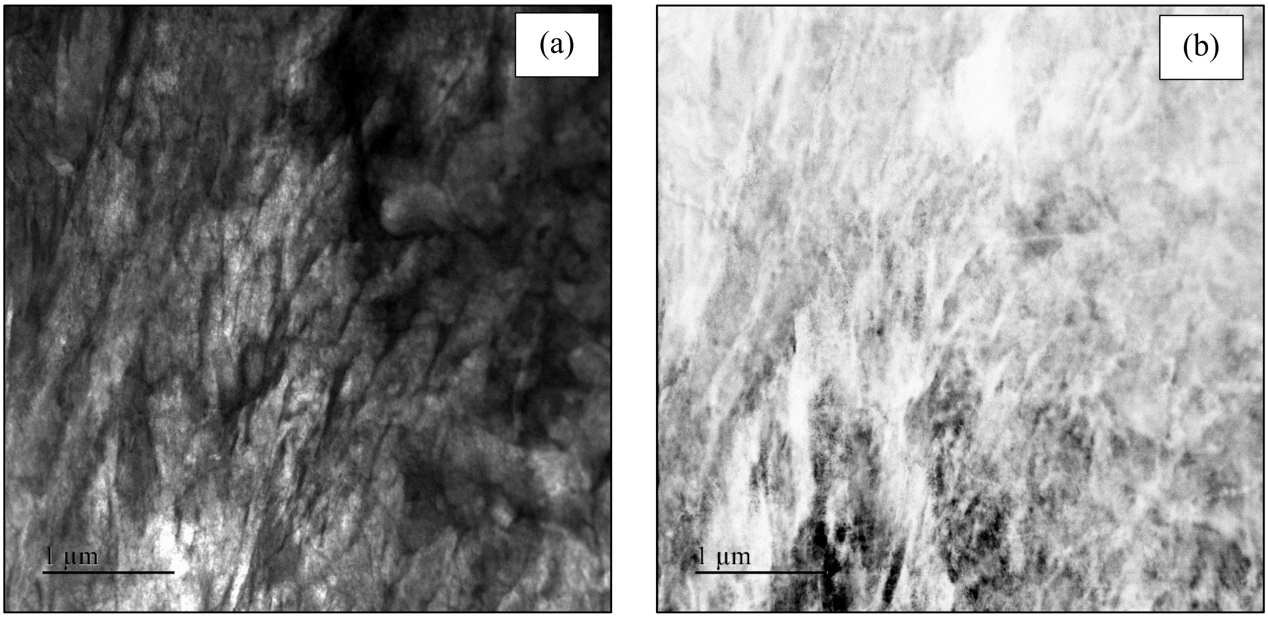

Figure 6.21: STEM images of BAIN 2 after being tempered and deformed where (a) is the brightfield image and (b) is the dark field image.

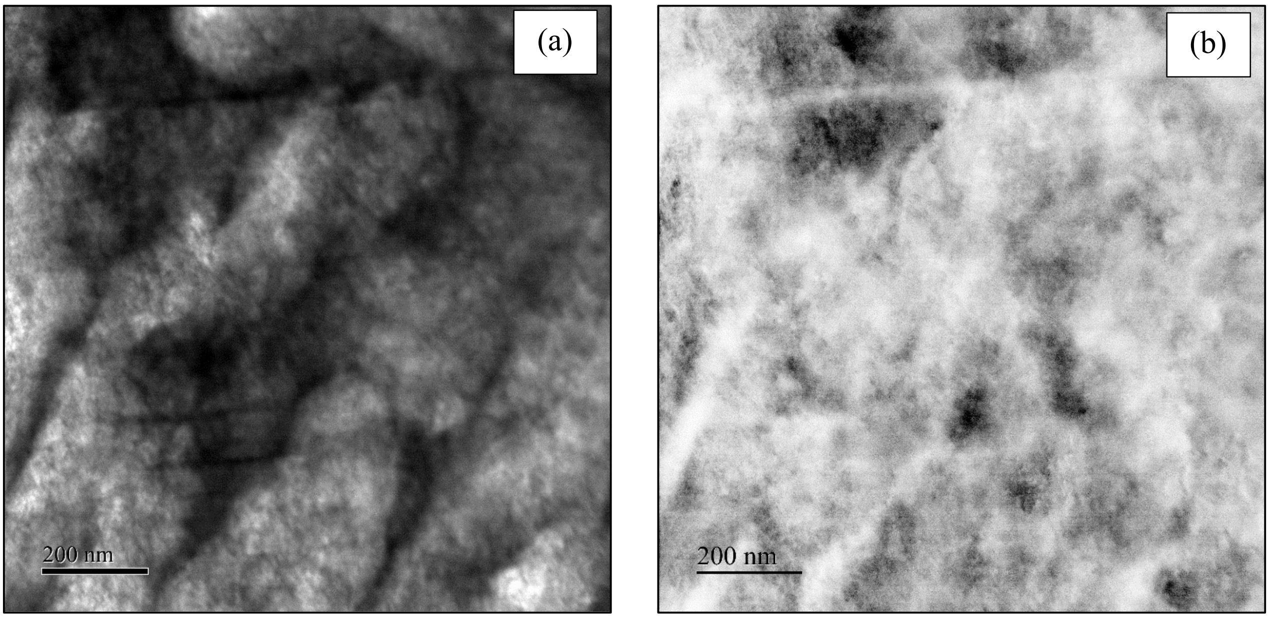

Figure 6.22: STEM images of BAIN 2 after being tempered and deformed where (a) is the brightfield image and (b) is the dark field image.

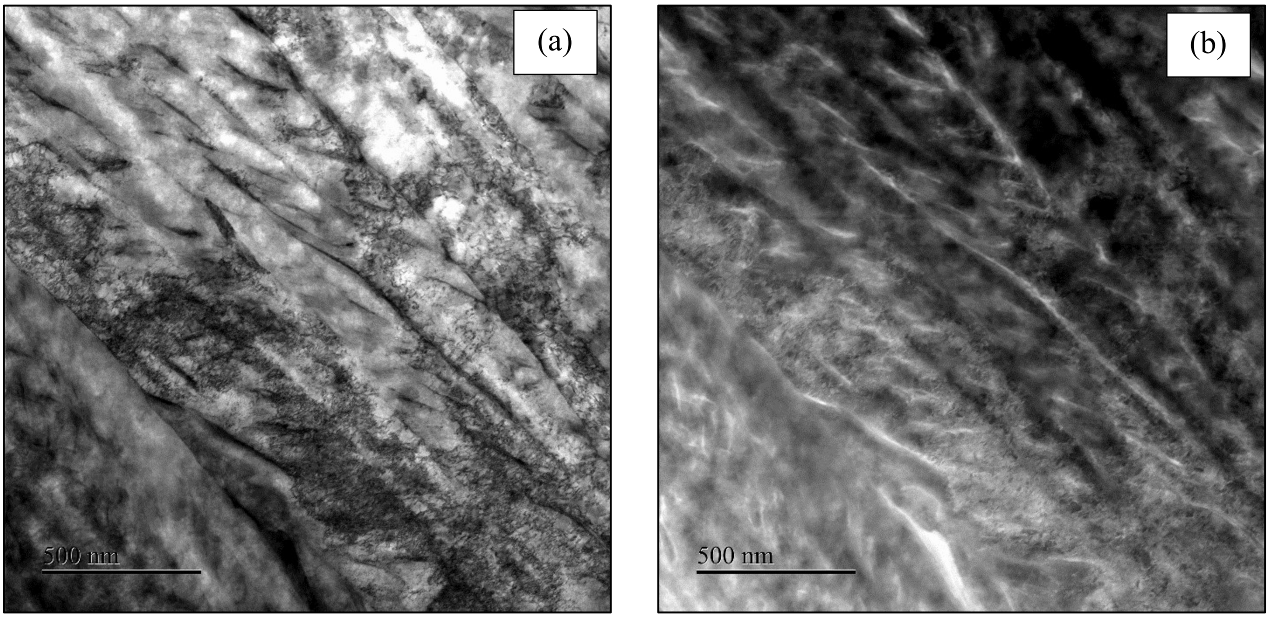

Figure 6.23: STEM images of BAIN 3 after being tempered and deformed where (a) is the brightfield image and (b) is the dark field image.

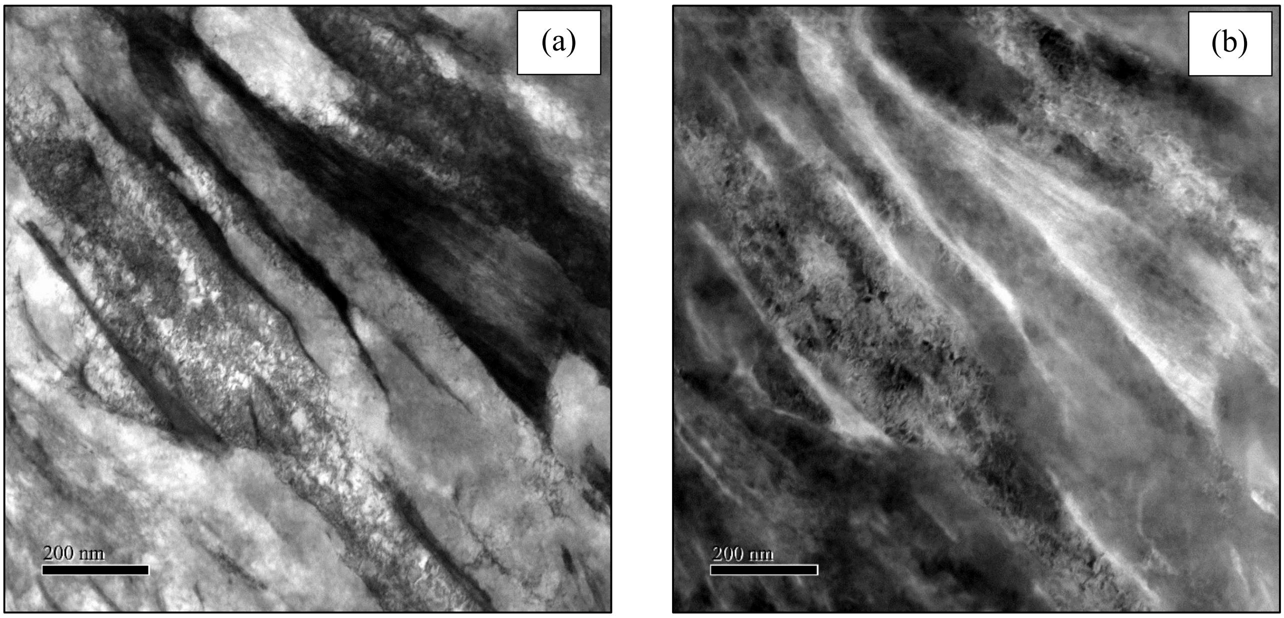

Figure 6.24: STEM images of BAIN 3 after being tempered and deformed where (a) is the brightfield image and (b) is the dark field image.

6.2.4 EDS

Figures 6.25 to Figure 6.31 show the STEM images which were utilised for EDS and the corresponding EDS quantified maps taken showing the distribution of carbon, iron, chromium, manganese and silicon.

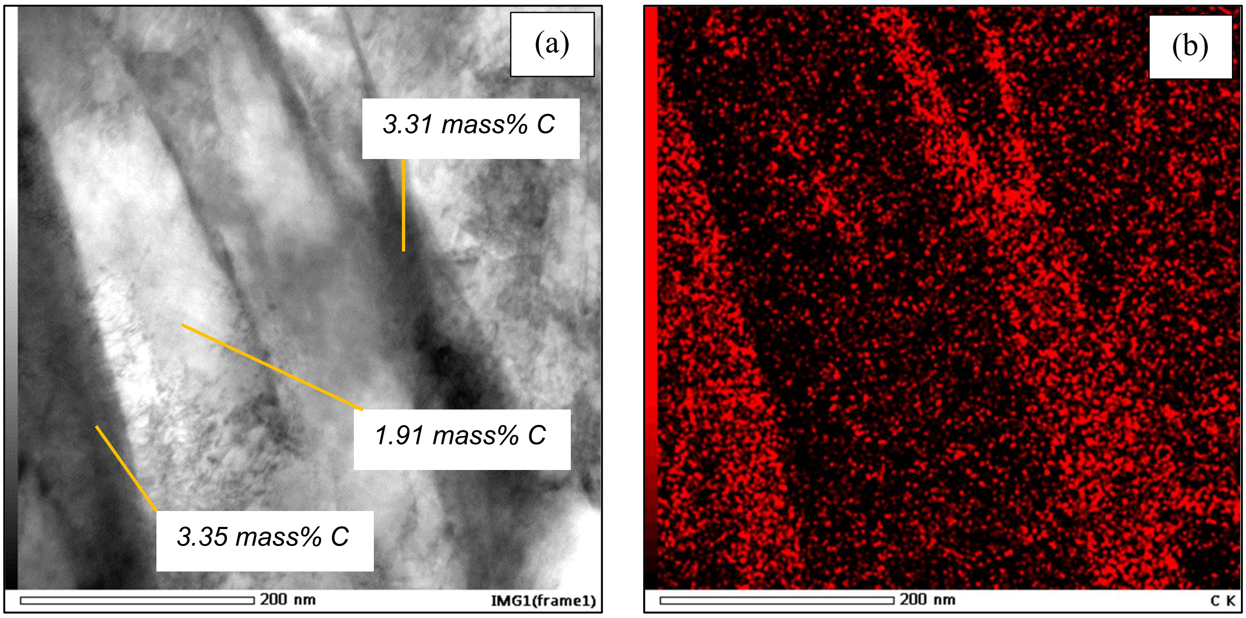

Figure 6.25: (a) Bright field STEM image of BAIN 1 after tempering and deformation. (b) Corresponding EDS quantified map of the carbon distribution in the STEM image. Point analysis was also done to determine the mass% of carbon in a selected area.

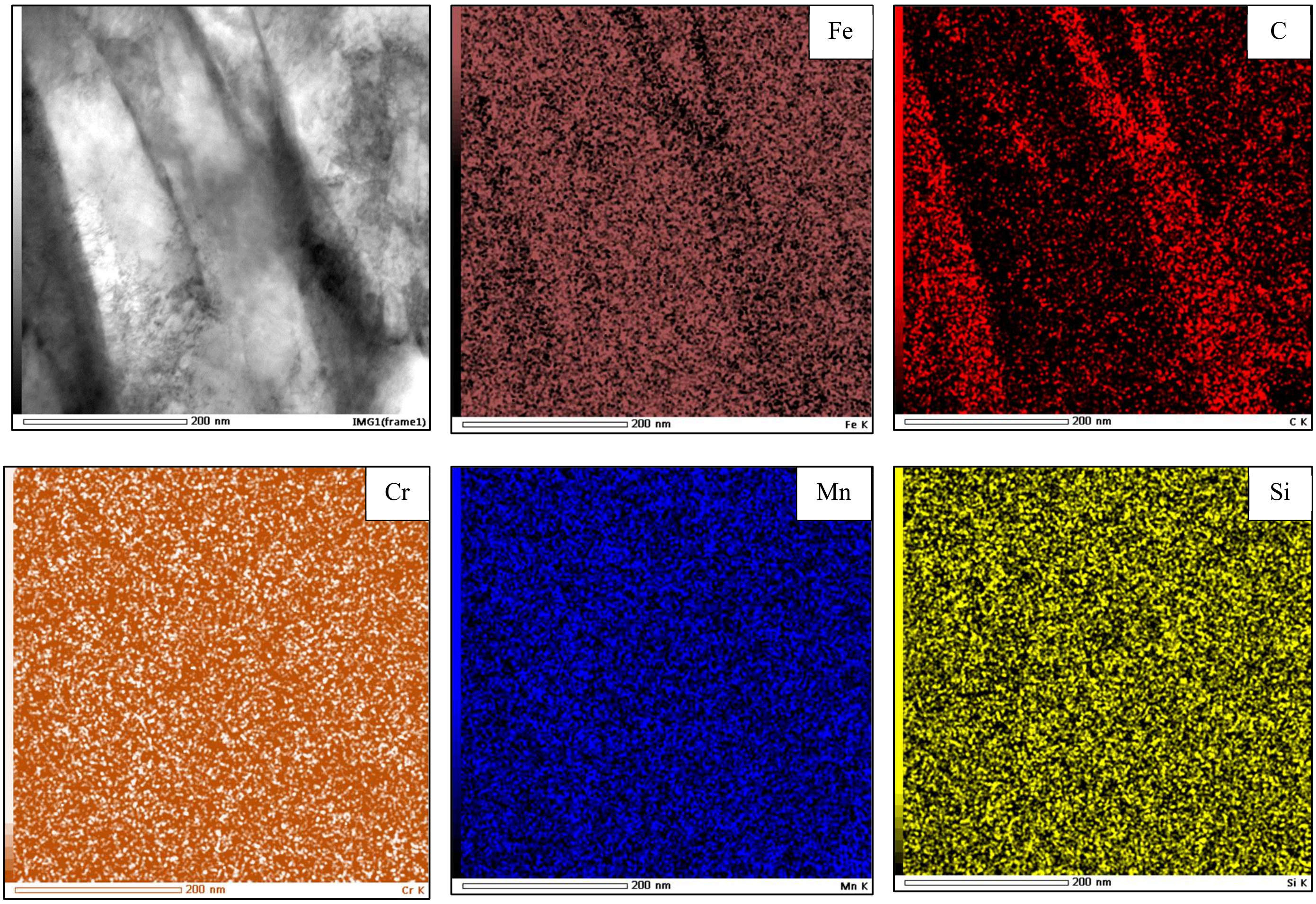

Figure 6.26: EDS quantified maps taken from (Top left) the bright field STEM image of BAIN 1 after tempering and deformation. Reading from left to right, the element maps are iron, carbon, chromium, manganese and silicon respectively.

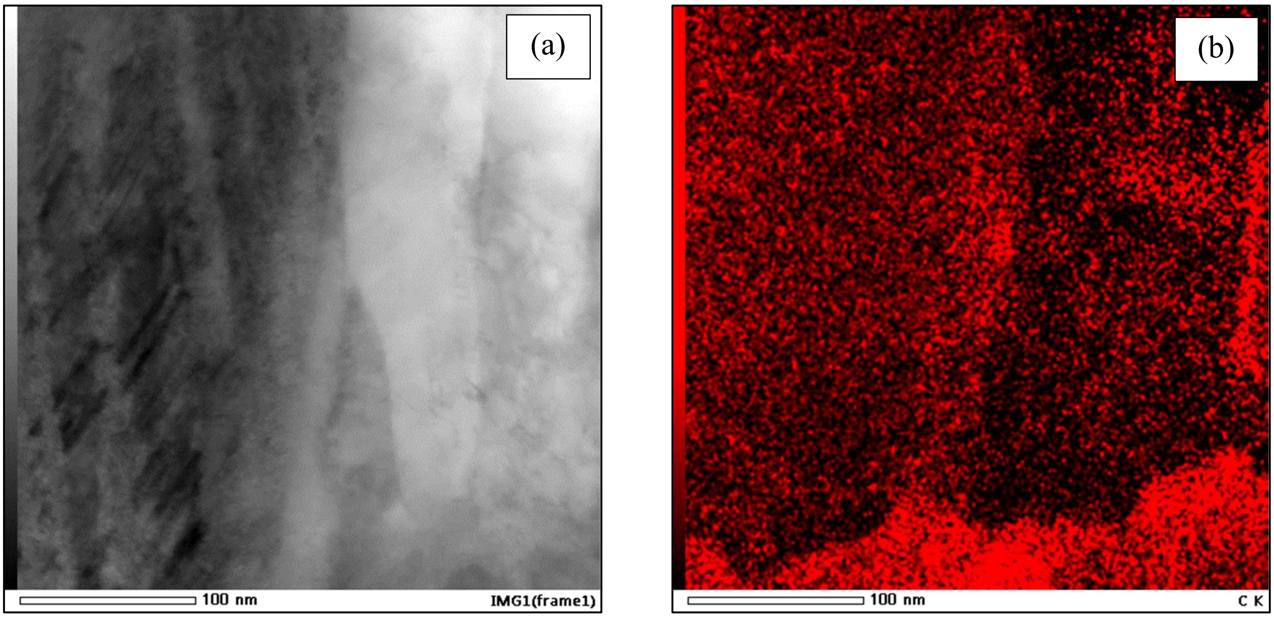

Figure 6.27: (a) Alternative bright field STEM image of BAIN 1 after tempering and deformation. (b) The corresponding EDS quantified map of the carbon distribution in the STEM image.

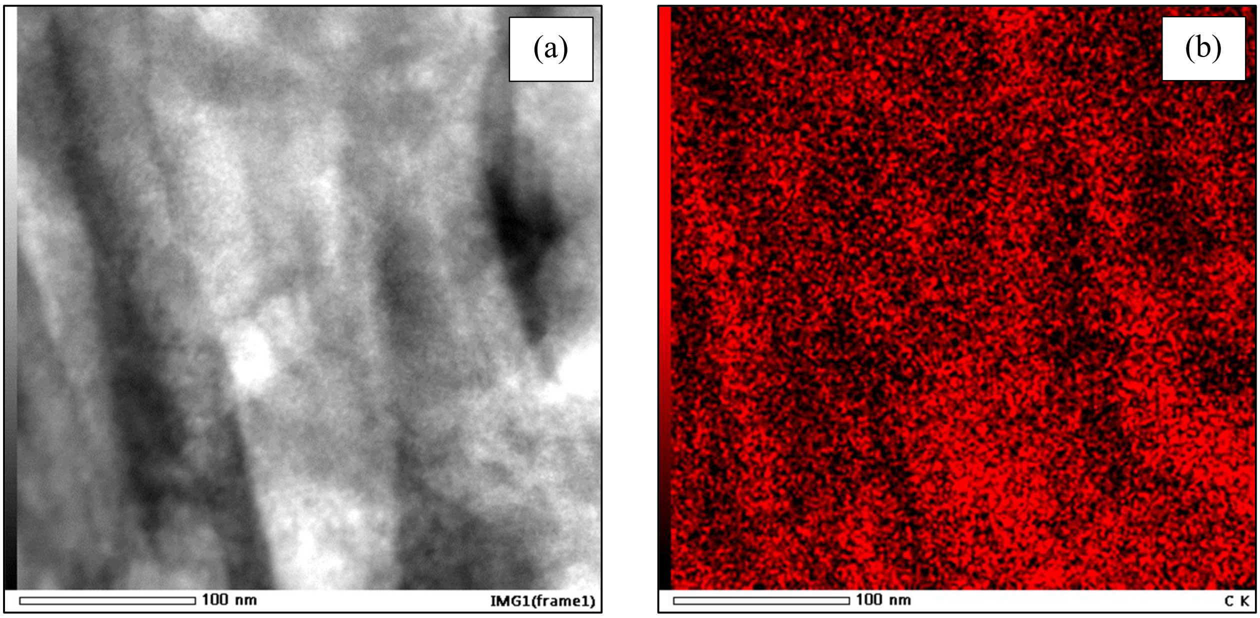

Figure 6.28: (a) Bright field STEM image of BAIN 2 after tempering and deformation. (b) Corresponding EDS quantified map of the carbon distribution in the STEM image.

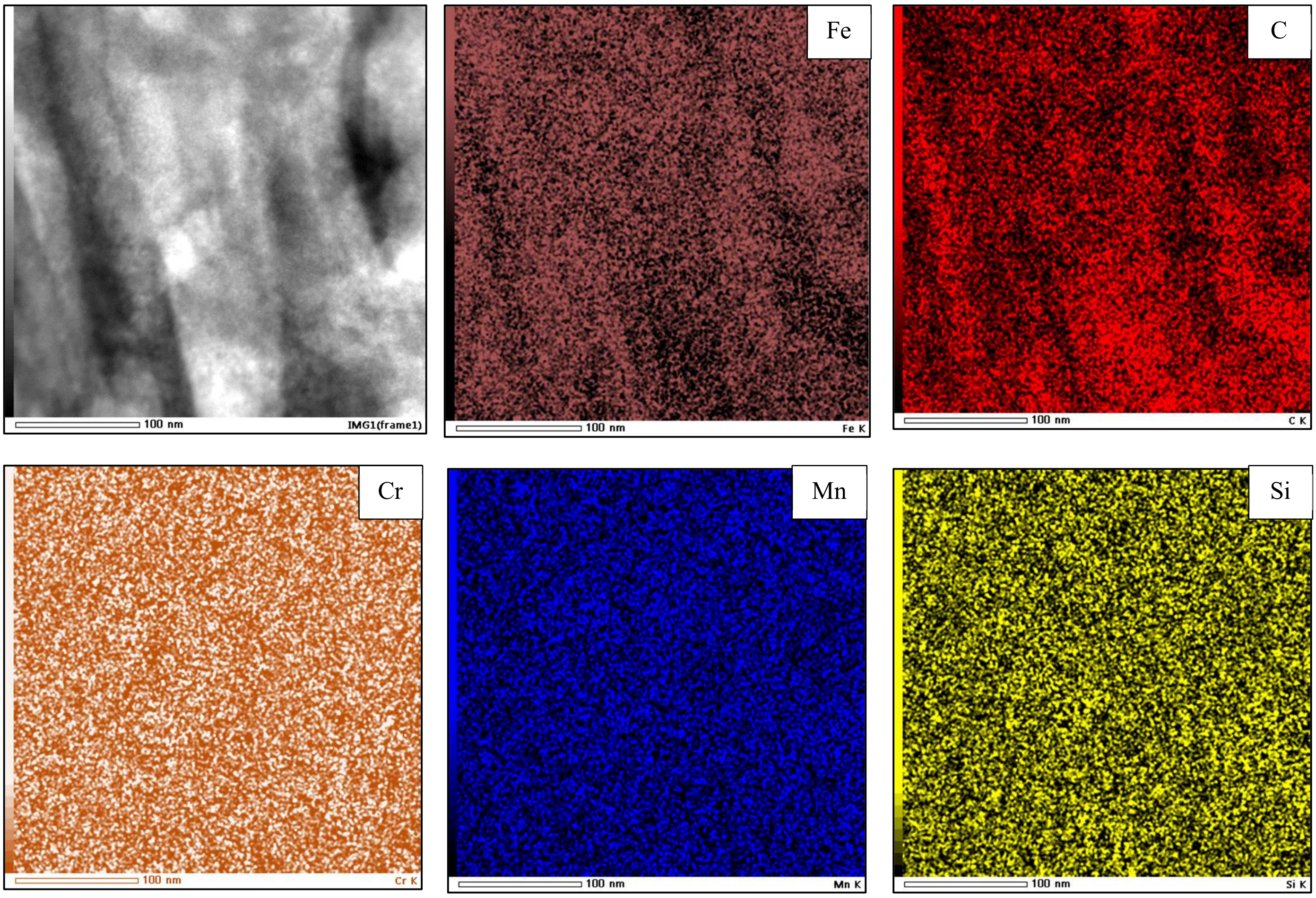

Figure 6.29: EDS quantified maps taken from (Top left) the bright field STEM image of BAIN 2 after tempering and deformation. Reading from left to right, the element maps are iron, carbon, chromium, manganese and silicon respectively.

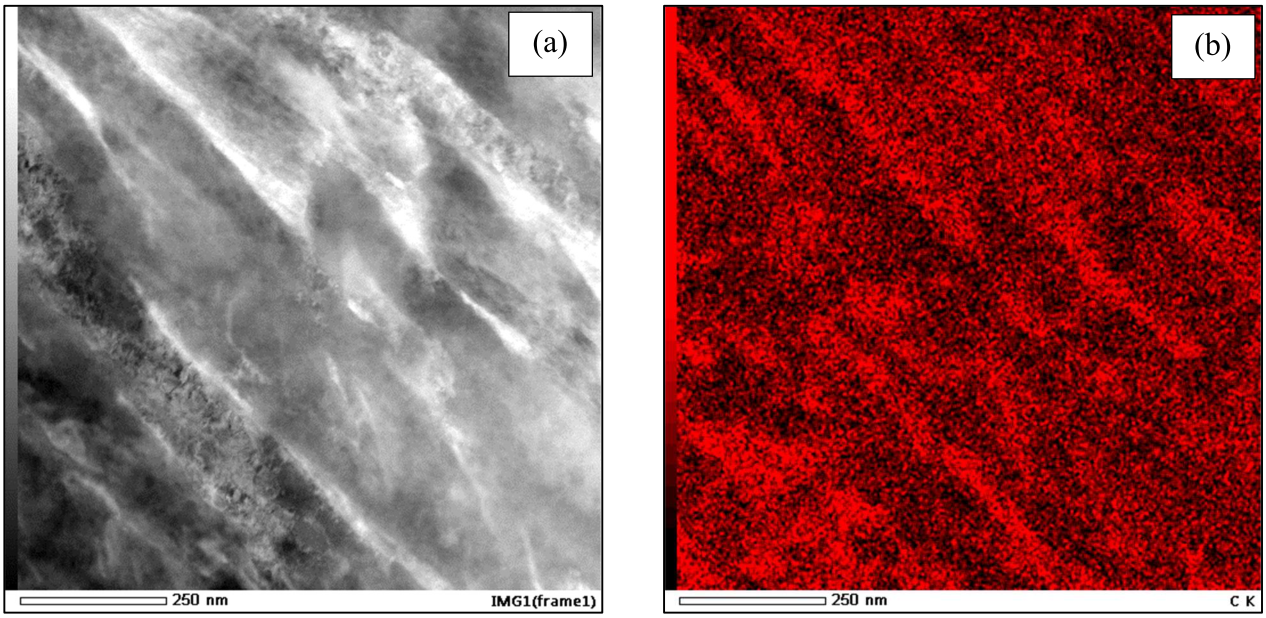

Figure 6.30: (a) Bright field STEM image of BAIN 3 after tempering and deformation. (b) Corresponding EDS quantified map of the carbon distribution in the STEM image.

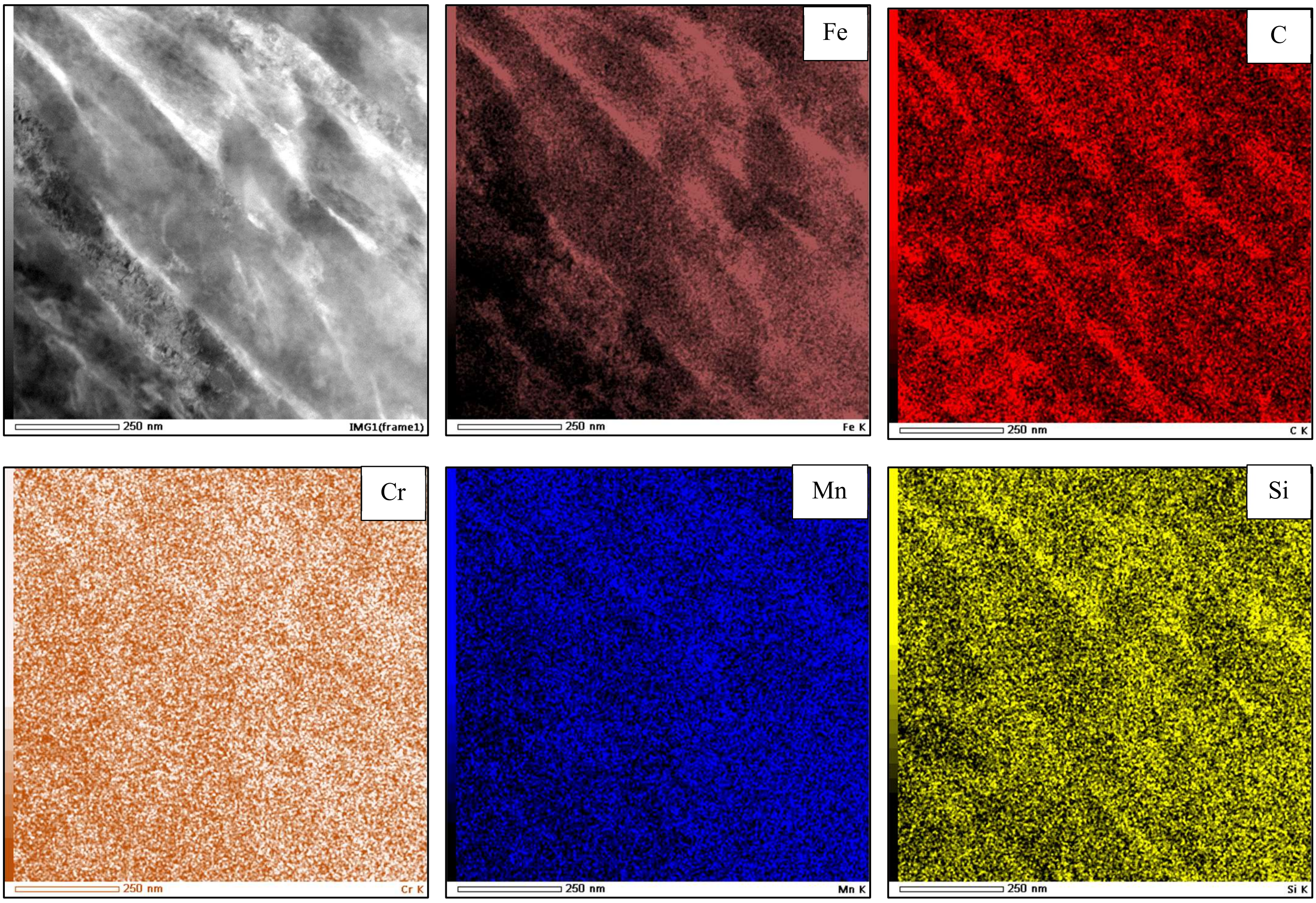

Figure 6.31: EDS quantified maps taken from (Top left) the bright field STEM image of BAIN 2 after tempering and deformation. Reading from left to right, the element maps are iron, carbon, chromium, manganese and silicon respectively.

6.2.5 EBSD/Grain distribution

Figures 6.32 to Figure 6.34 shows the EBSD results of both the tempered samples, and the tempered and deformed samples. Additionally, Figure 6.35 shows the evolution of the volume fraction and morphology of the retained austenite after each of the different processing stages.

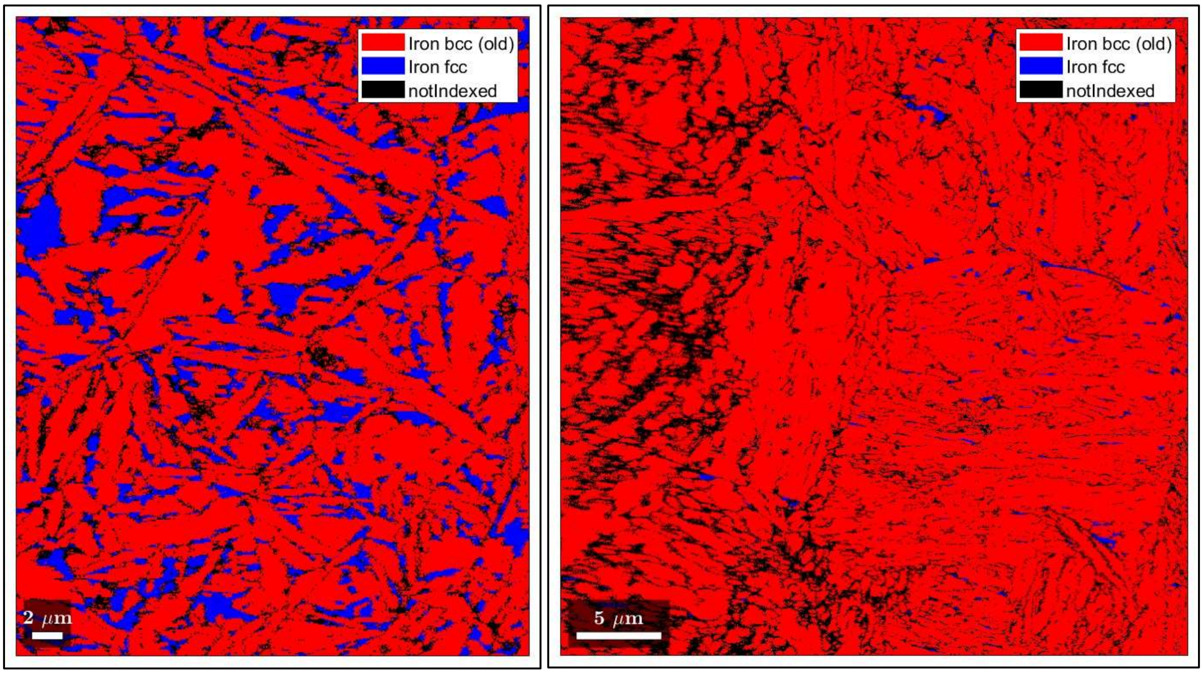

Figure 6.32: (left) EBSD image of BAIN 1 tempered. (right) EBSD images of BAIN 1 tempered and deformed (0.4 engineering strain).

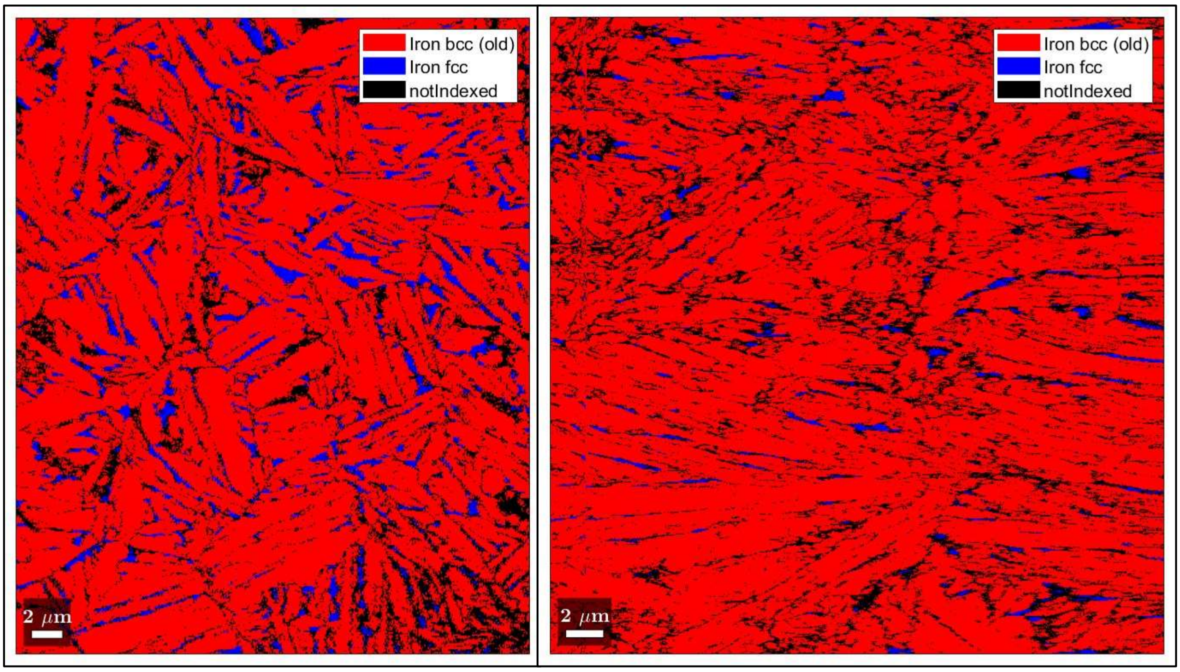

Figure 6.33: (left) EBSD image of BAIN 2 tempered. (right) EBSD images of BAIN 2 tempered and deformed (0.5 engineering strain).

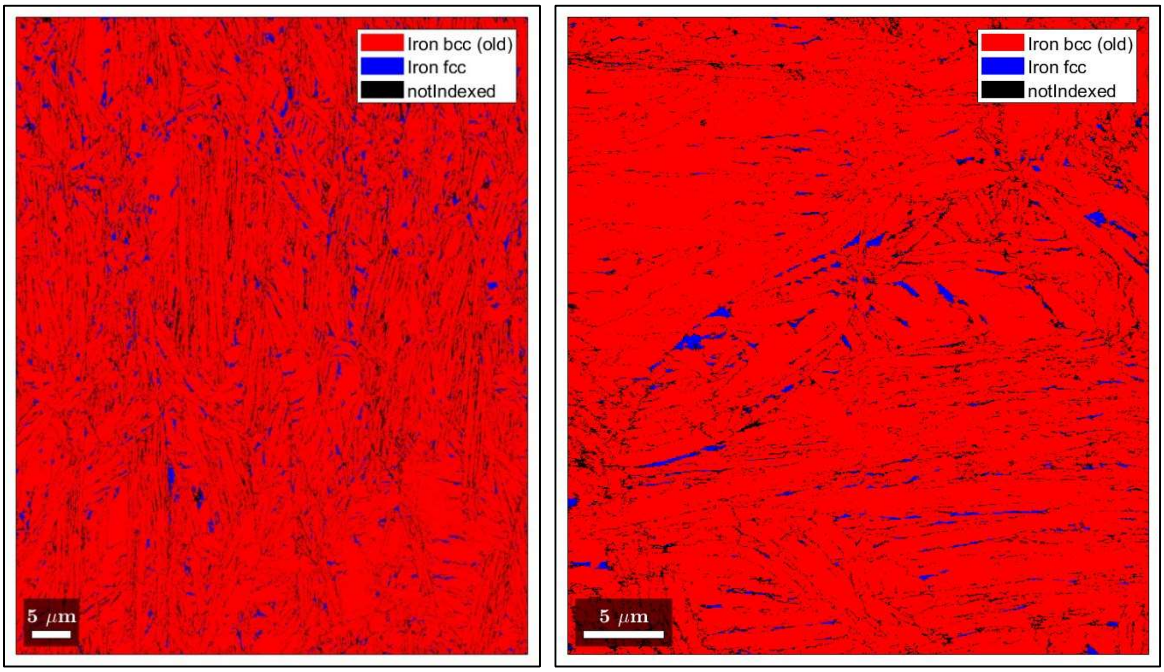

Figure 6.34: (left) EBSD image of BAIN 3 tempered. (right) EBSD images of BAIN 3 tempered and deformed (0.5 engineering strain).

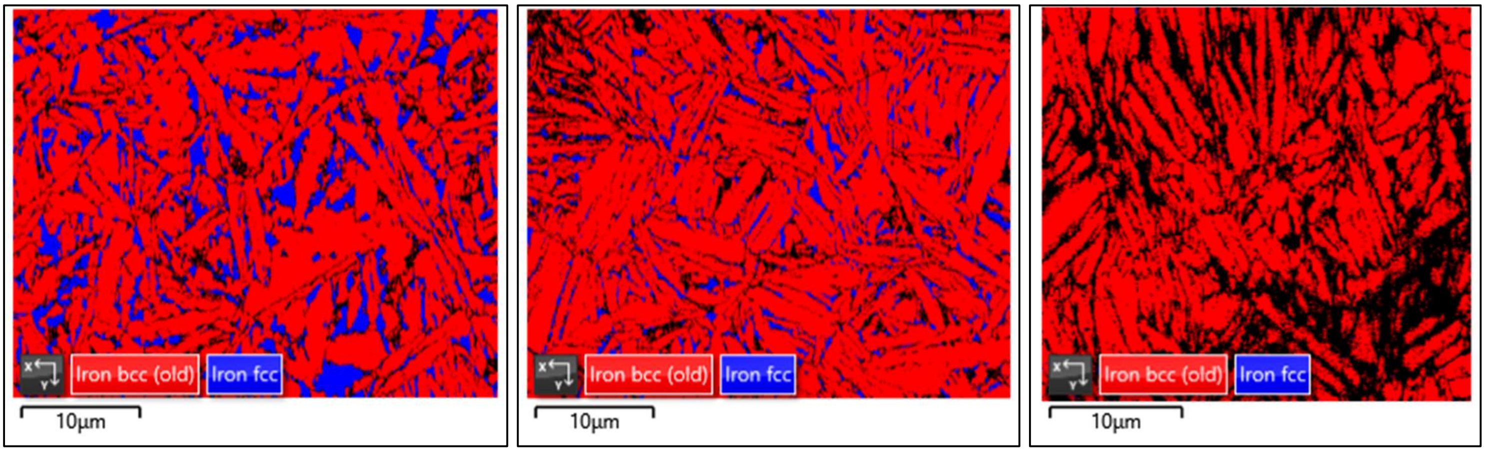

Figure 6.35: The evolution of the volume fraction of retained austenite in BAIN 2, shown using EBSD images. The EBSD maps are taken from the salt bath heat-treated state, the tempered state and the tempered and deformed state respectively.

Figures 6.36 to Figure 6.38 use the EBSD scan data created by AZTecCrystal software and utilised the MTEX program to produce graphs of the grain area of the retained austenite vs frequency, and the aspect ratio of the retained austenite vs frequency, for each of the tempered state compositions.

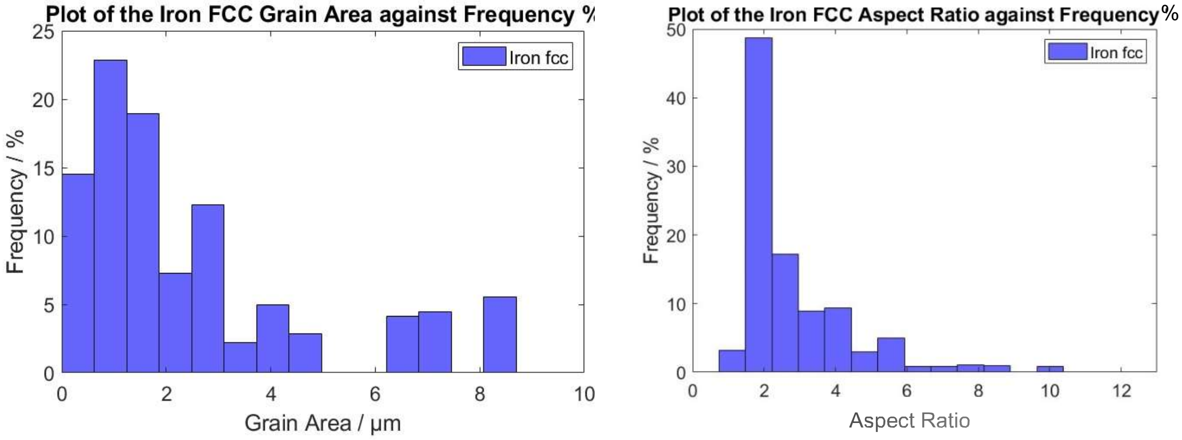

Figure 6.36: Plot of the (left) FCC grain area vs frequency and (right) FCC aspect ratio vs frequency for BAIN 1 Tempered.

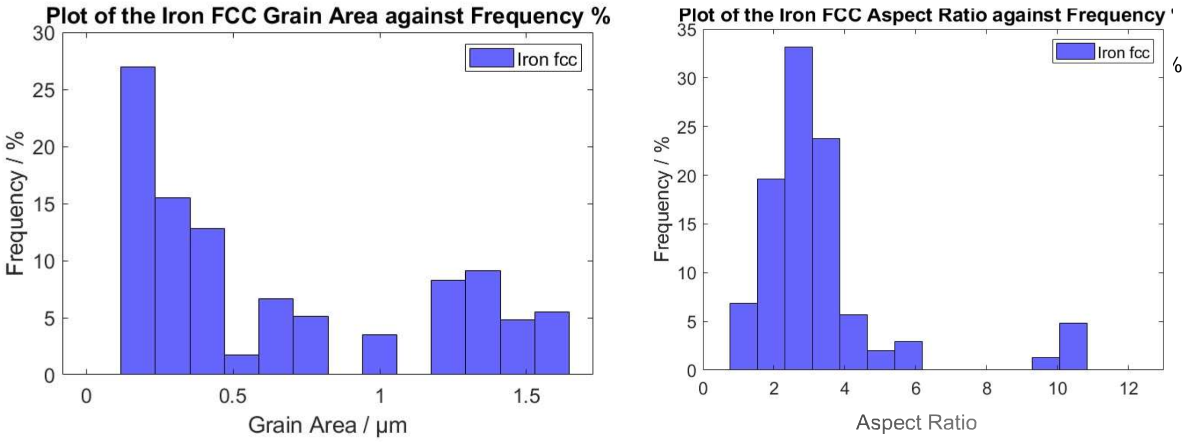

Figure 6.37: Plot of the (left) FCC grain area vs frequency and (right) FCC aspect ratio vs frequency for BAIN 2 Tempered.

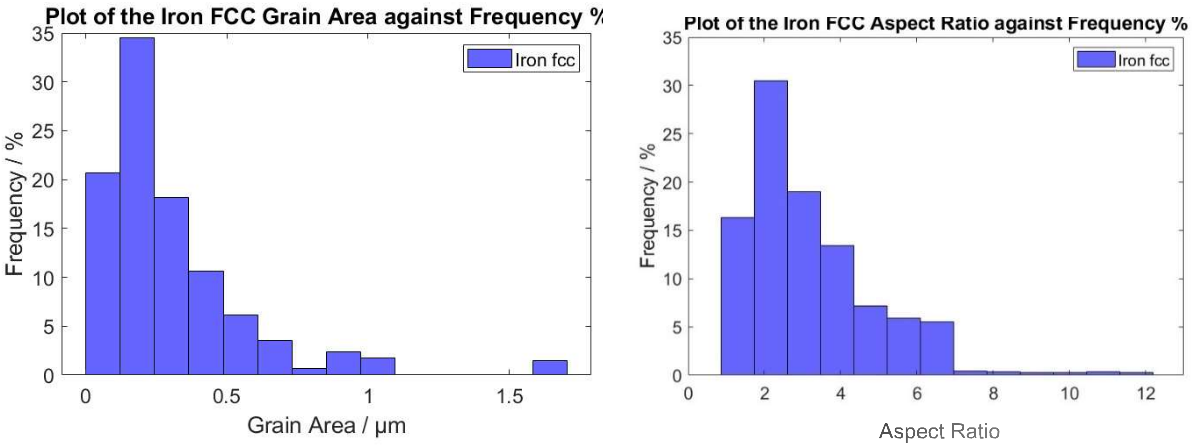

Figure 6.38: Plot of the (left) FCC grain area vs frequency and (right) FCC aspect ratio vs frequency for BAIN 3 Tempered.

6.2.6 XRD

Table 6.4 summarises the estimated fraction of retained austenite present in each of the alloy samples in both the salt bath heat treated and tempered condition. The XRD data plots can be found in the appendix, Section 9. Unfortunately, no XRD data was obtained for the deformed samples because of time constraints. The retained austenite was quantified using the RIR method, as discussed in Section 3.5.4.

Table 6.4: Summarised fraction of retained austenite detected using XRD, for each of the salt bath treated and tempered samples.

Alloy Name	**Est. wt.% RA**
BAIN 1 SB	22
BAIN 1 T	20
BAIN 2 SB	18
BAIN 2 T	16
BAIN 3 SB	18
BAIN 3 T	16

6.2.7 Mechanical testing

6.2.7.1 TMC Axial compression Testing

Figures 6.39 to Figure 6.41 show the stress strain curves for the salt bath treated samples, the tempered samples, and the combined stress-strain curves of both conditions respectively. As mentioned in Section 3, all the cold compression testing was performed using the TMC.

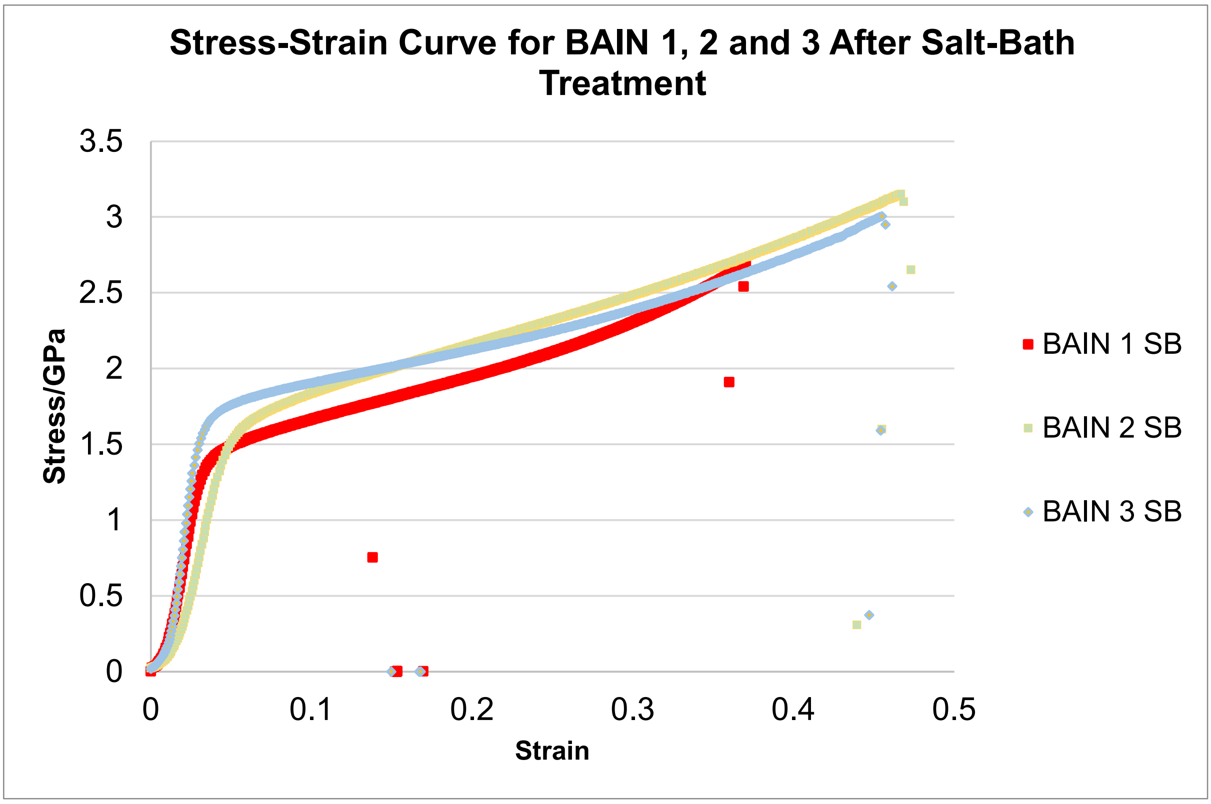

Figure 6.39: Stress-strain curve for BAIN 1, 2 and 3 after the salt-bath treatment.

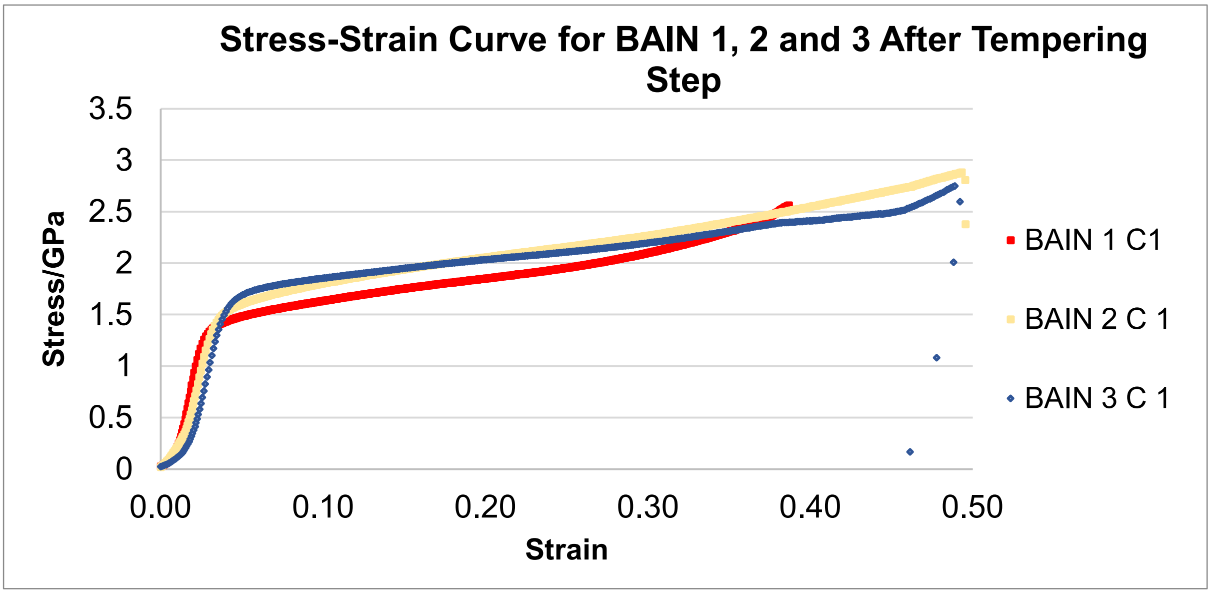

Figure 6.40: Stress-strain curve for BAIN 1, 2 and 3 after tempering.

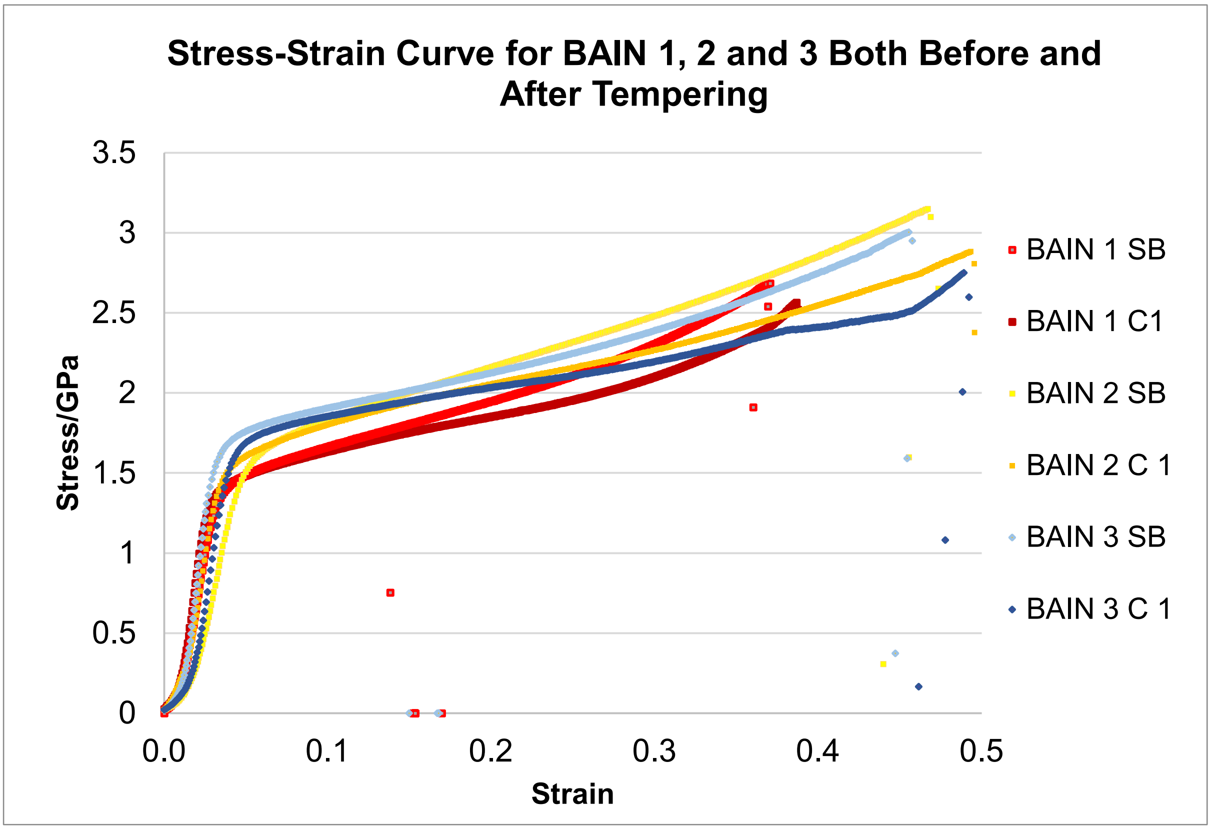

Figure 6.41: Stress-strain curve for BAIN 1, 2 and 3 both before and after tempering.

6.2.7.2 Vickers Hardness Testing

Finally, Figure 6.42 shows the Vickers hardness recorded for each of the alloy samples in all three conditions. The plot shows the average of 10 hardness readings taken per sample. The results from all the different hardness tests can be found in Appendix, 9.2.

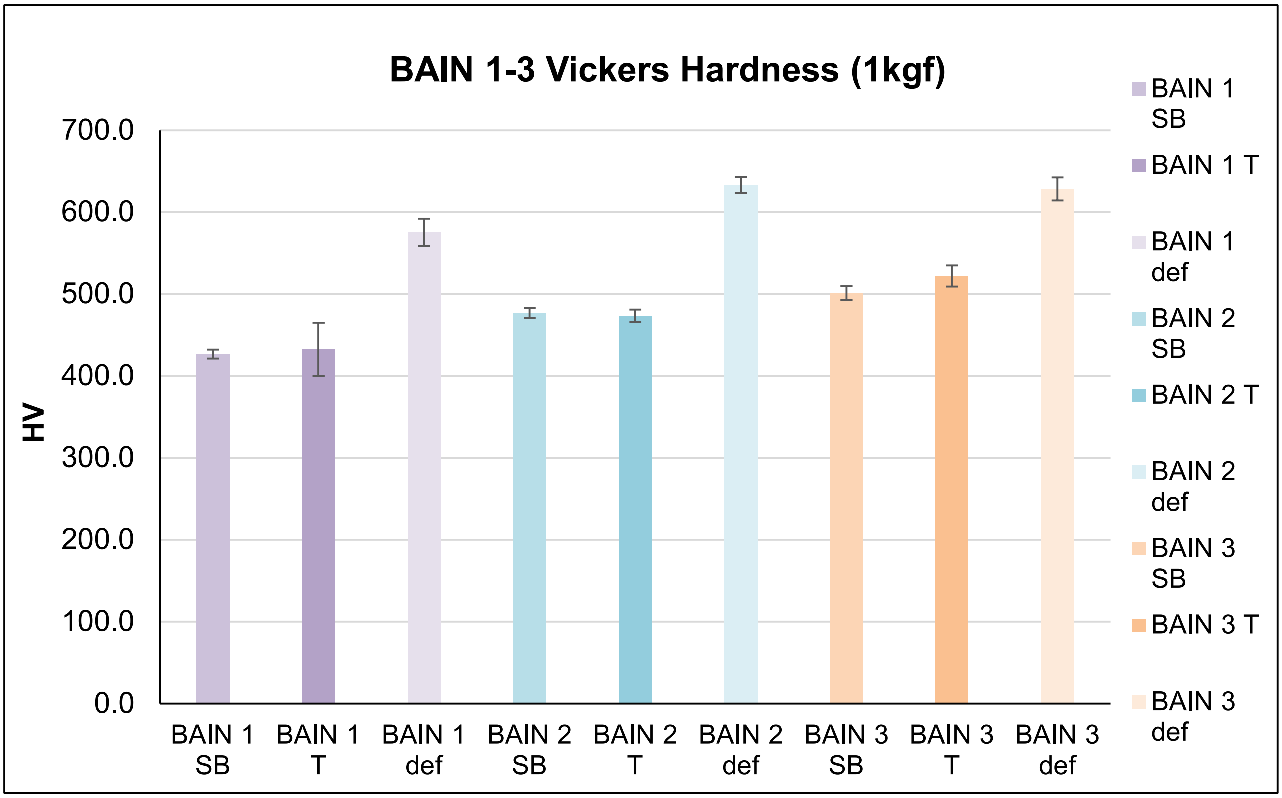

Figure 6.42: Vickers hardness average values from each of the different alloys and processing stages.

6.3 Discussion

6.3.1 SEM

The microstructures observed using SE-SEM do appear to indicate that the microstructures are indeed bainite with dispersed phases of retained austenite present. Figure 6.43 compares one of the microstructures to that achieved by Garcia-Mateo et al. [43] to show similarity between the bainitic microstructures.

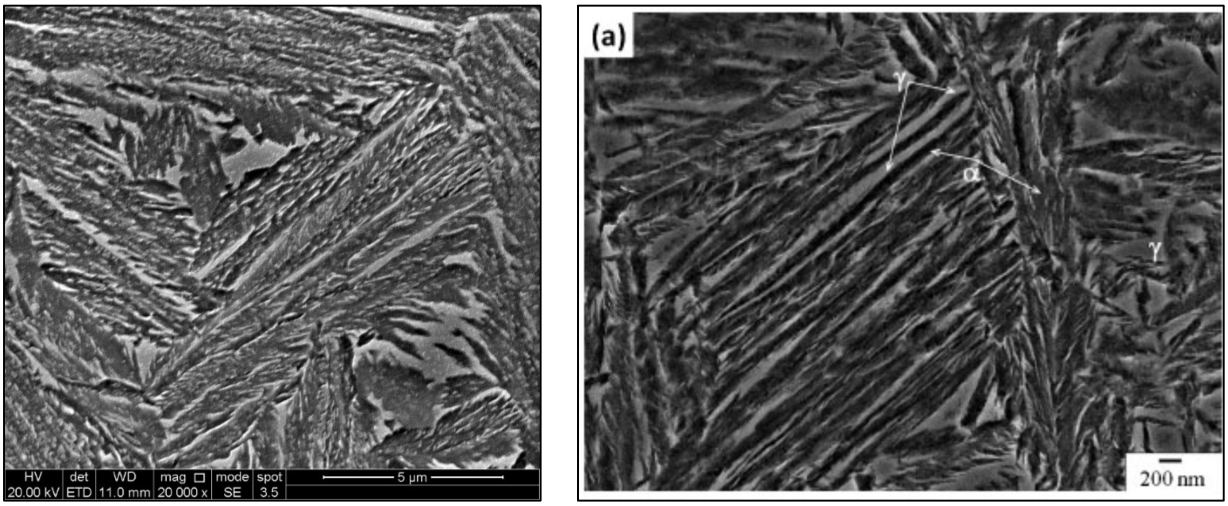

Figure 6.43: (Left) SE-SEM image of BAIN 3 after the 1^{st} isothermal holding treatment. (Right) Garcia-Mateo et al. examples of typical nanostructured bainite microstructure [43].

The retained austenite present is shown to be in two distinct morphologies, either as polygonal large blocks or as thin films within the matrix of bainitic ferrite. These two morphologies have been labelled in Figure 6.44 below. Additionally, there is no martensite that is distinguishable in the SE-SEM images, due to the retained austenite having a M_s temperature well below room temperature as the carbon has partitioned into the phase. The 2 wt.% silicon addition helps to facilitate this as this hinders the precipitation of carbides, therefore more carbon is present to stabilise the retained austenite.

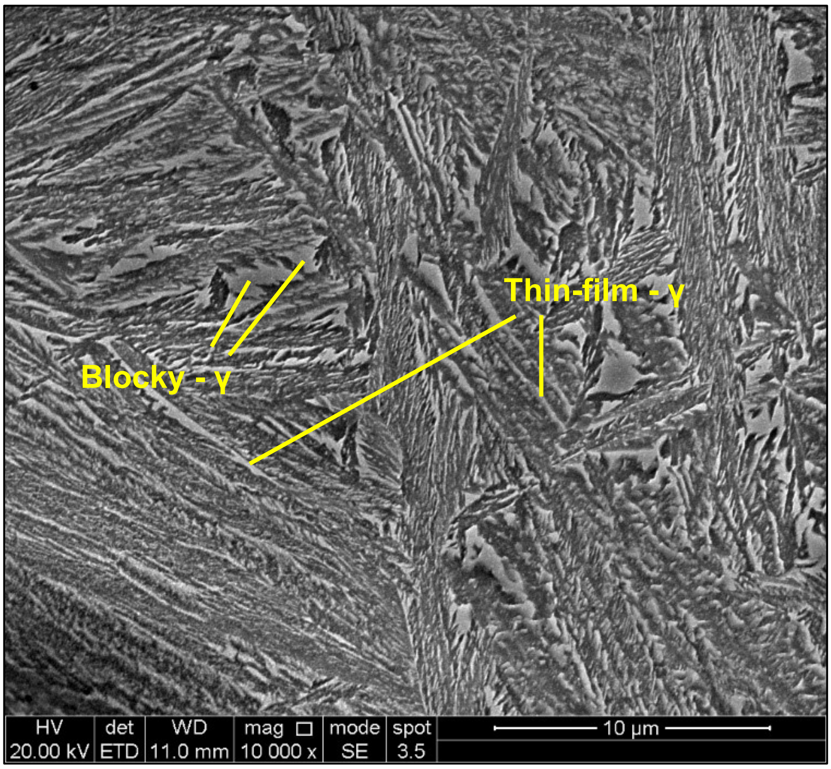

Figure 6.44: SE-SEM of BAIN 3 after 1st isothermal holding treatment. Thin-film and blocky retained austenite are labelled above.

Though it is difficult to resolve the coarseness of the bainitic ferrite in the multiple images, it can be observed that BAIN 3 appears to have the finest microstructure. This is most clearly seen in the after the initial heat treatment, in Figure 6.7 (a). However, this is not a quantifiable result. Further experimental work would be needed to measure the size of the phases present more accurately. One explanation for the qualitative finding, is the higher carbon content in BAIN 3, at 0.5 wt.%, as compared to BAIN 1 and 2, at 0.4 wt.%. BAIN 1 and 3 have the same chromium and manganese content, thus the higher carbon present in BAIN 3 results in the M_s temperature of the alloy being 50 °C lower. This allows for a lower transformation temperature heat treatment, producing the finer microstructure in the process as grain growth during transformation is more limited. Comparing the compositions of BAIN 2 and BAIN 3 is more nuanced as the M_s temperatures between the two alloys are much more similar. The lower manganese and chromium content in BAIN 3 could results in a faster bainitic transformation, allowing for a larger volume fraction of bainitic ferrite to be formed under the isothermal holding temperature and time. As previously mentioned, Caballero et al. [36] found that reducing the addition of Mn and Cr helped to decrease transformation times substantially. This must be quantified through later experiments, such as XRD and EBSD.

The second isothermal holding heat treatment does appear to refine the microstructures for each of BAIN 1, 2 and 3. The amount of blocky polygonal retained austenite decreases between the SE-SEM. This is likely due to the phases transforming into bainitic ferrite during the additional heat treatment. Avishan et al. [49] found that two step austempering not only decreased the overall volume fraction of retained austenite but also, had the additional benefit of producing a second generation bainite within the microstructure. Figure 6.45 compares the second generation bainite observed in Avishan's work with the SE-SEM images of one of the bainitic microstructures produced through this work. The formation of a second generation bainite within the microstructure is not as obvious but plausible in the region highlighted.

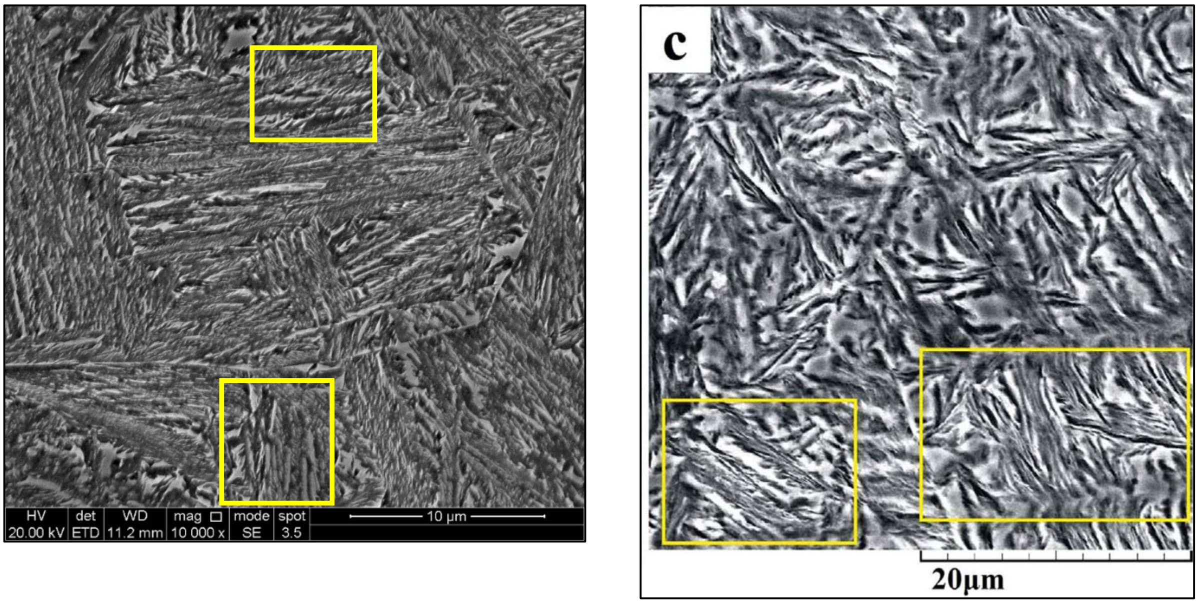

Figure 6.45: (Left) SE-SEM image of BAIN 3 after the tempering step, with highlighted regions being suggested for the formation of second generation bainite. (Right) SE-SEM image from Avishan et al. where the rectangular sectors suggest the formation of second generation bainite upon a second isothermal holding step [49].

TEM and STEM will also help to differentiate whether any of the retained austenite phase has transformed, into either martensite or a second generation bainite. Figure 6.46 compares how present the phase is in the microstructure before and after the step.

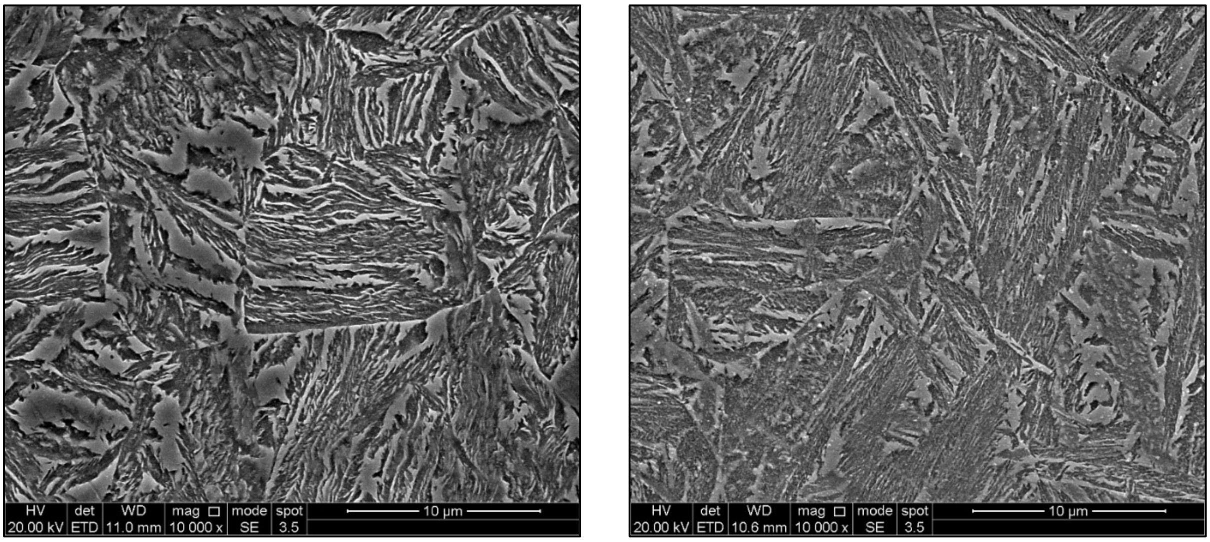

Figure 6.46: SE-SEM images of BAIN 2 (left) before the tempering step and (right) after the tempering step.

Post deformation, it can be observed that a large amount of the retained austenite left in the microstructure resembles the thin film morphology. However, large blocky regions of austenite still exist, as observed in Figure 96 above (right image). It is difficult to resolve whether any untempered martensite has formed during deformation. This could indicate that the level of deformation was not large enough to observe this effect. The TMC is limited to compressing to 50% of the original height (0.7 true strain). Therefore, all the samples were to be compressed to an engineering strain of 0.5. This is true for the BAIN 2 and BAIN 3 samples, however, an error when programming the TMC caused the BAIN 1 samples to be compressed to an engineering strain of only 0.4.

The SE-SEM microstructures do not confirm the presence of carbides within the samples. It has been proposed that carbides could be observed in Figure 6.47, as shown below. However, the phases labelled could similarly be retained austenite or a foreign particle present on the sample surface. The formation of carbides should be suppressed by the 2 wt.% addition of silicon present. However, at the scale shown in the images, it is difficult to resolve. The carbide presence or lack thereof should be clearer in TEM and STEM images, at higher imaging magnifications.

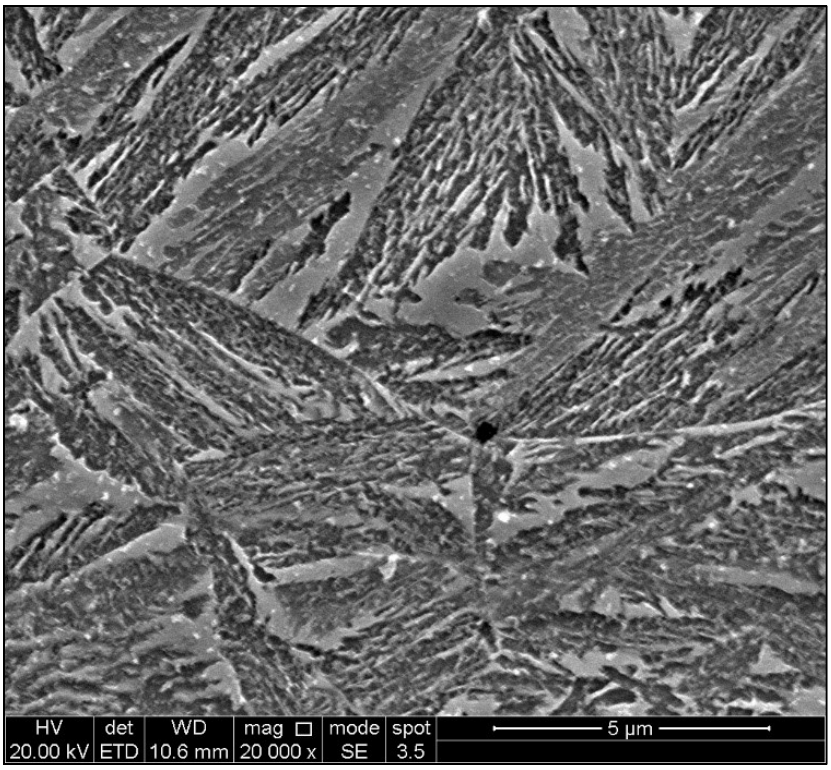

Figure 6.47: SE-SEM image of BAIN 2 after the tempering step.

6.3.2 TEM, STEM and EDS

Once again the TEM images closely resemble the NANOBAIN microstructures that were observed by Caballero et al [35]. Figure 6.48 compares the two microstructures. As shown, the microstructures mainly consist of thin film austenite in between a matrix of bainitic ferrite.

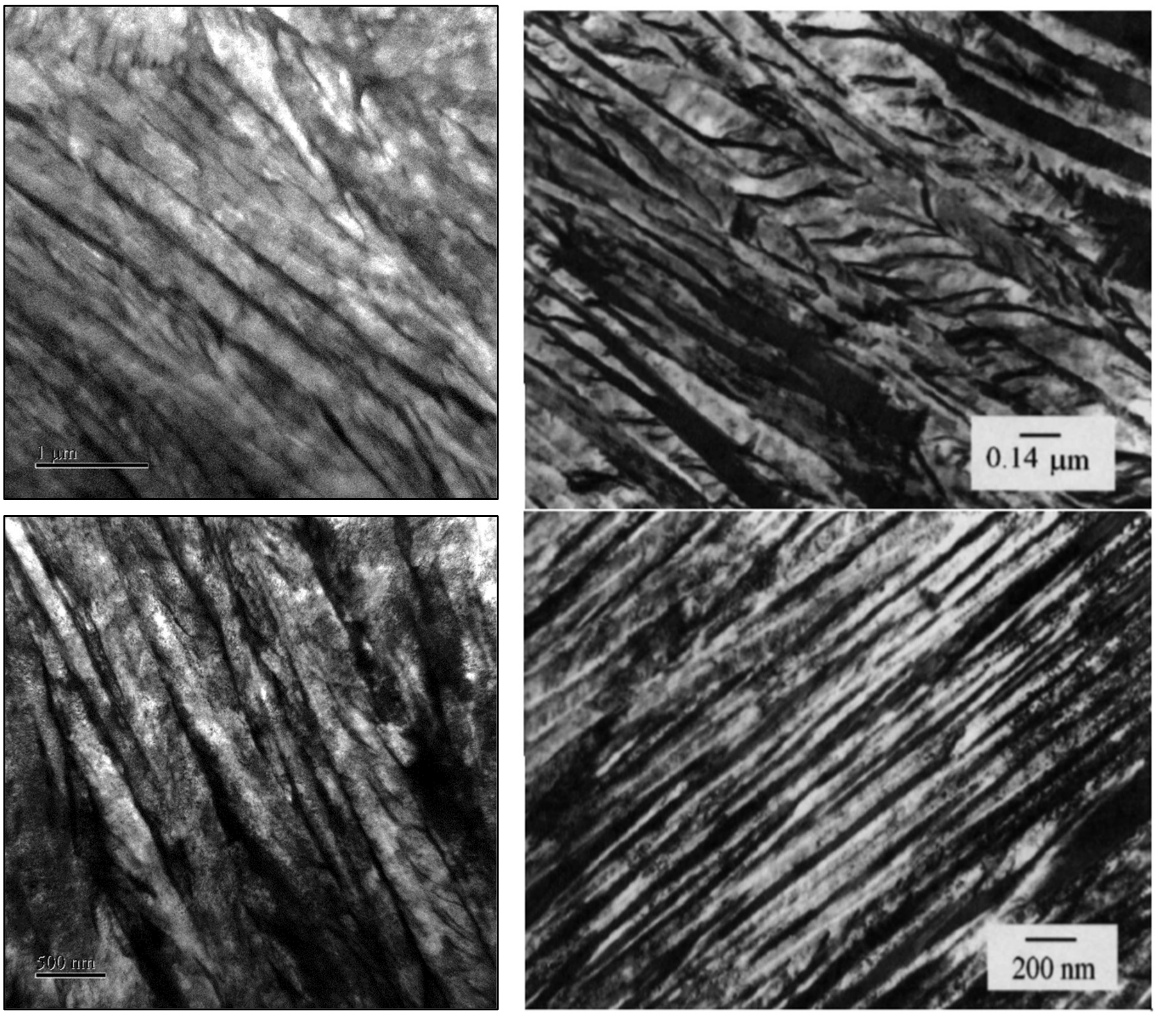

Figure 6.48: (Left) Two TEM images of BAIN 1 showing the microstructure of thin filmed retained austenite and bainitic sheaves. (Right) TEM images of the microstructures developed by Caballero et al [35].

The images are consistent with nanostructured bainite, with thin sheaves of bainitic ferrite separated by thin film retained austenite. Comparing TEM images obtained from BAIN 2 with the TEM images obtained by Caballero et al. [35], the similarities between the microstructures are evident and the same patterned effect of the retained austenite can be observed. The composition used by Caballero et al. consisted of Fe -1.59Si - 1.94Mn - 1.33Cr - 0.30Mo - 0.02Ni - 0.11V and carbon, however, the exact wt.% of the addition is not specified.

Through diffraction patterns, it can be confirmed that the thin film phases present in microstructures are indeed retained austenite. The d-spacing can be calculated by measuring the spacing between the spots in the selected area diffraction pattern. By then using Bragg's law, Equation 11, the lattice parameter can be compared to the XRD lattice parameter of austenite. The angle between spacings additionally can be used to determine the zone axis of the pattern, using the selected area diffraction pattern (SADP) image in Figure 6.49 from V. E. Cosslet's book, Practical Electron Microscopy [76]. This can be compared with the diffraction pattern show in Figure 6.50.

$$n\lambda = 2d\sin\theta \tag{11}$$

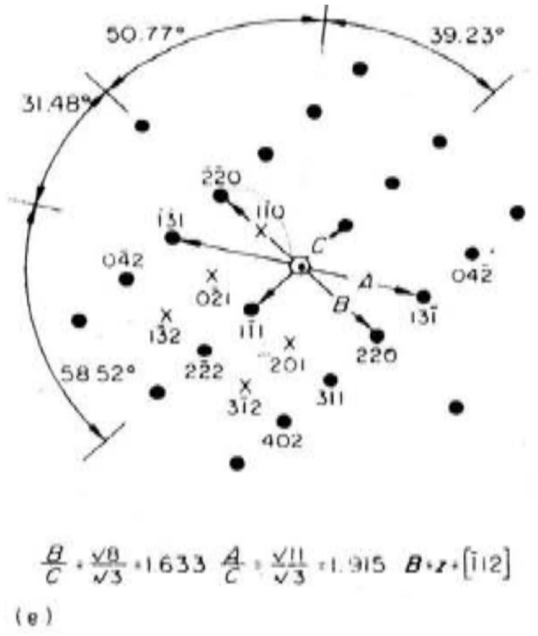

Figure 6.49: Single crystal spot transmission electron diffraction pattern for the FCC crystal structure, where z is the zone axis and equals [112]. Taken from [76].

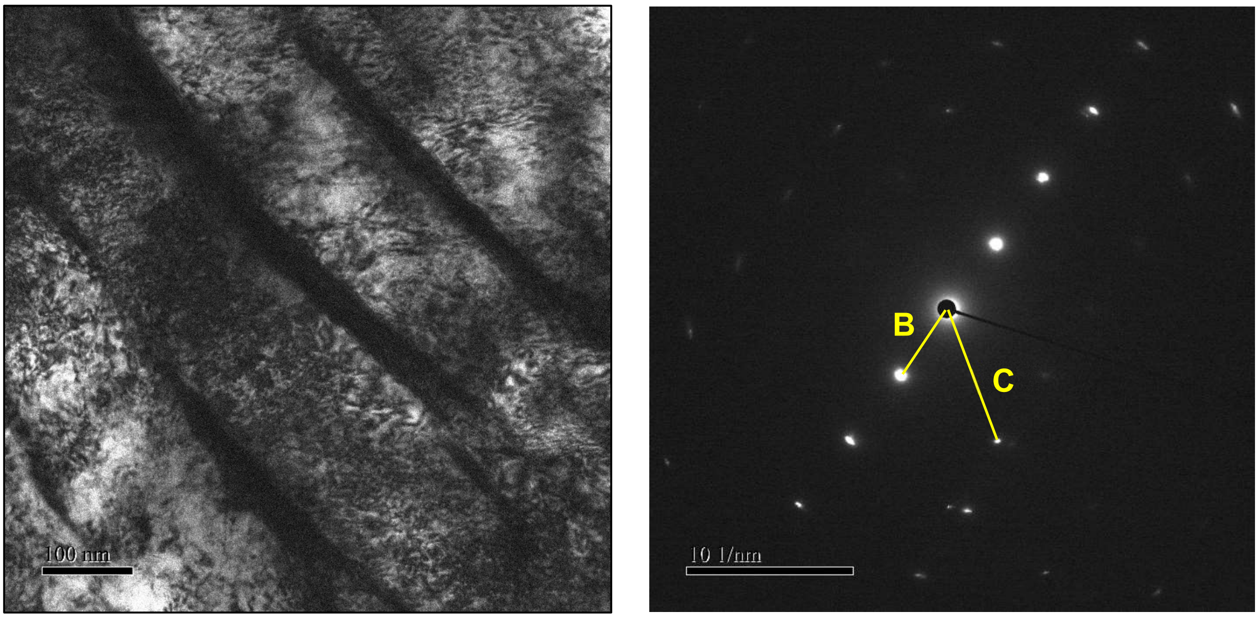

Figure 6.50: (Left) TEM image of BAIN 1 after being tempered and deformed and (right) the corrosponding diffraction pattern produced by focusing on the dark thin film regions.

Comparing the value of the calculated austenite d-spacing from the diffraction pattern and that of the XRD austenite d-spacing, the two values are 2.03 Å and 2.05 Å respectively. It is evident that the phase of the selected area diffraction pattern is austenite. This confirms that the phase is present, and the darker banded regions of the TEM/STEM images are in fact stabilised retained austenite. By comparing the angles between the diffraction spots with the SADP image, it can be observed that the zone axis of the phase is the [112] plane.

The carbide free microstructure is a good indication that the carbon has successfully diffused and stabilised the retained austenite present. However, there is signs that the larger retained austenite blocks have undergone the TRIP effect to form martensite, as shown in Figure 6.51. The microstructure formed is similar to that found by Sandvik et al. [40], however, the samples in that study were deformed to fracture under tensile testing and contained a larger addition of carbon at 0.76 wt.%. Nonetheless, this indicates that some of the retained austenite in the samples from the EngD project had transformed into martensite in the samples, even prior to deformation.

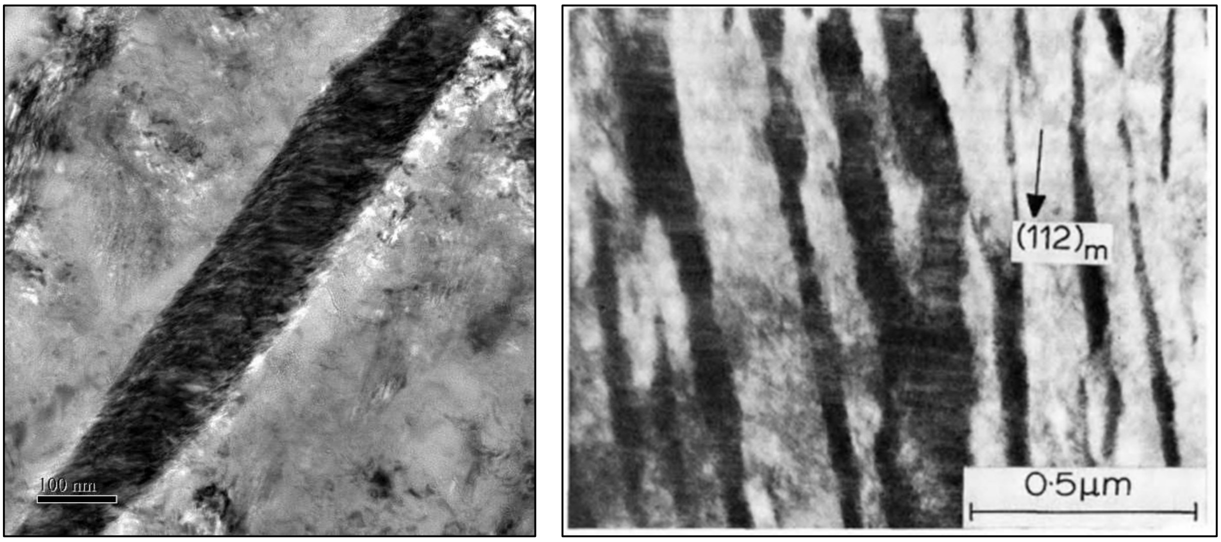

Figure 6.51: (Left) TEM image of BAIN 1 after the tempering step and (right) deformation induced twinned martensite found in nanostructured bainite by Sandvik et al [40].

The TEM thin disc samples formed an oxide film very quickly between electropolishing and as such, STEM was found beneficial to observing the microstructures in more detail. EDS analysis was performed on STEM images of the retained austenite, to observe the distribution of elements within the microstructure. It can be observed in Figure 6.52 that the carbon is diffusing into the retained austenite as expected, stabilising the phase.

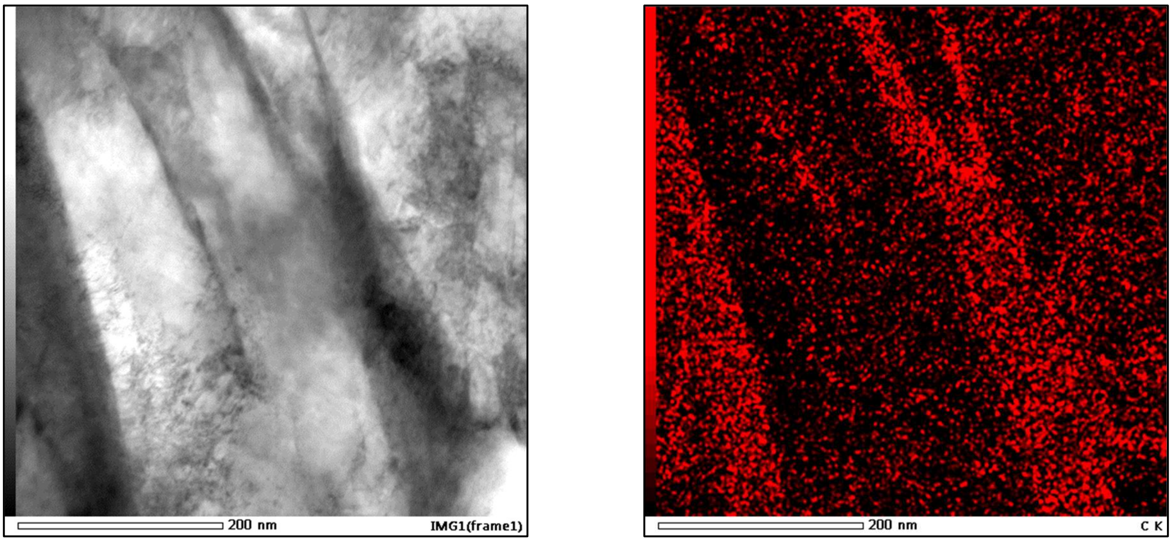

Figure 6.52: (Left) Bright field STEM image of BAIN 1 after tempering and deformation. (Right) Corresponding EDS map of the carbon distribution in the STEM image.

The isothermal heat treatment was designed to partition the carbon into the retained austenite, due to the higher solubility of carbon in austenite than ferrite. By transforming at temperatures only slightly above the M_s temperature, other elements are not diffused in addition and the fine microstructure helps to shorten diffusion distances. The silicon addition prevents the formation of carbides, which would compete with the diffusion into the retained austenite and result in less carbon available to stabilise. Point analysis of the mapped regions shows that mass% of carbon is higher than that of surrounding ferrite. This can be observed in Figure 6.25 (a) where the mass% of carbon measured in the austenite is 3.35 compared to the 1.91 value of the bainitic ferrite region. The EDS map shown in Figure 6.53 suggests that some of the other alloy elements are diffusing into the retained austenite. However, by looking at the Fe image, this is likely an issue with the scan. This is clearer when comparing the Fe image to that of the other scans.

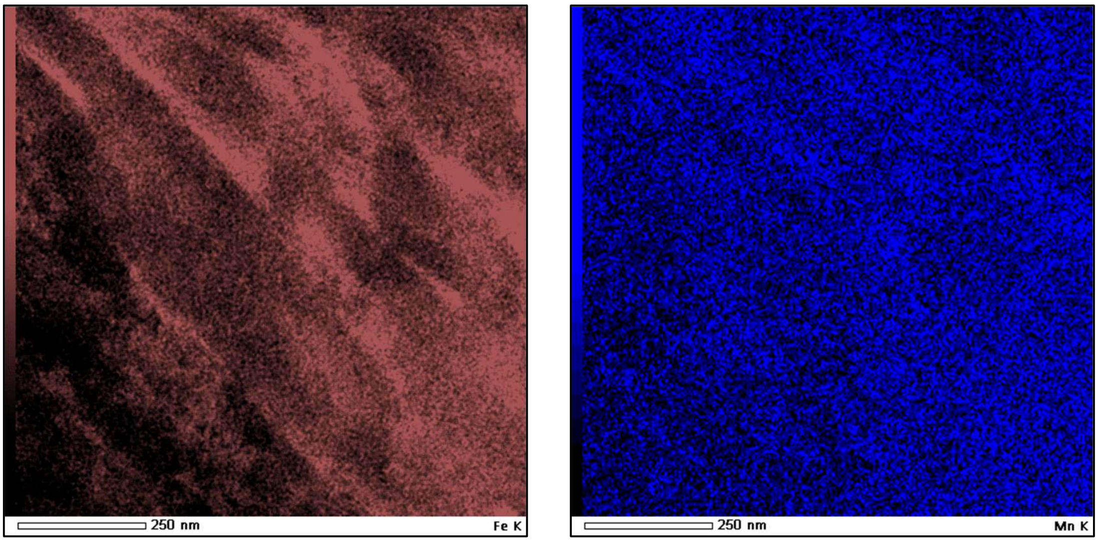

Figure 6.53: EDS maps of iron and manganese in BAIN 2 after tempering and deformation.

6.3.3 EBSD and XRD

The EBSD phase maps of the 1st step heat treated, 2nd step heat treated and deformed samples is beneficial in showing the evolution of the volume of retained austenite. These 3 different sample condition phase maps for BAIN 2 are displayed below in Figure 6.54.

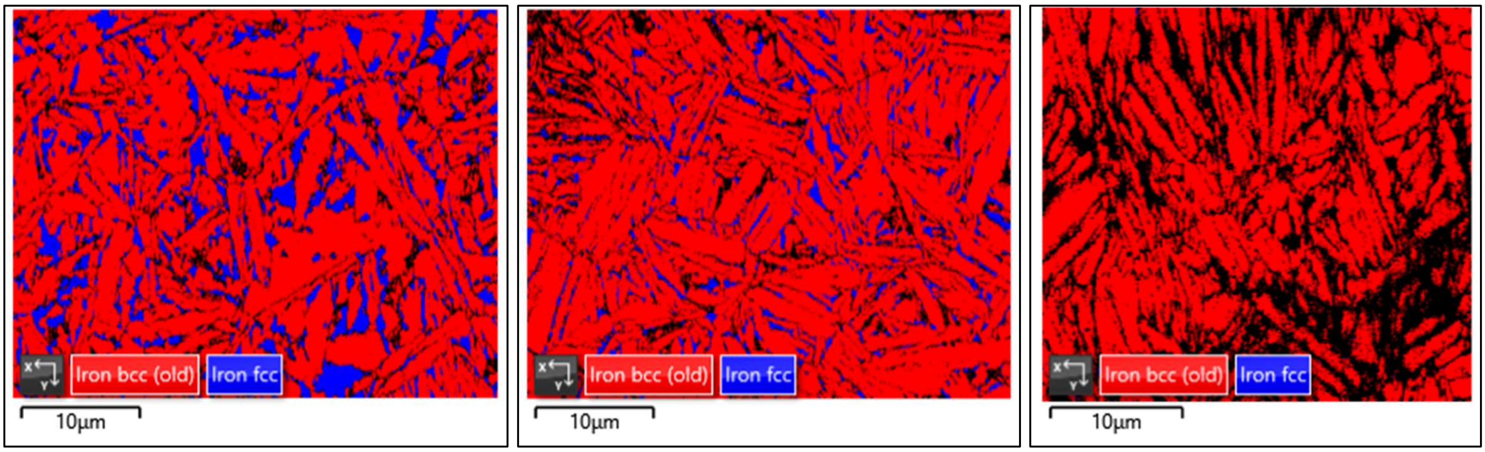

Figure 6.54: The evolution of the volume fraction of retained austenite in BAIN 2, shown using EBSD images. The EBSD maps are taken from the salt bath heat-treated state, the tempered state and the tempered and deformed state respectively.

This correlates with the detected volume fractions of Iron FCC (austenite) that the different maps produced, where the detected fraction of the 3 different conditions as listed previously are 13.16, 5.87 and 0.09 volume fraction percent respectively. The dislocations present in the deformed samples make it very difficult to map. This inability to index certain regions is the clearly observed in the deformed sample for BAIN 2. Therefore, it is important to consider that the volume fraction of retained austenite in the deformed samples is likely higher than indicated by EBSD. The decrease in the volume fraction of austenite is a sign that the retained austenite is transforming during before processes, whether that is into bainitic ferrite or martensite due to the TRIP effect.

In the tempered condition, BAIN 3 has the lowest amount of retained austenite detected during the EBSD scan, following BAIN 2, with BAIN 1 having the highest volume fraction of retained austenite. Figure 6.55 compares the 3 tempered alloy EBSD phase maps and displays the estimated fraction of Iron FCC. BAIN 1 T containing a relatively large amount of the phase is likely due to the higher M_s temperature of the BAIN 1 compositions, leading to a higher transformation temperature required. As mentioned in Section 6.1, to produce a fine microstructure, it is essential for the transformation temperature to be a low as possible. In turn, the finer retained austenite allows for shorter distances for carbon to diffuse into the phase, further stabilising the phase at room temperature. However, BAIN 2 and BAIN 3 had the same transformation temperature. The lower fraction of retained austenite in BAIN 3 could be cause by the lower chromium and manganese content when compared to BAIN 2. By reducing the two additions, the aim was to increase the kinetics of transformation to bainite in the same amount of time.

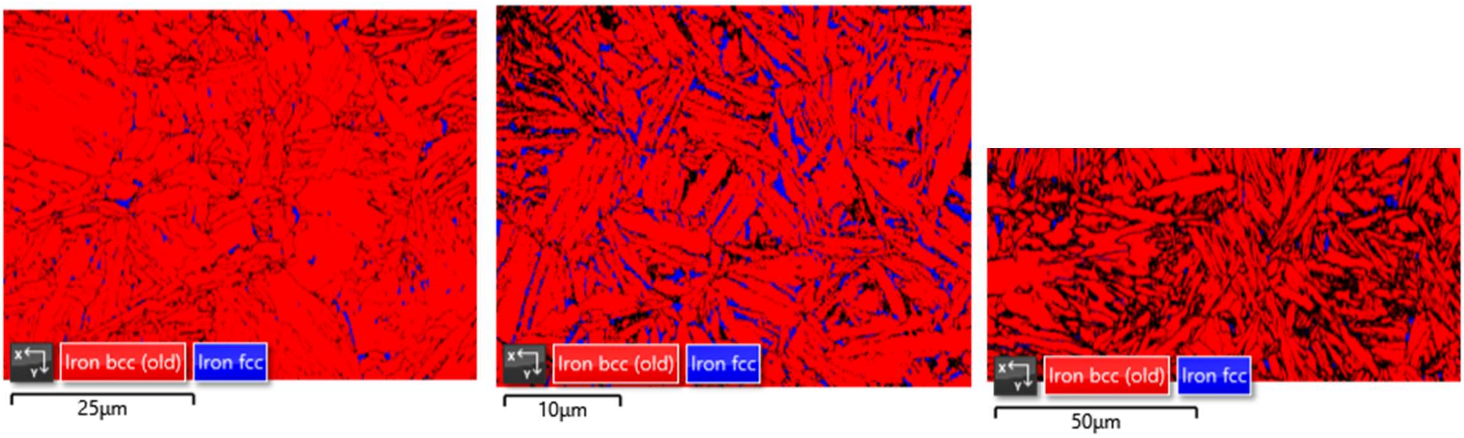

Figure 6.55: The EBSD maps of BAIN 1 tempered, BAIN 2 tempered and BAIN 3 tempered respectively.

While the fraction of retained austenite is important, as a larger volume fraction of bainitic ferrite leads to better tensile strengths, the morphology of the retained austenite present is another key factor of the mechanical properties of nanostructured bainites. The surrounding bainitic ferrite constrains the transformation. To compare the morphology of the 3 different alloy samples, Figure 6.56 and Figure 6.57 were produced using AZTecCrystal, a program that reads the .ctf files produced during EBSD and open them in coding programs such as MATLAB. The file produces a matrix of each scanned point, and the program allows for grain sizes and aspect ratio of the retained austenite phase to be calculated.

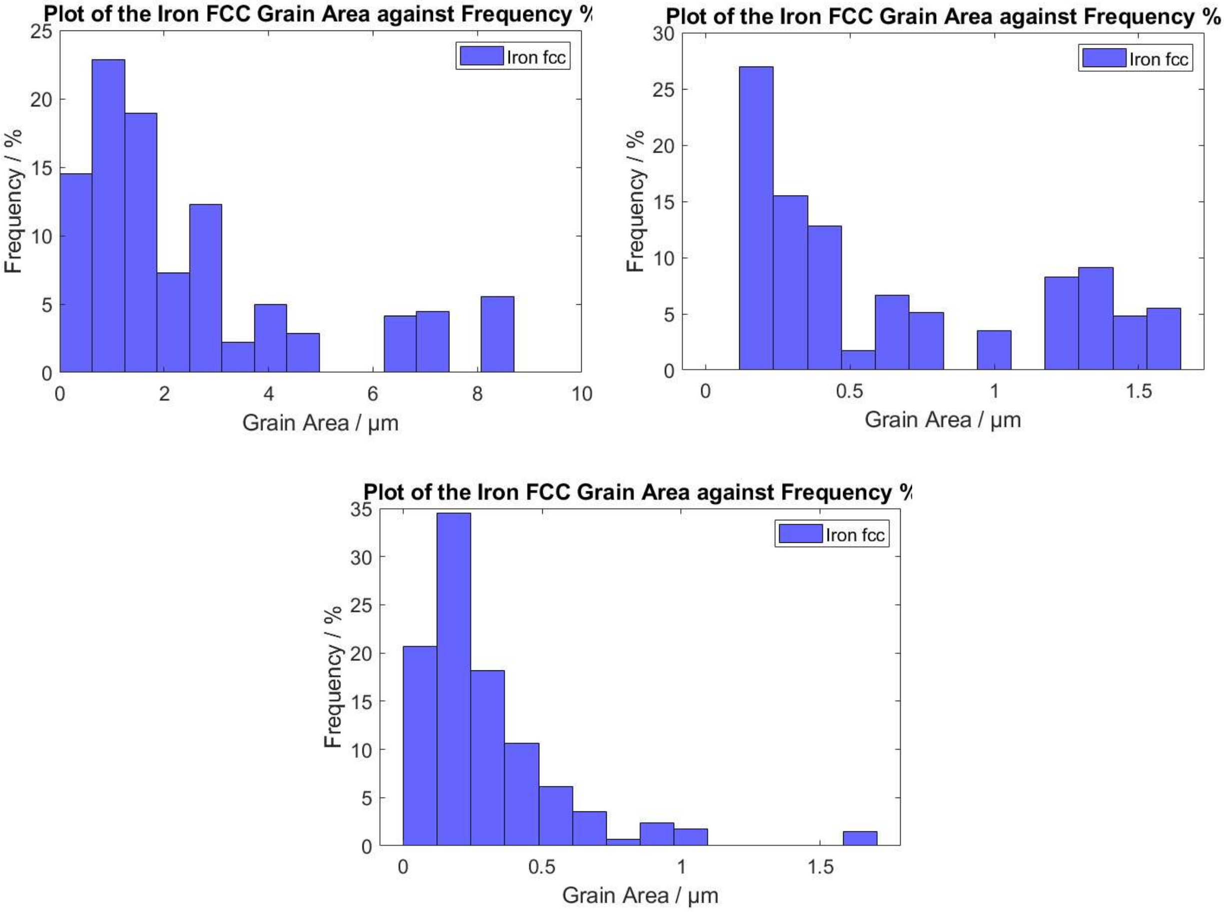

Figure 6.56: The grain area of retained austenite vs frequency plots of BAIN 1 tempered (Top left), BAIN 2 tempered (Top right) and BAIN 3 tempered (Bottom).

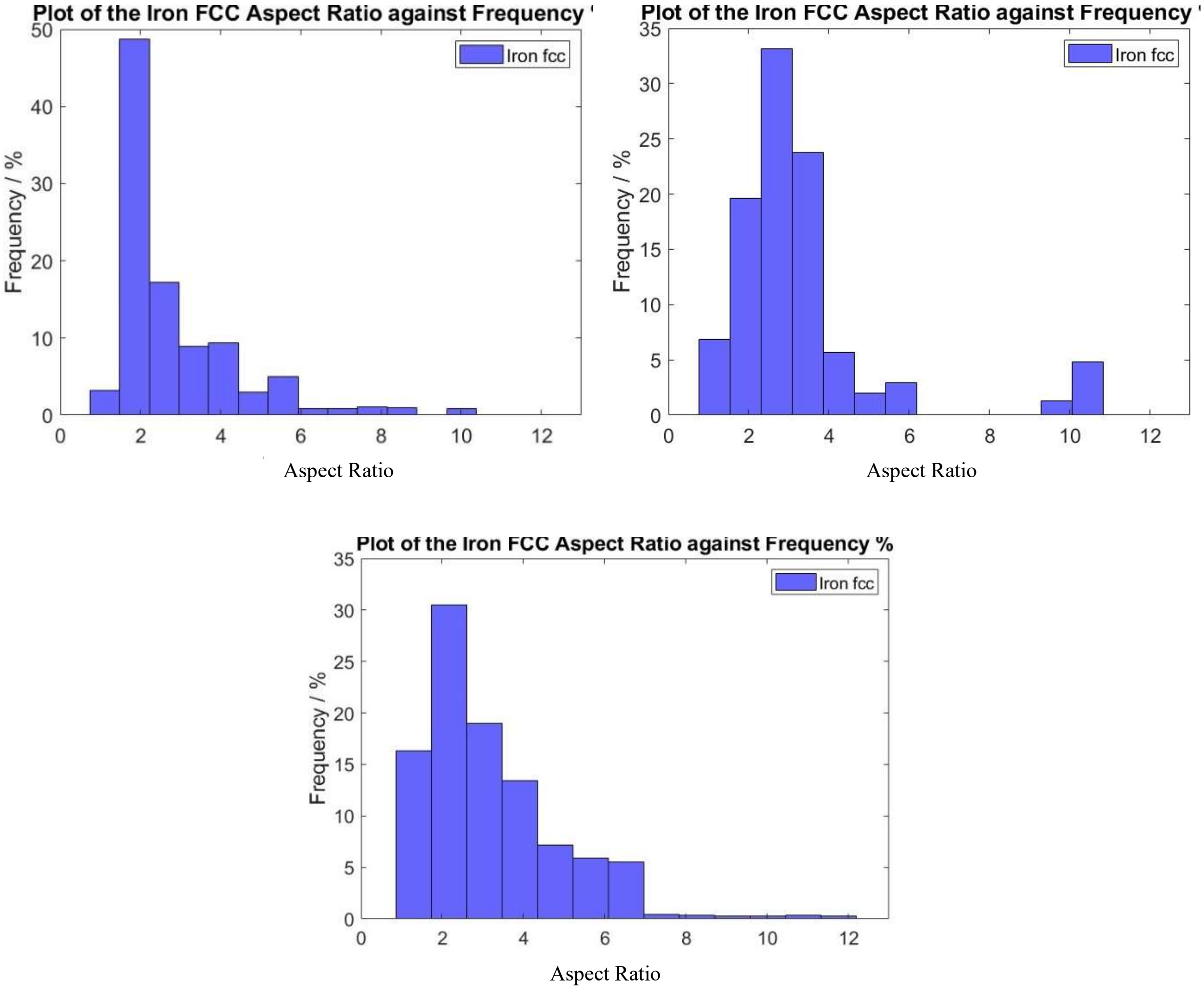

Figure 6.57: The aspect ratio of the retained austenite vs frequency plots of BAIN 1 tempered (Top left), BAIN 2 tempered (Top right) and BAIN 3 tempered (Bottom).

It can be observed in Figure 6.56 that the overall grain size of the retained austenite is much higher in BAIN 1 than in BAIN 2 and 3. Due to the larger grain size, there is a larger variation in the grain sizes present in the BAIN 2 microstructure. This supports the earlier statements that the higher M_s and transformation temperature is the probable explanation of the larger variation and mean grain area of retained austenite in BAIN 2. In contrast, BAIN 2 and BAIN 3 are much more similar in terms of the scale of the area of the retained austenite present in the 2 microstructures. One key difference between the two compositions is that there is a larger frequency of larger austenite grains (areas between 1 and 1.5 µm) in BAIN 2 than 3, shown in Figure 6.56. This could suggest that more of the larger areas retained austenite could be transformed in the BAIN 3, as the lower Mn and Cr content do increase the kinetics of the reaction.

As shown in Table 19, the XRD results show that the volume fraction of retained austenite is decreasing after the tempering step, although only marginally. The volume fraction of retained austenite for each sample and condition, was calculated using the reference intensity ratio method (RIR method), as described in Section 3.5.4.

6.3.4 Mechanical Properties

The compression data for the BAIN samples in both the salt bath and tempered conditions are displayed in Figure 6.58 below. Each of the plots are averages of three samples of the same alloy tested under that condition. As mentioned previously in the methods section, the samples were tested to an engineering strain of 0.5 (true strain of -0.7 due to compression). However, some samples failed before that level of deformation was achieved.

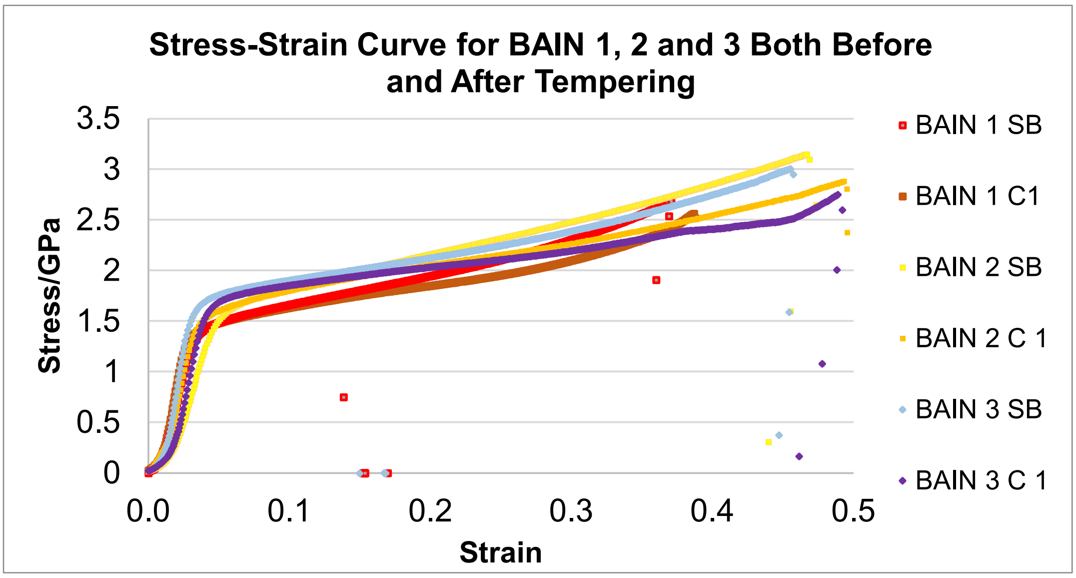

Figure 6.58: Stress-strain curve for BAIN 1, 2 and 3 both before and after tempering.

In both the salt bath and tempered condition, BAIN 1 typically failed at a strain around 0.37. The samples failed in a shear, brittle failure, suggesting that the retained austenite present had transformed into fresh untampered martensite during deformation. This supports the XRD and EBSD results, demonstrating the large amount of retained austenite present in the BAIN 1 samples. Furthermore, the phase was in polygonal and blocky morphology. As previously mentioned, blocky retained austenite is less stable than thin film retained austenite. This leads to blocky retained austenite readily transforming into martensite during deformation, forming the hard and brittle phases that worsens the toughness of the steel [48], [77]. The abundance of retained austenite and the blocky morphology is due to the high M_s and transformation temperature for the BAIN 1 composition. This causes larger phases of retained austenite, which are difficult to stabilise because of the larger diffusion distances.

Once again, BAIN 2 and BAIN 3 have results that deviate much less. The work hardening rate appears to be slightly higher in BAIN 2 than BAIN 3, leading to a higher final tensile strength reached in both the tempered and non-tempered state for BAIN 2 samples. The work hardening rate of BAIN 3 is additionally lower than BAIN 1. This could be explained by the lower amount of retained austenite present in BAIN 3 as the work hardening rate has decreased compared to that the other compositions. In comparison, BAIN 2 has a slightly higher austenite content but the phase is similarly stabilised and in the thin film morphology. This results in a good combination of both strength and ductility. Furthermore, both BAIN 1 and 3 show signs of a second higher work hardening rate after tempering. This is likely the point at which the retained austenite begins to transform into martensite under the deformation, leading to early failure in the case of BAIN 1. In comparison, BAIN 2 has a more linear gradient and the point at which the TRIP reactions would occur has not been observed when deforming up to 0.5 strain.

The tempered samples all have lower strength as expected, due to the reduction in retained austenite for work hardening. The tempering had the largest effect on BAIN 2 and 3, with BAIN 1 only showing a minimal difference in tensile strength and strain to failure. This may be due to the retained austenite present in the BAIN 1 composition containing mostly blocky morphology retained austenite, as shown in the EBSD results. The higher amount of stabilised blocky retained austenite would mean that the tempering had a minimal effect on transforming these regions to bainite. Alternatively, this could be caused by the starting fraction of this type of morphology being too high initially. The difference in the tempered condition is less evident in the hardness results, which is likely because the tempering did not have a noticeable effect on the yield strength of the alloys. However, the hardness does show the dramatic increase in hardness after deformation. This is as expected due to the high work hardening rates of the bainites. The Vickers hardness also supports BAIN 1 having lower strengths, whereby the composition also produced the lowest hardness in each of the conditions.

6.4 Conclusions

To compare the microstructural differences between BAIN 1, 2 and 3 in the salt bath treated, tempered and post-deformation condition, SEM, TEM, STEM, EDS and EBSD were used. XRD was utilised to quantify the amount of retained austenite present in the different alloys, while EBSD was used to supplement this and to provide morphology data on the area size and aspect ratio of the γ phase in the microstructures. Additionally, the mechanical properties of each of the different alloy compositions were tested using cold compression and Vickers hardness testing. Compression tests were performed on both the tempered and non-tempered samples, whilst Vickers hardness testing was performed on all sample conditions including post-deformation.

As demonstrated through both the XRD and EBSD results, the additional second isothermal holding step does appear to reduce the fraction of retained austenite present in the samples. Whilst the reduction in the volume fraction of retained austenite post the tempering step is marginal, the EBSD and SE-SEM results suggest that the step is beneficial in transforming a large amount of the austenite that is the blockier morphology. As this phase is more unstable during deformation than thin film retained austenite, decreasing the fraction of this morphology would lead to an overall increase in the ductility of the bainite. This limits the formation of untempered hard martensite during deformation through the TRIP effect.

All three alloy compositions were able to produce nanostructured carbide free bainite, similar to other studies [27], [37], [43], [46]. TEM and STEM images seem to show no evidence for the precipitation of carbides present in the microstructures. This demonstrates that the selected processing route of multiple temperature salt baths can be utilised for further study of carbide free bainite.

As expected, the alloy composition for BAIN 1 resulted in a larger amount of retained austenite present in the sample at each of the processing stages, when compared to BAIN 2 and 3. This is due the alloy composition having a higher M_s temperature and transformation temperature. The EBSD results and MTEX retained austenite grain size vs frequency plots show that the phase was much larger by area. This resulted in the early shear failure during compression testing due the formation of martensite.

BAIN 2 and BAIN 3 were both able to be deformed up to an engineering strain of 0.5 without failure. The two alloys have much more similar properties because of the marginal difference in M_s temperature and the same transformation temperature utilised for both. BAIN

2 appears to have a higher work hardening rate than BAIN 3, however, the MTEX data suggests that the retained austenite has a slightly lower overall grain size than in BAIN 3 than BAIN 2.

7.0 Conclusions

The quench and partitioned and carbide-free steel alloys were developed to investigate alternative microstructures for high carbon pearlitic steel wire. The microstructures were characterised and tested at different processing stages, utilising SEM, TEM, STEM, EBSD, EDS, Vickers hardness and compression testing. By analysing the results from both the microstructural techniques and mechanical testing, the thesis has come to the following conclusions.

The Q&P heat treatments, which used molten salt baths, were successful in creating a microstructure consisting of martensite and retained austenite. Transformation temperatures and times had a large effect on the final mechanical properties of the heat treated alloys, as shown from the mean Vickers hardness values taken from each of the samples. Transforming at lower temperatures, just above the M_s temperature of the steel composition, resulted in a finer microstructure, which increased the hardness of the samples and can be linked to an increase in the tensile strength. This shows that holding the samples for longer time periods resulted in a decrease in the hardness. This is likely due to a larger fraction of the austenite transforming into martensite.

The alloy composition chosen to investigate carbide free bainite was able to produce steel microstructures containing nanostructured bainite and retained austenite. Initially the isothermal heat treatment was performed successfully using the FTTU of the TMC machine at the university, the microstructure was also successfully replicated using salt baths and this method proved to be more efficient at processing multiple samples.

The initial investigation on carbide free bainite found that to produce the finest microstructure, a transformation temperature slightly above the M_s temperature must be utilised. This had an added benefit of producing thin film retained austenite, which is the most stable morphology for the phase and inhibits the austenite transforming into fresh untempered martensite upon deformation. However, the microstructures of BAIN 0 still contained a large fraction of blocky polygonal retained austenite. Therefore, BAIN 1 - 3 received a second tempering heat treatment to attempt to transform the larger regions of retained austenite into bainite.

The alloy compositions of BAIN 1 - 4 were designed to have varying carbon, manganese and chromium to investigate the effects of varying the M_s temperature and whether decreasing the Mn and Cr additions increased the volume fraction of bainite produced during the isothermal transformation step. It was shown through EBSD and XRD that BAIN 1 had the highest amount of retained austenite present and this negatively impacted the mechanical properties of the steel. The high amount of retained austenite was due to the high M_s and therefore transformation temperature which was used during heat treatment. This resulted in a low volume fraction of bainite and unstable block retained austenite. In comparison, BAIN 2 - 3 had more similar mechanical properties, likely due to being transformed at the same temperature. However, BAIN 2 showed a higher work hardening rate than BAIN 3 during compression testing. The graphs produced using AZTecCrystal which display the grain area and aspect ratio of the retained austenite in BAIN 2 and 3, after the second isothermal holding step, suggest that a larger proportion of the retained austenite present in BAIN 3 was in the thin film morphology. This builds on existing evidence [46] that reducing the Mn and Cr additions, decreases the transformation times for the carbide-free bainite. This finding could positively impact future research by enabling the reduction of transformation times for producing nanostructured bainite. TEM and STEM showed that the microstructures were carbide free and that there was martensite in some regions of the samples, prior to deformation. Additionally, EDS of the STEM images show that the carbon is partitioning the retained austenite to stabilise the phase. The retained austenite present is very fine in scale, ranging from around 50 to 100 nm in width.

This work found that the second isothermal holding step, also referred to as tempering, does decrease the volume fraction of austenite present in all the BAIN samples. This is clearly demonstrated by the results from XRD and the EBSD maps. The lower volume fraction retained austenite decreases the work hardening rate of the alloys but increases the elongation of the samples. This supports the work done by Avishan et al. [49] and Wang et al. [48], who found that multi-step isothermal bainitic transformation was beneficial in reducing the amount of blocky retained austenite present in nanostructured bainites. Since this morphology of retained austenite is much less stable than the thin film morphology, it is much more likely to undergo the TRIP effect and form untempered martensite during wire drawing/deformation. This demonstrates that utilising multi-step isothermal bainitic transformation could be highly beneficial to future work on carbide-free bainitic microstructures for the steel wire/rod industry.

8.0 Future Work

This chapter highlights points of interest for future work and discuss matters that could be beneficial for further studies in this field.

The M_s values for the steel compositions produced for this project were estimated using empirical formulas and programs such as those available on the Materials Algorithms Project Program Library [74]. Whilst these estimations are useful in the absence of accurate dilatometry, having a more accurate value of the M_s temperature would be highly beneficial. This would allow for potentially lower transformation temperatures to be utilised, producing finer bainitic microstructures with a larger proportion of thin film retained austenite. This would result in more stable retained austenite which would delay the transformation to martensite during deformation. Furthermore, the M_s temperature of the alloys investigated could be more accurately compared to other research in the field that utilise dilatometry.

Stress-strain data for each of the samples was studied using cold compression testing, performed by the TMC machine in the University of Sheffield. This was originally chosen due to the limitation of facilities through the COVID-19 pandemic and the high thermal control the machine fast thermal treatment unit (FTTU) provides. However, almost all research utilises tensile testing. This more accurately represents wire and rod in use, as the steel is usually under a tensile force. Obtaining tensile stress-strain data curves would allow for comparison between mechanical in other studies and be a more suitable way to compare mechanical properties to other wire and rod work.

More work is needed to assess the cold wire drawing capabilities of the carbide free bainitic microstructures. British Steel had many issues drawing bainite due to the formation of martensite through the TRIP effect limiting the drawability. Research in this area would provide more data to assess the viability of the microstructure as an alternative for the steel rod and wire industry, to the widely used high carbon pearlite. Torsion testing would also be required to assess the samples behaviour during twisting.

The alloy compositions chosen for this work were relatively simple, containing only carbon, silicon, manganese and chromium. However, cobalt and aluminium both increase the free energy change for the bainitic transformation. Garcia-Mateo et al. [46] found that small additions of these elements increased the volume fraction of bainitic ferrite, V_b, and can reduce the transformation times. Future work could investigate alloys containing one or more of additions, however, the added cost to the alloy production must be considered.

Atom probe tomography (APT) would be a useful technique for future studies, allowing for estimations of the carbon concentration in both the retained austenite and bainitic ferrite. In combination with XRD, this can provide more data on how the carbon concentration changes throughout the isothermal holding heat treatment.

Finally, longer isothermal holding times could be utilised to try to obtain as much bainitic ferrite as possible. In this study, transformation times were limited to three hours or less due to time constraints of the project. However, isothermal holding times of three days and longer have been used in previous research [17], [21], [27], [35], [46]. It is important to find a suitable facility for the long isothermal heat treatments and could prove challenging logistically.

9.0 Appendix

9.1 XRD Data

Figures 9.1 to Figure 9.6 show the XRD plot for each the three BAIN alloys in both the salt bath and tempered conditions.

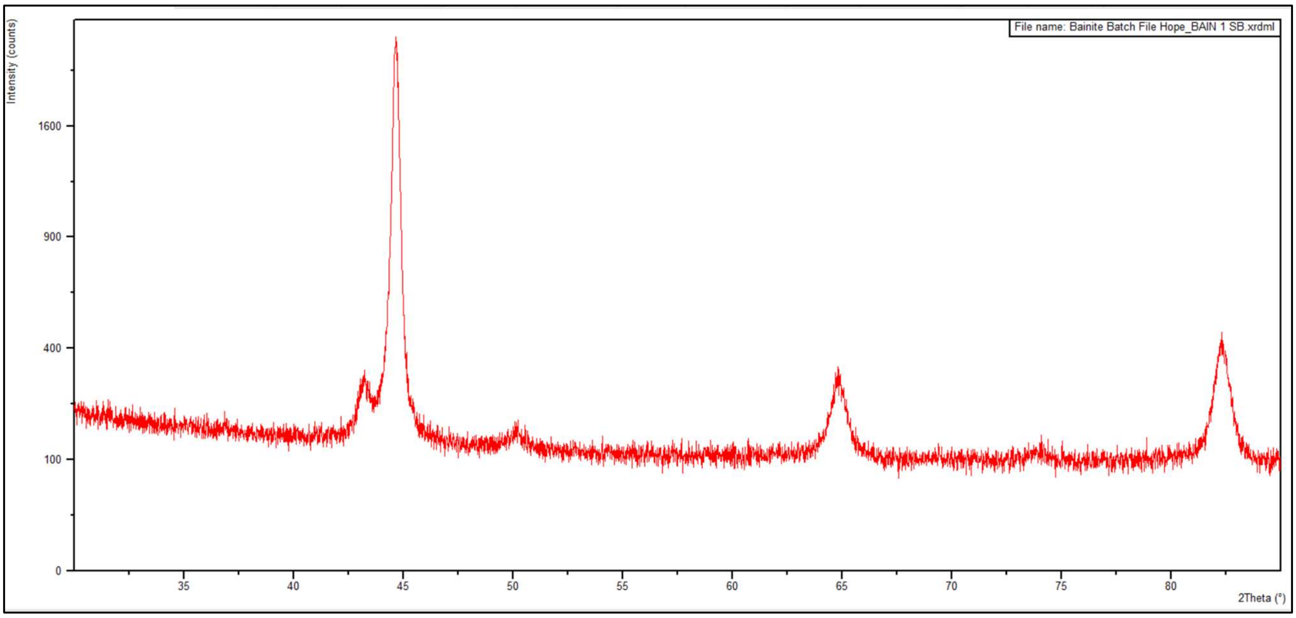

Figure 9.1: Cu K-a XRD plot for BAIN 1 in the salt bath condition.

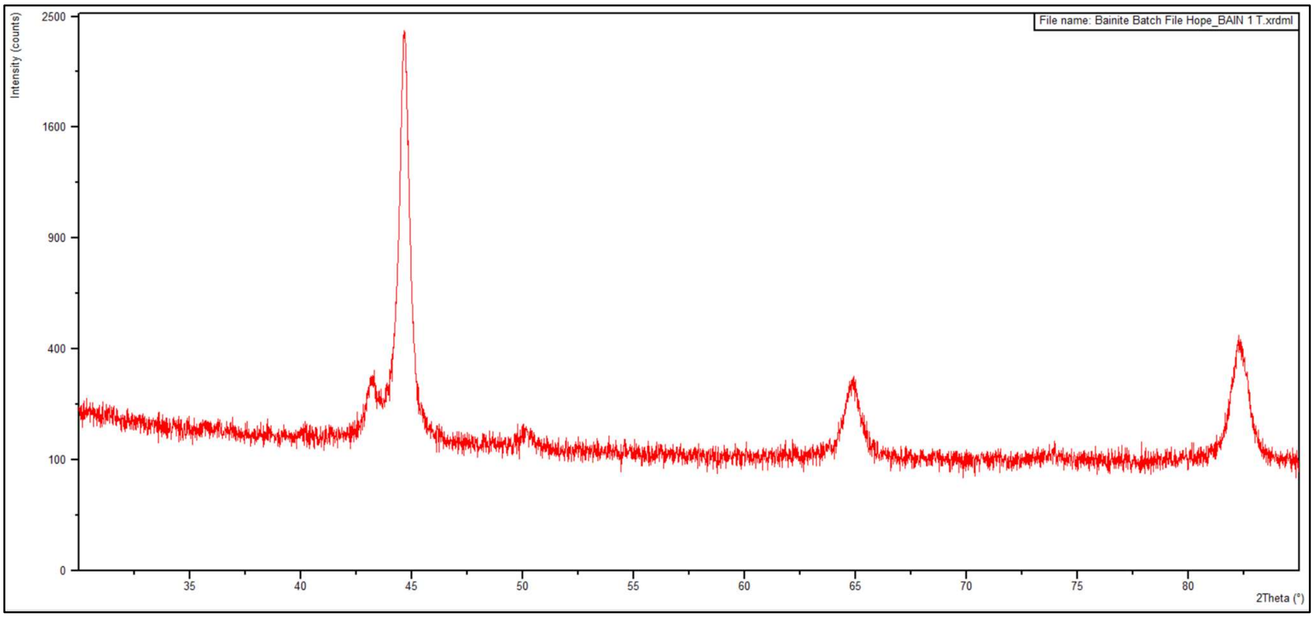

Figure 9.2: Cu K-a XRD plot for BAIN 1 in the tempered condition.

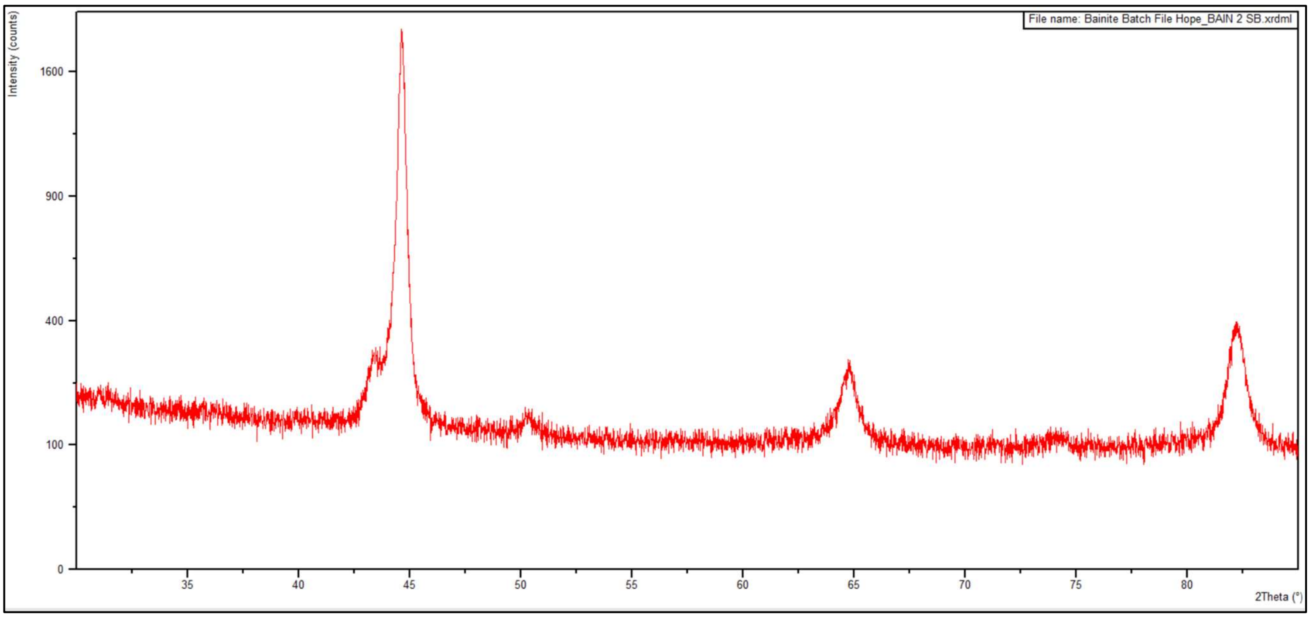

Figure 9.3: Cu K-a XRD plot for BAIN 2 in the salt bath condition.

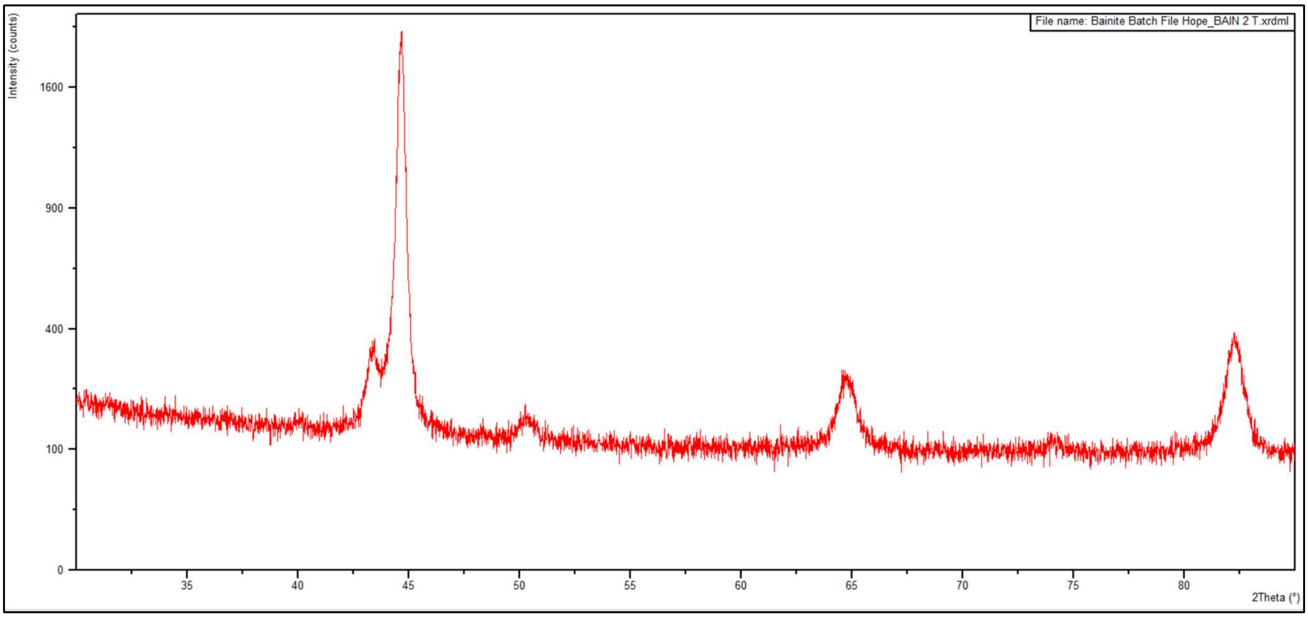

Figure 9.4: Cu K-a XRD plot for BAIN 2 in the tempered condition.

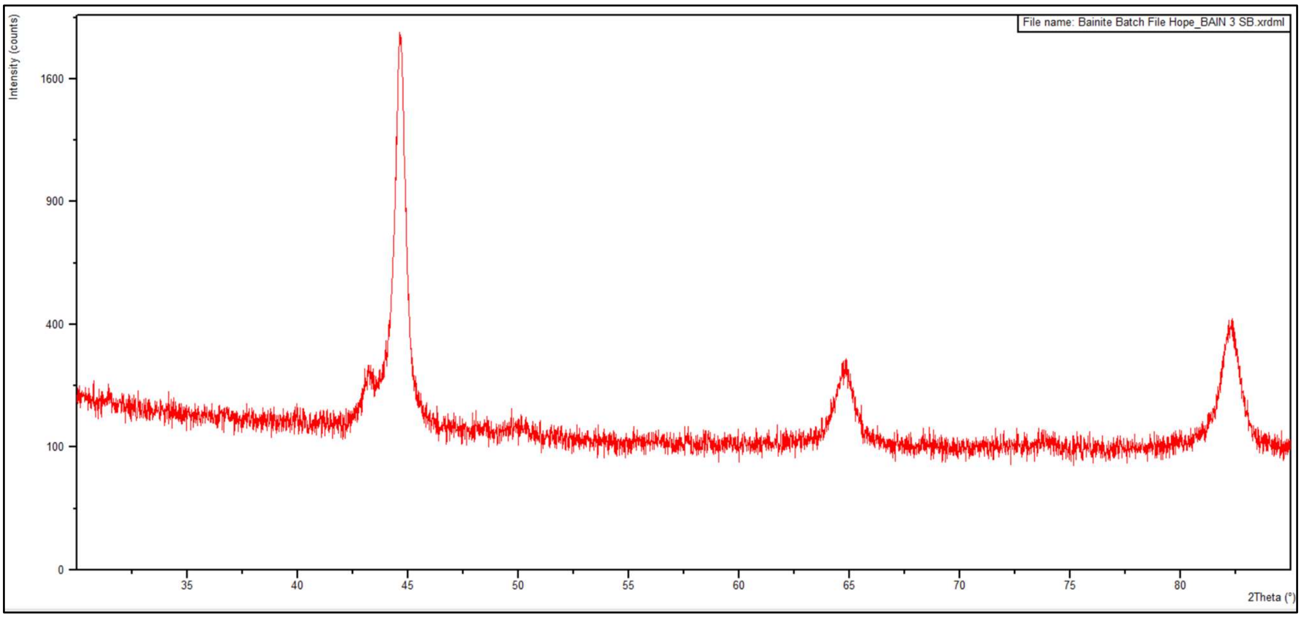

Figure 9.5: Cu K-a XRD plot for BAIN 3 in the salt bath condition.

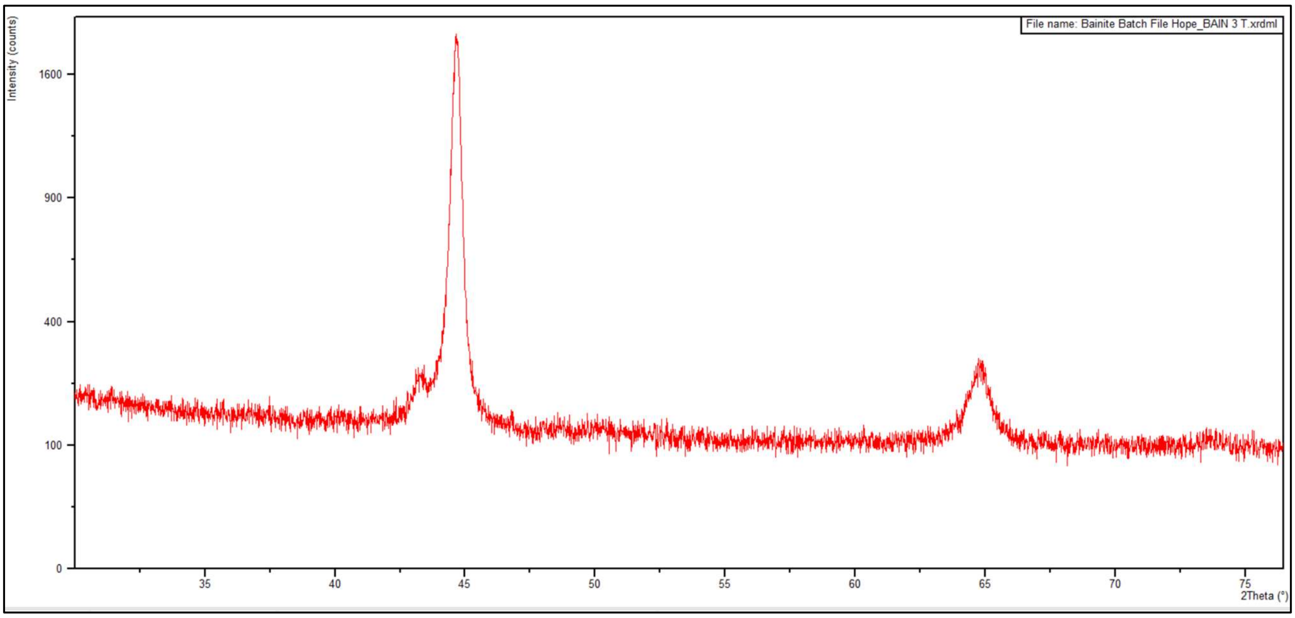

Figure 9.6: Cu K-a XRD plot for BAIN 3 in the tempered condition.

9.2 Vickers Hardness Values

Table 9.1 on the following page, shows the Vickers hardness readings that were used to calculate the mean hardness values for BAIN 1, 2 and 3 in both the salt bath and tempered conditions.

Table 9.1: Vickers hardness values used to calculate the mean Vickers hardness for BAIN 1, 2 and 3 in the salt bath (SB) and tempered (T) condition.

		length(H)	Vh	Length(V)	Vv		V average
BAIN 1 SB	1	333.0	418.1	332.5	419.4		418.7
	2	325.5	437.6	334.0	415.6		426.6
	3	326.0	436.2	333.0	418.1		427.2
	4	326.0	436.2	327.5	432.3		434.3
	5	329.0	428.3	329.5	427.0		427.7
BAIN 1 T	1	307.0	491.9	311.5	477.8		484.9
	2	324.0	441.6	326.0	436.2		438.9
	3	326.0	436.2	332.5	419.4		427.8
	4	340.0	401.1	333.5	416.8		409.0
	5	335.5	411.9	343.0	394.1		403.0
BAIN 2 SB	1	317.0	461.4	310.0	482.4		471.9
	2	310.5	480.9	310.5	480.9		480.9
	3	317.0	461.4	311.5	477.8		469.6
	4	310.0	482.4	312.5	474.8		478.6
	5	310.0	482.4	309.0	485.6		484.0
BAIN 2 T	1	307.0	491.9	313.0	473.2		482.6
	2	318.0	458.5	314.0	470.2		464.4
	3	312.0	476.3	310.0	482.4		479.4
	4	316.0	464.3	310.5	480.9		472.6
	5	313.0	473.2	316.0	464.3		468.8
BAIN 3 SB	1	304.5	500.0	306.5	493.5		496.8
	2	304.5	500.0	306.5	493.5		496.8
	3	306.5	493.5	307.0	491.9		492.7
	4	301.0	511.7	303.5	503.3		507.5
	5	300.5	513.4	301.0	511.7		512.6
BAIN 3 T	1	290	551.3	294	536.4		543.8
	2	300	515.1	298.5	520.3		517.7
	3	299.5	516.9	303.5	503.3		510.1
	4	300.5	513.4	295.5	530.9		522.2

	5	300	515.1	299	518.6		516.9

10.0 References

[1] X. Zhang, A. Godfrey, X. Huang, N. Hansen, and Q. Liu, “Microstructure and strengthening mechanisms in cold-drawn pearlitic steel wire,” *Acta Mater.*, vol. 59, no. 9, pp. 3422–3430, 2011, doi: 10.1016/j.actamat.2011.02.017.

[2] S. Semiatin, “ASM Handbook, Vol. 14: Forming and Forging,” *ASM Int. Ohio, USA*, 1993.

[3] J. . Embury and R. . Fisher, “The Structure and Properties of Drawn Pearlite,” *Acta Metall.*, vol. 14, pp. 147–159, 1966.

[4] G. Langford, “Deformation of pearlite,” *Metall. Trans. A*, vol. 8, no. 6, pp. 861–875, Jun. 1977, doi: 10.1007/BF02661567.

[5] C. Borchers and R. Kirchheim, “Cold-drawn pearlitic steel wires,” *Prog. Mater. Sci.*, vol. 82, pp. 405–444, 2016, doi: 10.1016/j.pmatsci.2016.06.001.

[6] A. Lamontagne, X. Kleber, V. Massardier-Jourdan, and D. Mari, “Identification of the mechanisms responsible for static strain ageing in heavily drawn pearlitic steel wires,” *Philos. Mag. Lett.*, vol. 94, no. 8, pp. 495–502, 2014, doi: 10.1080/09500839.2014.938137.

[7] J. Takahashi, M. Kosaka, K. Kawakami, and T. Tarui, “Change in carbon state by low-temperature aging in heavily drawn pearlitic steel wires,” *Acta Mater.*, vol. 60, no. 1, pp. 387–395, 2012, doi: 10.1016/j.actamat.2011.09.014.

[8] K. K. Ray and D. Mondal, “The effect of interlamellar spacing on strength of pearlite in annealed eutectoid and hypoeutectoid plain carbon steels,” *Acta Metall. Mater.*, vol. 39, no. 10, pp. 2201–2208, 1991, doi: 10.1016/0956-7151(91)90002-I.

[9] W. J. Nam, C. M. Bae, and C. S. Lee, “Effect of carbon content on the Hall-Petch parameter in cold drawn pearlitic steel wires,” *J. Mater. Sci.*, vol. 37, no. 11, pp. 2243–

2249, 2002, doi: 10.1023/A:1015361031384.

[10] M. Gensamer, E. B. Pearsall, W. S. Pellini, and J. R. Low, “The Tensile Properties of Pearlite, Bainite, and Spheroidite,” *Metallogr. Microstruct. Anal.*, vol. 1, no. 3–4, pp. 171–189, 2012, doi: 10.1007/s13632-012-0027-7.

[11] F. Fang *et al.*, “Deformation of cementite in cold drawn pearlitic steel wire,” *Mater. Sci. Eng. A*, vol. 608, pp. 11–15, 2014, doi: 10.1016/j.msea.2014.04.050.

[12] L. Zhou, F. Fang, X. Zhou, Y. Tu, Z. Xie, and J. Jiang, “Cementite nano-crystallization in cold drawn pearlitic wires instigated by low temperature annealing,” *Scr. Mater.*, vol. 120, pp. 5–8, 2016, doi: 10.1016/j.scriptamat.2016.04.002.

[13] A. Lamontagne, V. Massardier, X. Kléber, X. Sauvage, and D. Mari, “Comparative study and quantification of cementite decomposition in heavily drawn pearlitic steel wires,” *Mater. Sci. Eng. A*, vol. 644, pp. 105–113, 2015, doi: 10.1016/j.msea.2015.07.048.

[14] V. N. Gridnev, V. G. Gavrilyuk, I. Y. Dekhtyar, Y. Y. Meshkov, P. S. Nizin, and V. G. Prokopenko, “Investigation of carbide phase in strained steel by the method of nuclear gamma resonance,” *Phys. Status Solidi*, vol. 14, no. 2, pp. 689–694, 1972, doi: 10.1002/pssa.2210140238.

[15] S. Yamasaki, “The microstructure and mechanical properties of drawn and aged pearlitic steel wires,” *Mater. Sci. Technol. (United Kingdom)*, vol. 34, no. 1, pp. 1–11, 2018, doi: 10.1080/02670836.2017.1407542.

[16] E. S. Davenport and E. C. Bain, “Transformation of austenite at constant subcritical temperatures,” *Metall. Mater. Trans. B*, vol. 1, no. 12, pp. 3503–3530, Dec. 1970, doi: 10.1007/BF03037892.

[17] H. K. D. H. (Harshad K. D. H. Bhadeshia, *Bainite in steels : transformations, microstructure and properties*. London: London : Institute of Materials, 1992, 1992.

[18] M. Takahashi and H. K. D. H. Bhadeshia, “Model for transition from upper to lower bainite,” *Mater. Sci. Technol.*, vol. 6, no. 7, pp. 592–603, 1990, doi: 10.1179/mst.1990.6.7.592.

[19] C. Zener, “Equilibrium relations in medium-alloy steels,” *Trans. Am. Inst. Min. Metall. Eng.*, vol. 167, pp. 513–534, 1946.

[20] R. Le Houillier, G. Begin, and A. Dubé, “A study of the peculiarities of austenite during the formation of bainite,” *Metall. Trans.*, vol. 2, pp. 2645–2653, 1971.

[21] F. G. Caballero and H. K. D. H. Bhadeshia, “Development of Hard Bainite,” vol. 43, no. 8, pp. 1238–1243, 2003.

[22] L. C. D. Fielding, “The Bainite Controversy,” *Mater. Sci. Technol. (United Kingdom)*, vol. 29, no. 4, pp. 383–399, 2013, doi: 10.1179/1743284712Y.0000000157.

[23] H. J. Stone, M. J. Peet, H. K. D. . Bhadeshia, P. J. Withers, S. S. Babu, and E. D. Specht, “Synchrotron X-ray studies of austenite and bainitic ferrite,” *Proc. R. Soc. A, Math. Phys. Eng. Sci.*, vol. 464, no. 2092, pp. 1009–1027, 2008, doi: 10.1098/rspa.2007.0201.

[24] E. Swallow, H. K. D. H. Bhadeshia, E. Swallow, and H. K. D. H. Bhadeshia, “High resolution observations of displacements caused by bainitic transformation High resolution observations of displacements caused by bainitic transformation,” vol. 0836, 2013, doi: 10.1179/mst.1996.12.2.121.

[25] F. G. Caballero, M. K. Miller, C. Garcia-mateo, and J. Cornide, “New experimental evidence of the diffusionless transformation nature of bainite,” *J. Alloys Compd.*, vol. 577, pp. S626–S630, 2013, doi: 10.1016/j.jallcom.2012.02.130.

[26] F. G. Caballero, M. K. Miller, and C. Garcia-mateo, “Carbon supersaturation of ferrite in a nanocrystalline bainitic steel,” *Acta Mater.*, vol. 58, no. 7, pp. 2338–2343, 2010, doi: 10.1016/j.actamat.2009.12.020.

[27] F. G. Caballero, H. K. D. H. Bhadeshia, K. J. A. Mawella, D. G. Jones, and P. Brown, “Design of novel high strength bainitic steels: Part 1,” *Mater. Sci. Technol.*, vol. 17, no. 5, pp. 512–516, 2001, doi: 10.1179/026708301101510348.

[28] F. G. Caballero, H. K. D. H. Bhadeshia, K. J. A. Mawella, D. G. Jones, and P. Brown, “Design of novel high strength bainitic steels: Part 2,” *Mater. Sci. Technol.*, vol. 17, no. 5, pp. 517–522, 2001, doi: 10.1179/026708301101510357.

[29] G. Gomez, T. Pérez, and H. K. D. H. Bhadeshia, “Air cooled bainitic steels for strong, seamless pipes Part 1 - alloy design, kinetics and microstructure,” *Mater. Sci. Technol.*, vol. 25, no. 12, pp. 1501–1507, 2009, doi: 10.1179/174328408X388130.

[30] G. Gomez, T. Pérez, and H. K. D. H. Bhadeshia, “Air cooled bainitic steels for strong, seamless pipes Part 2 - properties and microstructure of rolled material,” *Mater. Sci. Technol.*, vol. 25, no. 12, pp. 1508–1512, 2009, doi: 10.1179/174328408X388149.

[31] A. Borgenstam, M. Hillert, and A. John, “Metallographic evidence of carbon diffusion in the growth of bainite,” vol. 57, pp. 3242–3252, 2009, doi: 10.1016/j.actamat.2009.03.026.

[32] R. F. Hehemann, K. R. Kinsman, and H. I. Aaronson, “A debate on the bainite reaction,” *Metall. Trans.*, vol. 3, pp. 1077–1094, 1972.

[33] H. K. D. H. Bhadeshia and D. V. Edmonds, “Bainite in silicon steels: New composition-property approach, Part 1,” *Met. Sci.*, vol. 17, no. 9, pp. 411–419, 1983, doi: 10.1179/030634583790420600.

[34] H. K. D. H. Bhadeshia and D. V. Edmonds, “Bainite in silicon steels: New composition-property approach, Part 2,” *Met. Sci.*, vol. 17, no. 9, pp. 420–425, 1983, doi: 10.1179/030634583790420646.

[35] F. G. Caballero, H. K. D. H. Bhadeshia, K. J. A. Mawella, D. G. Jones, and P. Brown, “Very strong low temperature bainite,” *Mater. Sci. Technol.*, vol. 18, no. 3, pp. 279–

284, 2002, doi: 10.1179/026708301225000725.

[36] F. G. Caballero, C. Garcia-Mateo, and M. K. Miller, “Design of novel bainitic steels: Moving from ultrafine to nanoscale structures,” *Jom*, vol. 66, no. 5, pp. 747–755, 2014, doi: 10.1007/s11837-014-0908-0.

[37] L. Morales-Rivas, C. Garcia-Mateo, T. Sourmail, M. Kuntz, R. Rementeria, and F. G. Caballero, “Ductility of nanostructured bainite,” *Metals (Basel).*, vol. 6, no. 12, 2016, doi: 10.3390/met6120302.

[38] P. J. Jacques, “Transformation-induced plasticity for high strength formable steels,” *Curr. Opin. Solid State Mater. Sci.*, vol. 8, no. 3–4, pp. 259–265, 2004, doi: 10.1016/j.cossms.2004.09.006.

[39] T. Sourmail *et al.*, “Understanding the basic mechnaism to optimize and predict in service properties of nanobanitic steels,” *Res. Fund Coal Steel*, 2016.

[40] B. P. J. Sandvik and H. P. Nevalainen, “Structure–property relationships in commercial low-alloy bainitic–austenitic steel with high strength, ductility, and toughness,” *Met. Technol.*, vol. 8, no. 1, pp. 213–220, 1981, doi: 10.1179/030716981803275992.

[41] F. G. Caballero and C. Garcia-Mateo, “The role of retained austenite on tensile properties of steels with bainitic microstructures,” *Mater. Trans.*, vol. 46, no. 8, pp. 1839–1846, 2005.

[42] H. K. D. H. Bhadeshia, “Bessemer memorial lecture: The dimensions of steel,” *Ironmak. Steelmak.*, vol. 34, no. 3, pp. 194–199, 2007, doi: 10.1179/174328107X174753.

[43] C. Garcia-Mateo *et al.*, “Nanostructured steel industrialisation: Plausible reality,” *Mater. Sci. Technol. (United Kingdom)*, vol. 30, no. 9, pp. 1071–1078, 2014, doi: 10.1179/1743284713Y.0000000428.

[44] I. Y. Pyshmintsev, M. De Meyer, B. C. De Cooman, R. A. Savray, V. P. Shveykin, and M. Vermeulen, “The influence of the stress state on the plasticity of transformation induced plasticity-aided steel,” *Metall. Mater. Trans. A Phys. Metall. Mater. Sci.*, vol. 33, no. 6, pp. 1659–1667, 2002, doi: 10.1007/s11661-002-0175-5.

[45] T. Sourmail, C. Garcia-Mateo, F. G. Caballero, L. Morales-Rivas, R. Rementeria, and M. Kuntz, “Tensile ductility of nanostructured bainitic steels: Influence of retained austenite stability,” *Metals (Basel).*, vol. 7, no. 1, pp. 1–7, 2017, doi: 10.3390/met7010031.

[46] F. G. Garcia-Mateo, C, Caballero and H. K. D. H. Bhadeshia, “Acceleration of Low-temperature Bainite,” *ISIJ Int.*, vol. 43, no. 11, pp. 1821–1825, 2003.

[47] M. Soliman, H. Mostafa, A. S. El-Sabbagh, and H. Palkowski, “Low temperature bainite in steel with 0.26wt% C,” *Mater. Sci. Eng. A*, vol. 527, no. 29–30, pp. 7706–7713, 2010, doi: 10.1016/j.msea.2010.08.037.

[48] X. L. Wang, K. M. Wu, F. Hu, L. Yu, and X. L. Wan, “Multi-step isothermal bainitic transformation in medium-carbon steel,” *Scr. Mater.*, vol. 74, pp. 56–59, 2014, doi: 10.1016/j.scriptamat.2013.10.019.

[49] B. Avishan, M. Tavakolian, and S. Yazdani, “Two-step austempering of high performance steel with nanoscale microstructure,” *Mater. Sci. Eng. A*, vol. 693, no. January, pp. 178–185, 2017, doi: 10.1016/j.msea.2017.03.104.

[50] S. Wiewiórowska and Z. Muskalski, “The Application of Low and Medium Carbon Steel with Multiphase TRIP Structure in Drawing Industry,” *Procedia Manuf.*, vol. 2, no. February, pp. 181–185, 2015, doi: 10.1016/j.promfg.2015.07.031.

[51] Z. Yu, Z. Mi, J. Guo, and N. Gong, “Studying inhomogeneous deformation of bainite-retained austenite steel during cold drawing,” *Mater. Res. Express*, vol. 5, no. 9, 2018, doi: 10.1088/2053-1591/aad850.

[52] H. IzumIda, K. Shimizu, S. Takamura, Y. Shimoda, O. Momozawa, and T. Murai, “Development of high-strength steel wire with superior weldability,” *SEI Tech. Rev.*, no. 75, pp. 141–145, 2012.

[53] S. Hobson, “Superbainitic Rod Project,” *TATA STEEL*, no. Reference Source No: 151758, pp. 1–6, 2010.

[54] S. C. Hobson, “Bainitic Rod Project – Examination of 0.90C-Si-Cr Steel,” *TATA STEEL*, no. Reference Source No: 153123, pp. 1–11, 2011.

[55] S. Hobson, “Bainitic Rod Project - Assessment of 0.40C-Si-Mn-Cr Steel,” *TATA STEEL*, no. Reference Source No: 157046, pp. 1–19, 2013.

[56] S. Matas and R. F. Hehemann, “Retained Austenite and the Tempering of Martensite,” *Nature*, vol. 187, no. 4738, pp. 685–686, Aug. 1960, doi: 10.1038/187685a0.

[57] J. Speer, D. K. Matlock, B. C. De Cooman, and J. G. Schroth, “Carbon partitioning into austenite after martensite transformation,” *Acta Mater.*, vol. 51, no. 9, pp. 2611–2622, 2003, doi: 10.1016/S1359-6454(03)00059-4.

[58] F. Rizzo and D. Matlock, “The "Quenching and Partitioning " Process: Background and Recent Progress,” *Mater. Res.*, vol. 8, no. No. 4, pp. 417–423, 2005, doi: 10.1590/S1516-14392005000400010.

[59] J. H. Jang, I. G. Kim, and H. K. D. H. Bhadeshia, “Substitutional solution of silicon in cementite: A first-principles study,” *Comput. Mater. Sci.*, vol. 44, no. 4, pp. 1319–1326, 2009, doi: 10.1016/j.commatsci.2008.08.022.

[60] S. S. Nayak, R. Anumolu, R. D. K. Misra, K. H. Kim, and D. L. Lee, “Microstructure-hardness relationship in quenched and partitioned medium-carbon and high-carbon steels containing silicon,” *Mater. Sci. Eng. A*, vol. 498, no. 1–2, pp. 442–456, 2008, doi: 10.1016/j.msea.2008.08.028.

[61] I. de Diego-Calderón, I. Sabirov, J. M. Molina-Aldareguia, C. Föjer, R. Thiessen, and

R. H. Petrov, “Microstructural design in quenched and partitioned (Q&P) steels to improve their fracture properties,” *Mater. Sci. Eng. A*, vol. 657, pp. 136–146, 2016, doi: 10.1016/j.msea.2016.01.011.

[62] N. Maheswari, S. G. Chowdhury, K. C. Hari Kumar, and S. Sankaran, “Influence of alloying elements on the microstructure evolution and mechanical properties in quenched and partitioned steels,” *Mater. Sci. Eng. A*, vol. 600, pp. 12–20, 2014, doi: 10.1016/j.msea.2014.01.066.

[63] M. J. Santofimia, T. Nguyen-Minh, L. Zhao, R. Petrov, I. Sabirov, and J. Sietsma, “New low carbon Q&P steels containing film-like intercritical ferrite,” *Mater. Sci. Eng. A*, vol. 527, no. 23, pp. 6429–6439, 2010, doi: 10.1016/j.msea.2010.06.083.

[64] B. Kim, J. Sietsma, and M. J. Santo, “The role of silicon in carbon partitioning processes in martensite / austenite microstructures,” vol. 127, no. March, pp. 336–345, 2017, doi: 10.1016/j.matdes.2017.04.080.

[65] S. Yan, X. Liu, W. J. Liu, T. Liang, B. Zhang, and L. Liu, “A Comparative study on microstructure and mechanical properties of a C-Mn- Si steel treated by quenching and partitioning (Q & P) processes after a full and intercritical austenitization,” *Mater. Sci. Eng. A*, vol. 684, no. December 2016, pp. 261–269, 2017, doi: 10.1016/j.msea.2016.12.026.

[66] C. Y. Wang, Y. Chang, X. D. Li, K. M. Zhao, and H. Dong, “Relation of martensite-retained austenite and its effect on microstructure and mechanical properties of the quenched and partitioned steels,” *Sci. China Technol. Sci.*, vol. 59, no. 5, pp. 832–838, 2016, doi: 10.1007/s11431-016-6045-y.

[67] R. O. Ritchie, M. H. C. Cedeno, V. F. Zackay, and E. R. Parker, “Effects of silicon additions and retained austenite on stress corrosion cracking in ultrahigh strength steels,” *Metall. Trans. A*, vol. 9, no. 1, pp. 35–40, 1978, doi: 10.1007/BF02647168.

[68] M. S. Loveday *et al.*, “Measurement of flow stress in hot plane strain compression tests,” *Mater. High Temp.*, vol. 23, no. 2, pp. 85–118, Jan. 2006, doi: 10.1179/mht.2006.006.

[69] R. Wu *et al.*, “Enhancement of mechanical properties for quenched and partitioned steels via intragranular austenite,” *Ironmak. Steelmak.*, vol. 43, no. 8, pp. 616–620, 2016, doi: 10.1080/03019233.2015.1132124.

[70] L. Deng and P. F. Morris, “A review of potential ultra high strength steel wires,” vol. 44, no. 0, 2010.

[71] H. K. D. H. Bhadeshia and D. V. Edmonds, “Mechanism of Bainite Formation in Steels.,” *Acta Metall.*, vol. 28, no. 9, pp. 1265–1273, 1980, doi: 10.1016/0001-6160(80)90082-6.

[72] C. Garcia-Mateo *et al.*, “Tensile behaviour of a nanocrystalline bainitic steel containing 3wt% silicon,” *Mater. Sci. Eng. A*, vol. 549, pp. 185–192, 2012, doi: 10.1016/j.msea.2012.04.031.

[73] H. K. D. H. Bhadeshia and D. V. Edmonds, “Bainite in silicon steels: New composition-property approach,” *Met. Sci.*, vol. 17, no. 9, pp. 411–419, 1983, doi: 10.1179/030634583790420600.

[74] M. A. Project and P. Library, “Program MAP_STEEL_MUCG83.” https://www.phase-trans.msm.cam.ac.uk/map/steel/programs/mucg83.html#down (accessed Jun. 22, 2021).

[75] G. Papadirnitriou and G. Fourlaris, “A TEM Investigation of the Stepped Bainite Reaction in Silicon Steels,” vol. 7, 1997.

[76] V. E. (Vernon E. Cosslett, *Practical electron microscopy*. London: Butterworths Scientific, 1951.

[77] E. Bonnevie, G. Ferri, A. Ikhlef, D. Kaplan, and J. M. Orain, “Morphological aspects

of martensite – austenite constituents in intercritical and coarse grain heat affected zones of structural steels,” vol. 385, pp. 352–358, 2004, doi: 10.1016/j.msea.2004.06.033.